TEM study of the structural evolution of ionic solids from amorphous to polycrystalline phases in the case of alkaline earth difluoride systems

Experimental exploration of energy landscape

Vom Fachbereich Material- und Geowissenschaften
der Technischen Universität Darmstadt

zur Erlangung des akademischen Grades eines
Doktor-Naturwissenschaften

genehmigte Dissertation

vorgelegt von

M.Sc. Xiaoke Mu

aus Shandong–China

Berichterstatter:	Prof. Dr. Hans-Joachim Kleebe
Mitberichterstatter:	Prof. Dr. Peter A van Aken
Tag der Einreichung:	17.06.2013
Tag der mündlichen Prüfung:	20.08.2013

Darmstadt 2013

D17

Abstract

The discovery and synthesis of new polymorphs of solids is one of the most attractive tasks for chemists in the development of new materials. To transfer the current synthesis means from empirically random search to rational design based on theoretic prediction has become one of the most desired goals in material science. To achieve this requires a systematic study of the free energy of the interesting materials. The present work here will report a transmission electron microscopy study in structure evolution from amorphous to polycrystalline phases of alkaline earth fluorides, by which the energy landscape of the fluoride materials are experimentally explored.

Structural disorder and distortion play a significant role in structure evolution, especially when amorphous phases are involved. An experimentally precise characterization of the disordered structure is crucial for a correct understanding of the phase transformation. An important quantity in such characterization is the so-called pair-distribution function (PDF), which represents the distribution of atomic pair distances in the investigated material and can therefore also provide insight into the structural distortions in crystalline materials. PDF measurements currently gains increasing application in various fields of material science, especially in neutron and X-ray diffraction. In comparison, electron diffraction can be performed in standard transmission electron microscopes and is thus easily accessible. It also offers the possibility of obtaining data from small material volumes which may be crucial in hetero-structured specimens. However, the PDF technique based on electron diffraction is still not a routine as in X-ray synchrotron and neutron radiation measurements due to the difficulties caused by strong dynamic scattering of electrons, inelastic scattering contribution, and difficult large-angle acquisition. This work carefully studied the electron diffraction based PDF technique. Modifications of the technique were focused on the large-angle data acquisition in energy-filtered diffraction experiments and data processing as well as multiple scattering correction, by which the reliability of the experimental PDF was remarkably improved.

In this work, the modified PDF technique based on in-situ electron diffraction was used to investigate the structure evolution in the phase transformation processes of alkaline earth fluorides. By combination of molecular dynamic simulations the experimental PDFs were clearly interpreted. The structure evolution was further comprehended and finally interpreted within the energy landscape concept.

High-resolution transmission electron microscopy, electron energy-loss spectroscopy, and energy-filtered transmission electron microscopy were also involved in the studies for investigation of crystalline structures.

In addition to the experiments, structural modelling based on reversed Monte-Carlo method was studied. An approach based on a modified reverse Monte-Carlo method for overcoming the difficulty caused by the dynamic scattering was reported.

Zusammenfassung

Die Entdeckung und Synthese neuer polymorpher Festkörper mit dem Ziel der Entwicklung neuer Materialien ist eine der wichtigsten Aufgaben in der Chemie. Entscheidend ist hierbei, die zufällige empirische Suche durch rationales Design (basierend auf theoretischen Vorhersagen) zu ersetzen. Um dies zu erreichen, benötigt man eine systematische Studie der freien Energie des interessierenden Materialsystems. In dieser Arbeit wurde mittels Transmissionselektronmikroskopie (TEM) der Strukturübergang von der amorphen zur polykristallinen Phase in Erdalkalifluoriden untersucht. Dies ermöglichte Einblicke in die Freie-Energie-Landschaft der Fluoride.

Strukturelle Fehlordnung und Verzerrung spielen eine wichtige Rolle in der Strukturbildung, insbesondere wenn amorphe Phasen beteiligt sind. Deshalb ist eine genaue experimentelle Charakterisierung der ungeordneten Strukturen entscheidend für das korrekte Verständnis der Phasenübergänge. Dabei spielt die sogenannte Paarverteilungsfunktion (PVF) eine zentrale Rolle. Sie repräsentiert die Häufigkeit von Atompaarabständen im untersuchten Material und erlaubt damit Einblicke in die atomistische Struktur. PVF-Messungen werden speziell in der Neutronen- und Röntgenbeugung in zunehmendem Maße in verschiedenen Bereichen der Materialforschung eingesetzt. Im Gegensatz zu diesen Verfahren kann Elektronenbeugung in herkömmlichen Transmissionselektronenmikroskopen durchgeführt werden welche einfach zugänglich sind. Darüber hinaus kann Elektronenbeugung auf kleine Materialvolumina angewandt werden was für die Untersuchung feinskaliger heterostrukturierter Proben extrem hilfreich ist. Jedoch ist die PVF-Bestimmung mittels Elektronenbeugung immer noch kein Routineverfahren. Dies liegt insbesondere an den starken dynamischen Effekten bei der Beugung von Elektronen, dem Einfluss inelastischer Elektronenstreuung und der Schwierigkeit, große

Streuwinkel zu erfassen. In dieser Arbeit wurden diese drei Probleme untersucht, Lösungen erarbeitet und somit die PVF-Bestimmung mittels Elektronenbeugung optimiert. Dabei kam die energiefilternde TEM zum Einsatz und es wurde eine Mehrfachstreukorrektur angewandt, welche die Zuverlässigkeit der experimentellen PVF deutlich verbesserte.

Mit Hilfe dieser verbesserten Verfahren wurde in dieser Arbeit Elektronenbeugung während des Anlassens (d.h. in situ) von bei tiefen Temperaturen abgeschiedenen Fluoriden durchgeführt. In Verbindung mit molekulardynamischen Simulationen konnten experimentelle PVFen eindeutig interpretiert werden. Die Strukturbildung wurde im Rahmen des Energielandschaftskonzepts interpretiert.

Als ergänzende Methoden zur Untersuchung der kristallinen Phasen wurden die hochauflösende TEM, Elektronen-Energieverlustspektroskopie (EELS) und energiegefilterte Transmissionselektronmikroskopie (EFTEM) eingesetzt. Darüber hinaus wurde Strukturverfeinerung mittels inverser Monte-Carlo-Methoden studiert. Es wurde eine modifizierte inverse Monte-Carlo-Methode vorgestellt, welche zur überwindung der Schwierigkeiten durch die dynamische Beugung beitragen könnte.

Acknowledgements

This work is performed in the Max-Planck-Institut für Intelligente systeme, Stuttgart, Germany in Prof. Dr. van Aken's group in the time between January of 2010 and February of 2013 under the financial support by the German Research Foundation (Deutsche Forschungsgemeinschaft, DFG).

I gratefully acknowledge Prof. Dr. Peter A van Aken who gave me the opportunity to work in his group and supervised my Ph.D. researches. I also thank him very much for his kind support and care.

I also gratefully acknowledge Prof. Dr. Hans-Joachim Kleebe who supported my PhD researches.

I gratefully appreciate Dr. Wilfried Sigle who was my tutor for the passed three years. He supervised my whole work and gave me knowledges from the fundamental to the in-depth. All I learnt from him made me to be competent in scientific researches.

I would like to appreciate Prof. Dr. Christoph T Koch. I got his help at the most difficult time of my research work which was so important and in time. The wonderful discussions with him brought fresh and extensive ideas to me and told me the way how to think.

Here, I also would like to acknowledge my cooperation partners Dr. Andreas Bach and Dr. Dieter Fischer who prepared the MBE specimens for me and helped me for the cold sample transport.

Sridhar Neelamraju, Dr. Nico Totó, Prof. Dr. J Christian Schön and Prof. Dr. Dr. h.c. Martin Jansen are acknowledged due to the theoretical support and cooperation. The simulation results from them helped me to understand my experiments more comprehensively.

I specially thank Dr. Vesna Srot. She not only looks beautiful but also kind heart. She kept encouraging me and bringing me sunshine in both work and daily life.

Dmitry Tyutyunnikov who is a wonderful guy, smart, active, positive, and also modest. He patiently listened my complicated and maybe boring mathematical equations, and brought his own understanding to me. All the discussions with him are nice memories.

Caroline Heer and Dr. Behnaz Rahmati are specially appreciated. They helped me overcame difficulties of living in a foreign country and took care my life like elder-sisters. I can not imagine what would be if they did not appear in my life within the past three years.

I would like to thank Kersten Hahn and Peter Kopold who gave me training for operating the Zeiss and Jeol microscopes individually. Special thank for Kersten's kind invitation of fantastic dinners in his apartment. I enjoyed them a lot.

Kepeng Song, Nengyun Phillipp-Jin, Ute Salzberger, Marion Kelsch and Cigdem Özsoy Keskinbora are acknowledged due to their sincere concern for my work and life in Germany.

I thank Zhen Chen's help for the calculation of EELS core-loss spectra and playing pin-pong games with me at weekend.

What a greatly fantastic group I was in! The passed years has become the most important period in my life. Thanks to God for the wonderful luck!

Finally, I would like to bring my most appreciation to my mother. Her continuous support and encourages gave me a great deal of confidence and power to face any kind of challenges in my life!

Stuttgart, April 2013

Contents

1 Introduction

The knowledge of composition and structure as well as properties of new solid-state compounds leads to essential progress of material science. Discoveries and synthesis of new solid-state compounds is one of the fundamental tasks in solid-state chemistry research. The synthesis approaches up to now are still based on empirical experience. This empirical search of synthesis condition is an extremely time-consuming work and unable to predict existence of naturally non-existing compounds. Therefore, to synthesize the solid-state compounds with well-controlled composition and structure, and hence the desired properties and functions based on theoretical predictions, becomes one of the most desired goals in material science [1–4]. To achieve a rational design of synthesis in solid-state chemistry, two basic steps are necessary: 1. Discovery of the possibly existing compounds and prediction of their structures and properties. 2. Designing a reasonable synthesis route to realize the predicted compounds [5–7]. Within thermodynamic theories, both of the above steps need an understanding the free energy of the investigated material systems. Therefore a systematic pre-study of the energy landscape becomes the key point of realizing the rational synthesis.

Theoretical studies of the energy landscape have been implemented for more than two decades [8–13]. Nevertheless, sampling all points on the energy landscape in theoretical calculation is unachievable with nowadays computing power. Thus, an alternative approach based on the experimental exploration is involved into the studies. One successful method is the so-called low-temperature atom-beam deposition [14]. With such a technique the investigated material is deposited on a low-temperature substrate to form an amorphous structure and then annealed to higher temperature. The annealing induced phase transformations can be observed and recorded by several characterization techniques. The experienced phases correspond to different thermodynamically (meta)stable states of the investigated system, hence the different (locally) ergodic regions on the energy landscape. Accordingly, the energy landscape of the investigated system is eventually explored to a certain extent. This experimental approach has much efficiency and broad applicability on material systems, although it cannot provide the values of the minima and barrier in the observed ergodic region as precise as ab-initio level calculations.

The experimental exploration approach requires high-quality characterization results to obtain accurate and precise structures. One of the challenges is that the starting point of the phase transition has a highly disordered or even amorphous structure. Resolving the disordered structures is quite difficult due to the lack of both experimental techniques and theoretical modelling methods. The present work starts from this point and aims at fixing some of the difficulties. The energy landscape is experimentally explored by evaluating the phase evolution of the investigated materials in case of alkaline fluoride systems. The energy landscape concept and the low-temperature atom deposition techniques as well as the experimental design will be shortly introduced in chapter 2. The material systems will also be shown in this chapter. The predominant work is focused on the characterization of the originally amorphous phase as well as the structure distortion of the phases induced by the annealing process. Energy-filtered electron diffraction, based on transmission electron microscopy, combined with in-situ heating is the main method used in this work for the characterization. The theory of pair distribution function analysis as well as the extraction procedure from the 2-D experimental electron diffraction patterns are discussed in detail in chapter 3. Experimental details will be described in chapter 4. Main results will be reported and discussed in chapter 5 and 6, where the feasibility and reliability of the pair distribution function will be shown. Imaging and electron energy-loss spectroscopy are also used as supplementary techniques. The difficulties resulting from dynamic scattering will be discussed in 7, where a promising method will be proposed to solve the amorphous structure from only experimental electron diffraction data without any theoretical simulation, such as molecular dynamics. This method also takes the multiple scattering effect into account, thus simultaneously fixing the problem of dynamic scattering. Finally, in chapter 8, experimental methods for acquisition of element specific partial pair distribution functions will be shortly discussed, and moreover a brief introduction of other characterization methods for disordered materials will be given. They are considered and tested in this work.

Challenges in this work are as follows:

1. In-situ experiments: low-temperature transport of the materials which are sensitive to both temperature and air.
2. Radiation damage: the structures (especially the metastable phase) of the materials are very beam sensitive.
3. Characterization of irregular structures in the experiment: distinguishing disordered amorphous phases from distorted crystalline phases. This makes high-resolution transmission electron microscopy (HRTEM) and traditional diffraction impossible.
4. Dynamic scattering of the electron beam: it degrades the reliability of the experimentally measured pair distribution function.
5. Structure modelling of the disordered phase: difficult to gain a physically reliable model to explain the experimental data. It correlates to point 3 and increases the difficulty of this work.

This thesis will show that points 1, 2, 3, and 5 are finally overcome and point 4 is fixed by the proposed method in chapter 7.

The work presented in the following chapters has been partially published:

- Xiaoke Mu, Sridhar Neelamraju, Wilfried Sigle, Christoph T. Koch, Nico Totó, J. Christian Schön, Andreas Bach, Dieter Fischer, Martin Jansen, and Peter A. van Aken, *Evolution of order in amorphous-to-crystalline phase transformation of* MgF_2, Journal of Applied Crystallography **46** (2013), 1105–1116.
- Xiaoke Mu, Wilfried Sigle, Andreas Bach, Dieter Fischer, Martin Jansen, and Peter A van Aken, *Influence of a second cation* ($M = Ca^{2+}$, Mg^{2+}) *on the phase evolution of* $(Ba_x, M_{1-x})F_2$ *starting from amorphous deposits*, submitted (2013).
- Xiaoke Mu, Andreas Bach, Wilfried Sigle, Dieter Fischer, Martin Jansen, and Peter A. van Aken, *A study of structural evolution of alkaline earth fluorides*

from amorphous to polycrystalline phase by in-situ TEM, MC2013 Regensburg, Germany (2013).

- Xiaoke Mu, Sridhar Neelamraju, Wilfried Sigle, Christoph T. Koch, Nico Totó, J. Christian Schön, Andreas Bach, Dieter Fischer, Martin Jansen, and Peter A. van Aken, *TEM study of the structural evolution of ionic solids from amorphous to polycrystalline phases in the case of alkali difluoride systems*, EMC2012 Manchester (2012), 0493.

- Xiaoke Mu, Wilfried Sigle, Andreas Bach, Dieter Fischer, Nico Totó, Sridhar Neelamraju, J. Christian Schön, Martin Jansen, and Peter A. van Aken, *Electron diffraction analysis of the structural evolution of MgF2 from an amorphous phase to a polycrystalline modification*, Proceedings MC2011 Kiel (2011), 163.

- Andreas Bach, Dieter Fischer, Xiaoke Mu, Wilfried Sigle, Peter A. van Aken, and Martin Jansen, *Structural evolution of magnesium difluoride: from an amorphous deposit to a new polymorph*, Inorganic Chemistry **50** (2011), 1563–1569.

Symbol	Description
N	total number of atoms
E_{free}	free energy
U_p	potential energy
U_k	kinetic energy
P	pressure
V	volume
T	temperature
S	entropy
ρ_0	average atom density
$\vec{q}$	scattering vector
θ	scattering semi-angle ($\theta = \lvert\vec{q}\rvert/2$)
s	$s = 2\sin\theta/\lambda$ (λ is electron wavelength)
ϕ	azimuthal scattering angle
$f(s)$	electron scattering factor
$\varphi(r)$	structure factor
r	atomic pair distance
$P(r)$	(raw) pair distribution function (PDF)
$G(r)$	(reduced) PDF
$G_{ave}(r)$	elemental signal averaged PDF
$G_{i-j}(r)$	partial PDF (element specific between species i and j)

Table 1.1: Definition of the common symbols used in this work

2 Energy landscape and experimental explorations

2.1 Energy landscape

Each atom in a given material (or system) containing N atoms can be described by its position vector in three-dimensional (3D) space. Thus, the whole system can be described by one $3N$ -dimensional Euclidean space where the base axes are constructed by the three elements of the position vectors of all atoms, so-called configuration space. A determined structure of the given system is one point of the configuration space. The potential energy, which gives the dynamic properties of the system, is dependent on the structure of the system, i.e. the positions of the atoms. Thus, the potential energy is a function of the configuration space and can be depicted as a hypersurface over the 3N-demensional configuration space. This potential energy hypersurface containing energy minima and maxima is commonly called energy landscape [6, 7, 9, 15–17].

Figure 2.1 [6] gives a schematic view of an example of an energy landscape, where the horizontal X_1 and X_2 axes represent the configuration space; the vertical axis represents the potential energy; the three valleys, marked by three different colour dots, represent three minima on the energy hypersurface. The valley marked by a green dot has the lowest energy (see the projected colour dots on the vertical E axis) corresponding to a global minimum of the energy landscape and is associated with a dynamically stable state, i.e. the thermodynamically stable phase of the material (or system). The other two valleys correspond to local minima of the energy landscape and relate to kinetically stable states, i.e. two thermodynamically metastable phases. High-energy regions, namely the mountain of the landscape, represent dynamically unstable states. They are normally

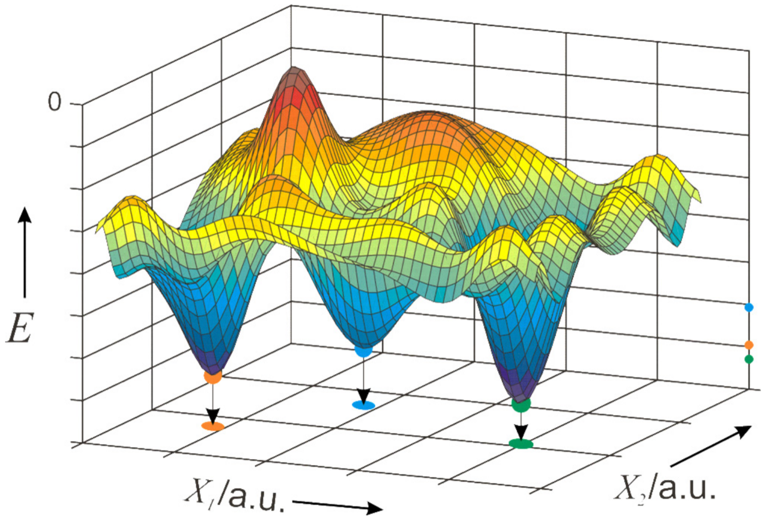

Figure 2.1: Sketch of an energy landscape [6], the hypersurface of the potential energy versus the $3N$-dimensional configuration space. The horizontal X_1 and X_2 axes represent the configuration space. The vertical axis represents the system potential energy.

considered to be highly disordered structures, i.e. they can be associated to disordered or amorphous phase.

A material with determined structure (for instance a perfect crystalline structure) will be located on its corresponding point (one minimum) of the energy landscape at 0 K. At higher temperature, the structure-point will start to randomly move around in the nearby relatively low-energy ergodic regions which contain many local sub-minima corresponding to defect structures. The random walk among the energy sub-minima points represents structure transitions between different defected structures, but be blocked by surrounding mountains, i.e. energy barriers. Then this material is denoted as being in a thermodynamically (meta)stable phase. The kinetic energy as well as the entropy term in the system free energy can be interpreted as the degree of the mobility of structure transitions. The mobility within the energy landscape will increase by raising the temperature. The structure can escape from the stable phase when the mobility is larger than the energy barrier around the minimum. Then, the structure of the material can reach another minimum on the energy landscape which is much deeper than the previous one and might be trapped by this minimum if it is deep enough. The material then transforms to another phase.

Therefore, a good understanding of the energy landscape can predict the existence of new compounds, usually related to metastable modifications, by judging the depth and height of the corresponding minimum and barriers. Furthermore the energy landscape can even be used to depict phase diagrams [17, 18], hence, help the experimentalists to develop a rational synthesis route to achieve the compounds with desired structures.

2.2 Low-temperature atom-beam deposition

The ultimate aim of exploration of the energy landscape is based on the theoretical computation on the ab-initio level without need for experimental data [8–12, 17]. However, to sample all points in the configuration space by computation is impossible with nowadays computation power, even when searching local minima and nearby barriers. Therefore experimental data as a complement, to explore the energy landscape and validate the theoretical calculation and prediction, becomes necessary [6, 7, 19, 20].

One technique for this aim is so-called low-temperature atom-beam deposition (LT-ABD) [14] that has been successfully applied to the synthesis of new alloys [21, 22], nitrides [23, 24], and halides [20, 25–27].

Figure 2.2 shows an ultra-high vacuum (UHV) chamber used for the LT-ABD. The substrate can be cooled down to liquid nitrogen (77 K) or liquid helium (4 K) temperature by the cooling system on the substrate holder. The investigated materials can be heated up to vaporize in the effusion cell to form an atomic steam flowing toward the substrate. The emitted atoms, because of the low-temperature substrate, will lose most of their kinetic energy when they touch the cold substrate. These atoms consequently stick on the cold substrate at random sites and thus form a structure resembling a random network, i.e. an amorphous phase. The free energy of this random network corresponds to a relatively high energy on the energy landscape compared to its crystalline counterparts. The deposited atoms cannot rearrange their positions sufficiently due to the reduced mobility, i.e. the amorphous structure is frozen and the structure point on the energy landscape cannot overcome the nearby barriers to reach a lower energy level. By heating the substrate atoms of the deposit gain energy. As a

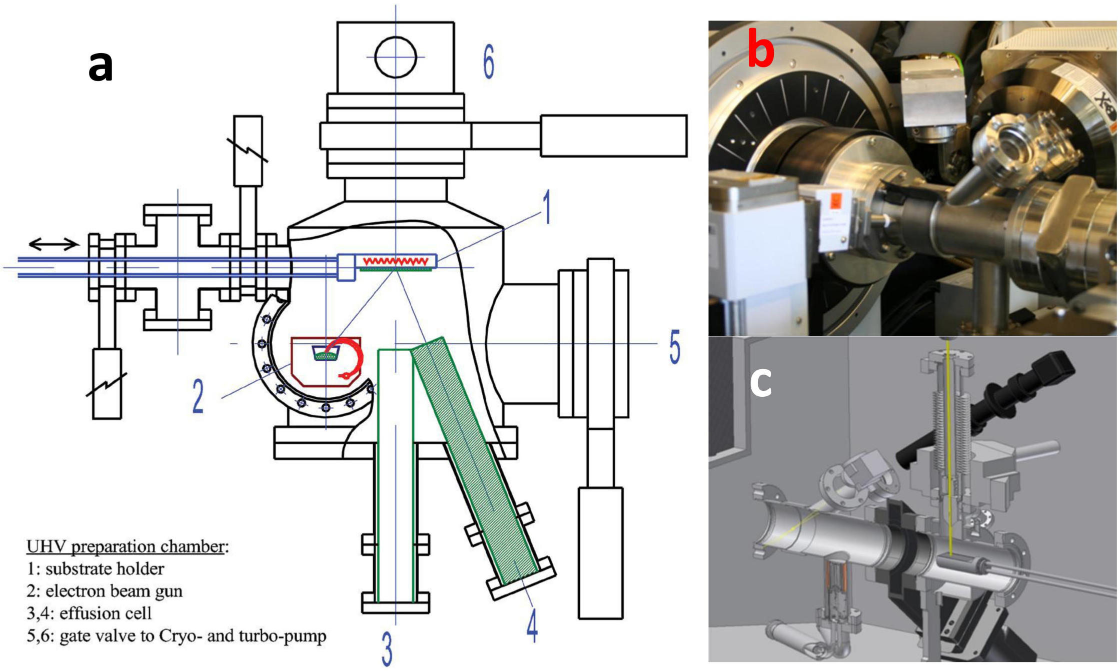

Figure 2.2: (a) Schematic view of the ultra-high vacuum chamber used for the low-temperature atom-beam deposition and the experimental setup. (b) X-ray diffractometer and (c) Raman spectroscope for in-situ structure characterization.

result, the system overcomes surrounding barriers on the energy landscape to reach a lower energy region. A local minimum would correspond to a metastable state of the material. At further heating, the atoms in the deposit will gain even higher energy. The structure point on the energy landscape hence can escape from the local minimum and finally reach the global minimum which corresponds to the stable phase of the material. At even higher temperature, the structure point on the energy landscape will escape from any global minimum and the material reaches the melting or gaseous phase. The energy landscape of the material is thus able to be partially explored by the above process. Furthermore, the metastable structure can be synthesized by the low-temperature deposition followed by high-temperature annealing technique.

The amorphous deposit with the cold substrate can then be transferred for further characterization, e.g. by X-ray diffraction (XRD) [28] (Fig. 2.2b), Raman spectroscopy

(RS) [29] (Fig. 2.2c) and transmission electron microscopy (TEM) (Fig. 4.1c), to monitor the structure evolution during in-situ heating.

2.3 Motivation of this work

Trying to understand the processes involved in the LT-ABD method requires a detailed understanding of the structure evolution of the deposited materials, especially the initial amorphous phase. The challenge is to study the atomic structure of the amorphous phase and also the distortion of the subsequently annealed crystalline phases. In contrast to XRD and RS, TEM offers much higher spatial resolution. Most importantly in this work electron diffraction based on TEM offers significantly higher scattering angle information than normal laboratory XRD due to the large scattering cross-section. This large angular information gives the possibility for the characterization of strongly disordered structures.

Electron beam diffraction is used as the main experimental method to measure the so-called pair distribution functions of the investigated materials. By combining with molecular dynamic simulations the atomic structures of the initial amorphous phases of the deposited materials as well as the subsequently polycrystalline phases are studied. This allows the evaluation of the structure evolution and eventually draw out the energy landscape of the investigated materials. Some other TEM techniques, such as high-resolution imaging (HRTEM) and electron energy loss spectroscopy (EELS) are also applied as complementary methods.

2.4 Material systems

The materials studied in this work are alkaline earth fluorides (Fig. 2.3, highlighted by the violet circles) because they are more ionic which makes the theoretical MD investigation to be more reliable. They are also structurally diverse due to the double fluorine configuration comparing the alkaline fluorides.

The pure binary MgF_2, CaF_2, SrF_2, and BaF_2 are investigated separately in this work. The results of MgF_2 will be presented in chapter 5. It expresses different behaviour from

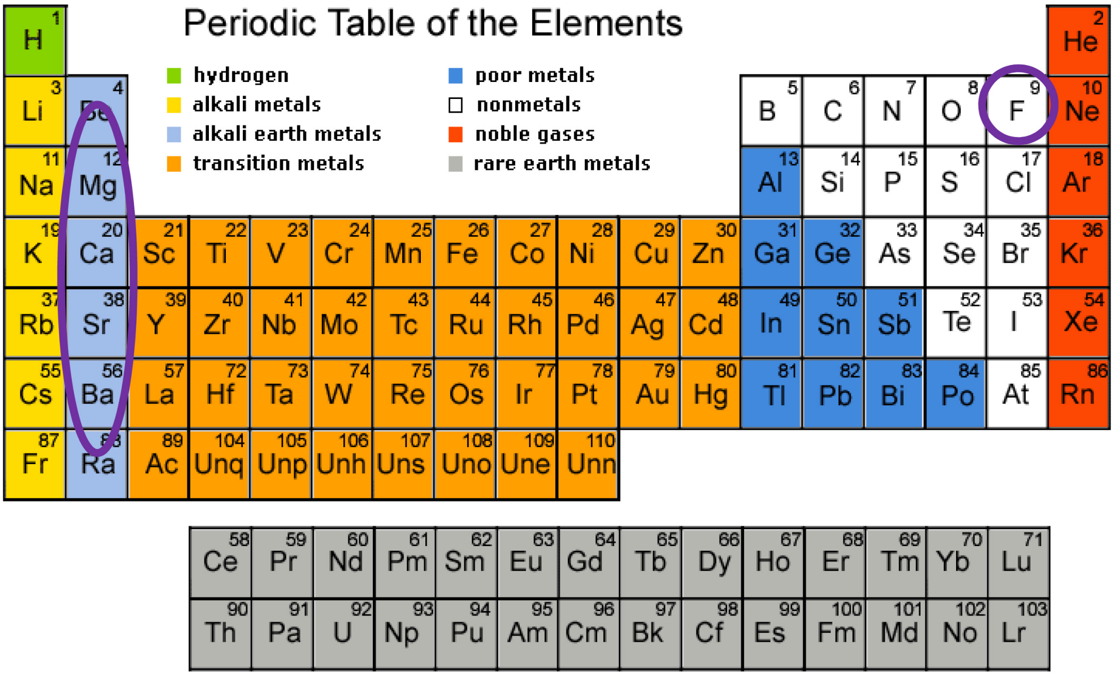

Figure 2.3: The studied materials are alkaline earth fluorides. The used elements are highlighted in this periodic table by the violet circles. The periodic table is taken from [30]

other alkaline earth fluorides in the experiments. Results of other alkaline earth fluorides will be shown in chapter 6, section 6.1.

Apart from the binary fluorides, ternary mixtures of the above compounds are also investigated. By considering the differences between the MgF_2 and others, the mixture between CaF_2 and BaF_2 (homo-structural mixing) and the mixture between MgF_2 and BaF_2 (hetero-structural mixing) are investigated in this work.

3 Characterization of disordered structures by the pair distribution function

3.1 Pair distribution function

The structure of the amorphous phase has puzzled materials scientists for a long time. It is believed that because of the constrained bonding distance and bonding angles the amorphous phase should also show short-range order. However, the characterization of amorphous structures is still a great challenge. One possible way of characterizing them makes use of the fact that amorphous structures are isotropic when averaged over large areas. The so-called pair distribution function (PDF) shows the probability of finding a possible atomic pair against the corresponding pair distance in the system, so it represents the distribution of atomic pair distances in the investigated material and can therefore also provide insight into the structural distortions in crystalline materials.

The structure of a system containing N atoms can be described by $\Re(\hat{r}_1, \hat{r}_2, ..., \hat{r}_N)$, where $\hat{r}_n$ are the 3D coordinates of the position of atom n. Therefore, a function can be defined [31–33]

$$P(\hat{r}) = \sum_{m}^{N} \sum_{n \neq m} \delta(\hat{r} - \hat{r}_{mn}) \tag{3.1}$$

where, $\hat{r}_{mn} = \hat{r}_n - \hat{r}_m$ is the vector from a specified atom m to atom n, r_n is the position of the atom n. The function $P(\hat{r})$ is a 3D function representing distributions of the pair vectors among all atoms, i.e. a 3D-PDF, and thus offers a certain extent of characterization for the investigated structure. Assuming that the structures of the amorphous and nanocrystalline materials are isotropic when averaged over large volumes, i.e. assuming that the distribution of atomic pairs has the same value in different directions, the 3D-PDF defined above is hence reduced to one dimension (1D):

$$P(r) = \sum_{m}^{N} \sum_{n \neq m} \delta(r - r_{mn}) \tag{3.2}$$

where, $r_{mn} = |r_n - r_m|$ is the pair distance between the specified atom n and the atom m.

Figure 3.1 demonstrates the 1D-PDFs in different systems. Notably owing to the disordered atom arrangement in the amorphous structure (Fig. 3.1c, left) the 1D-PDF (Fig. 3.1c, top right, red solid line) shows oscillations of broad peaks instead of the discrete delta (δ) functions in Eq. 3.2.

However, the PDF defined here contains shape information of the investigated material because of the summation in the Eq. 3.2 (also Eq. 3.1) over all atoms in the sampled volume of the material. The shape information in $P(r)$ will become more pronounced when the sampled volume is small, such as in nanoparticles. Thus a new function is defined here [32, 33]:

$$G(r) = \frac{1}{4\pi r}\left[\frac{1}{2N}P(r) - 4\pi r^2 \rho_0\right] = \frac{1}{4\pi r}\left[\frac{1}{2N}\sum_{m}^{N}\sum_{n \neq m} \delta(r - r_{mn}) - 4\pi r^2 \rho_0\right] \tag{3.3}$$

where ρ_0 is the average atom density of the material and the term $4\pi r^2$ ($r \in \Omega$, Ω is the set of all possible r_{mn}, this Ω contains the restriction of the material's shape) subtracts the shape information of the sampled volume from the 1D-PDF. Therefore, $G(r)$, contains only the fluctuations of the atomic pair distribution with respect to the average atomic density ρ_0 in the material, demonstrated by Fig.3.1c (bottom right). $G(r)$ is called the reduced pair distribution function. The peaks of the reduced PDF curve (Fig.3.1c, bottom right) represent local maxima of the probability to find atom pairs with the distance corresponding to the value of the peak positions, in other words the local maxima of the atomic radial density. Therefore the reduced PDF can depict the structural properties of the disordered materials. Eq. 3.3 is then used to characterize the amorphous and nanocrystalline structures.

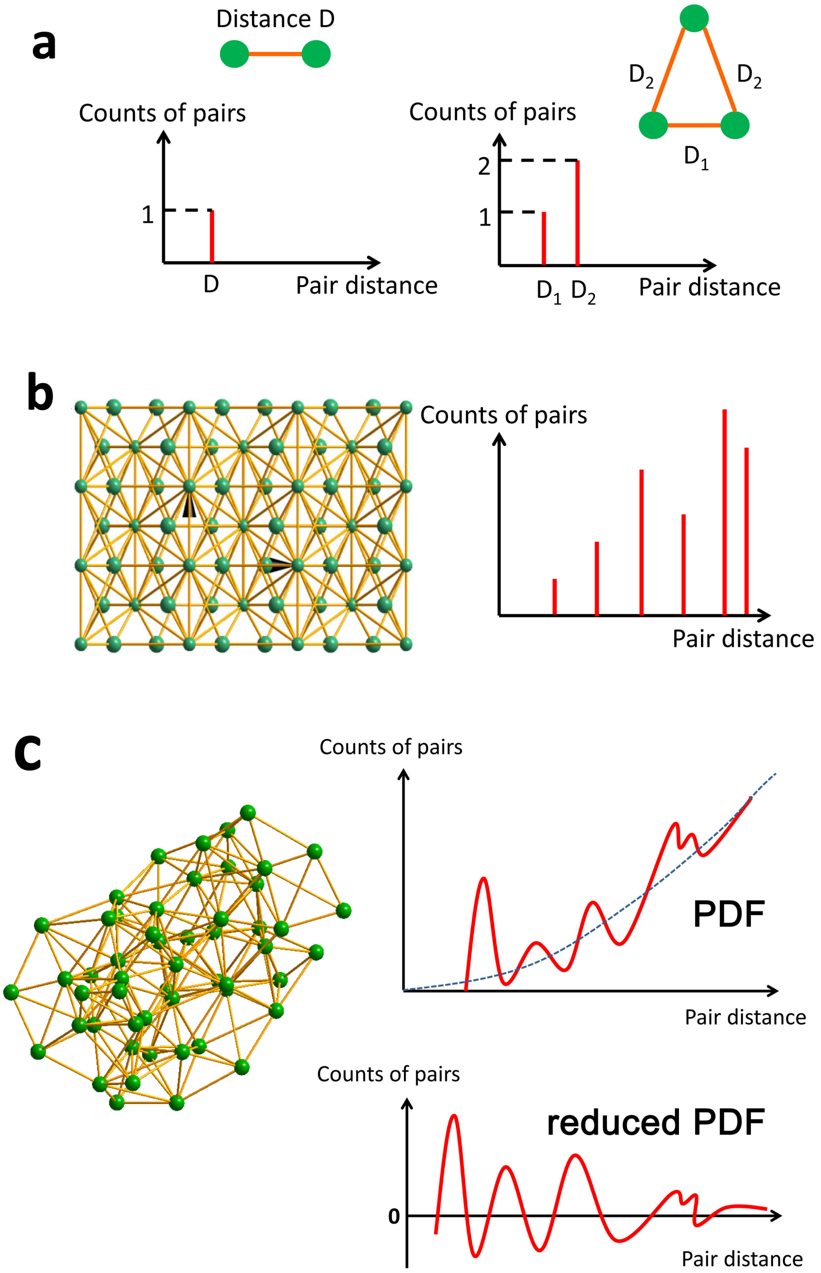

Figure 3.1: Demonstration of 1D-PDFs (red solid lines) for the simplest case of two (a, left) and three atoms (a, right), a crystalline structure (b, right) and an amorphous structure (c, top right) as well as its reduced PDF (c, bottom right). The horizontal axes represent the atomic pair distance. The vertical axes represent the amount of pairs against the distance. The dark-blue dashed line in c (top right) corresponds to the average density term $4\pi r^2\rho_0$.

Experimental measurement of PDFs is a routine task in neutron [34, 35] and X-ray diffraction [32, 36, 37] as well as in the extended X-ray absorption fine structure (EXAFS) spectroscopy [38, 39], although developments and improvements in the methodology still continue [40–43]. It is also possible to obtain the PDF from electron diffraction, especially in combination with zero-loss electron energy filtering to eliminate inelastic scattering contributions [44–47]. One advantage of electron diffraction is that it can sample very small volumes [48]. The PDF technique is in increasingly wide application in various fields of material science [49–51] to analyse the disordered structures, especially in the currently hot topic of energy materials [52–57].

The PDF technique used in this work is based on electron diffraction experiments performed in the TEM. They are applied to characterize the structure of the amorphous phase of the low-temperature deposits and the subsequently annealed nanocrystalline phases.

3.2 Transmission electron microscope

Electrons emitted from either a heated LaB_6 or from heated/non-heated field-emission filaments are accelerated to a high energy. More detailed description can be found in textbooks [58, 59]. Figure 3.2 left shows the basic configuration of a transmission electron microscope [60] and the imaging-mode ray diagram. The condenser 1 and 2 demagnify the filament cross-over. The condenser 3 projects the demagnified filament cross-over onto the front-focal plane of the pre-objective lens so that a parallel illumination forms on the specimen.

As figure 3.2b shows, if there is a specimen inside the microscope, a fraction of the parallel incident electron beam is scattered by the specimen. The objective lens focuses parallel electrons at one position on the back focal plane. Thus, the intensity distribution on the back focal plane represents the angular distribution of electrons, i.e. the diffraction pattern. An image of the illuminated specimen area is formed in the image plane of the objective lens. The objective lens plays the role of a Fourier transformer. It transforms the electron wave exiting from the specimen (real-space coordinates) to the diffraction plane on the back-focal plane (spatial frequency coordinates).

In the image mode, the lower projection system (intermediate lenses plus projection

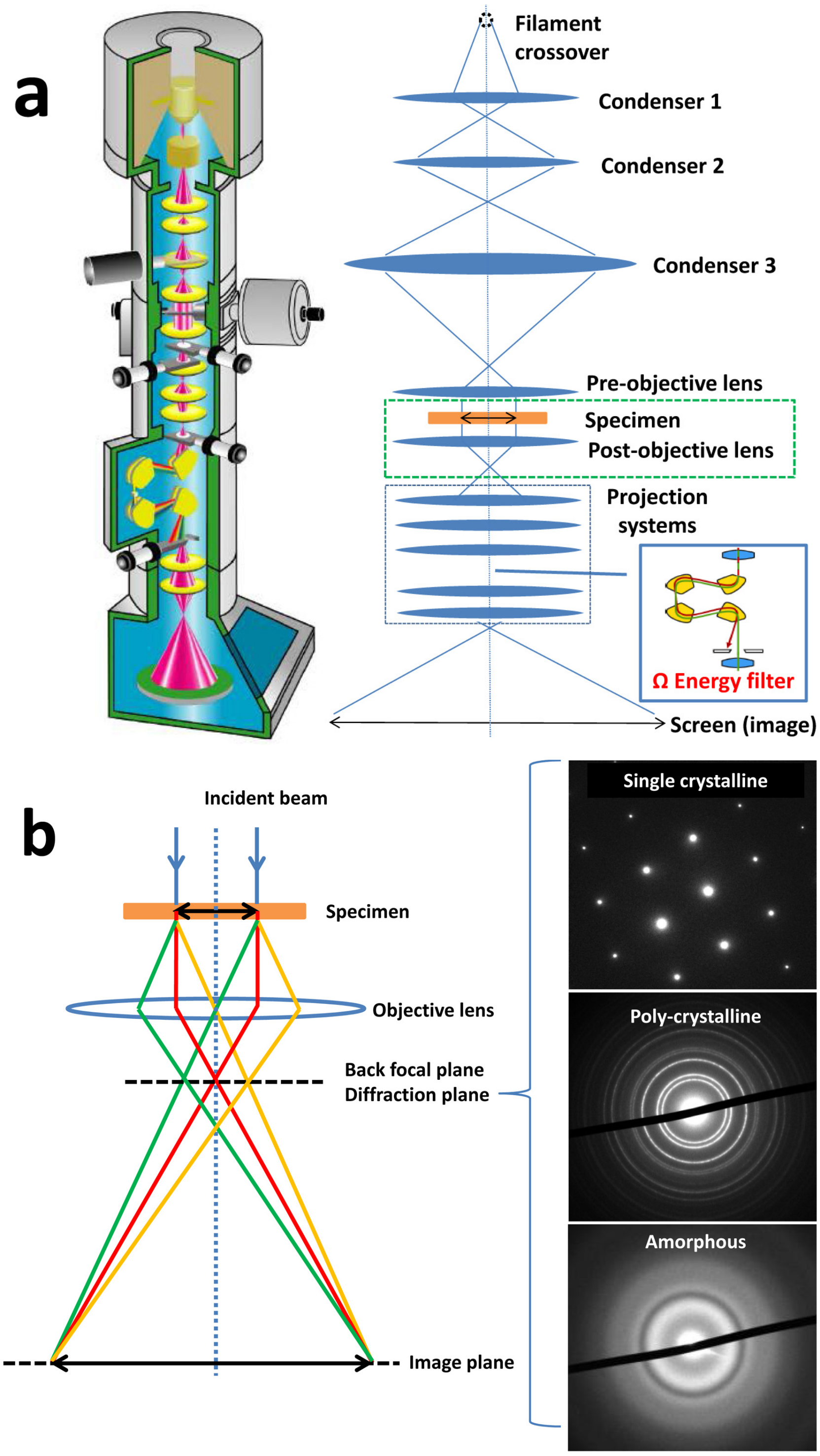

Figure 3.2: (a) Left: sketch of a transmission electron microscope; right: ray diagram of the microscope shown in the left (based on Zeiss EM912 Ω [60]). (b) Left: the detailed ray diagram near the objective enlarged from the dashed green box in (a, right). Right: example of diffraction patterns.

lenses) projects the image plane of the objective lens on the screen (or camera). In the diffraction mode, the projection system projects the back-focal plane of the objective lens on the screen (or camera).

In the Zeiss EM 912, an Ω-shaped energy filter, shown in the insert of Fig. 3.2a (right), is mounted between the intermediate lenses and projection lenses. Electrons with different energy are deflected differently by several static magnetic fields inside the filter. Electrons with specific energies can be selected to form energy-filtered images or diffraction patterns by controlling the width and position of a slit located in the spectrum plane of the filter. In this project, diffraction patterns are recorded from elastically scattered electrons by allowing only electrons with zero energy-loss to pass the filter.

3.3 Pair distribution function from electron diffraction (theoretical background)

The diffraction intensity is generated by the interference of scattered electron waves and can be described by the Debye formula:

$$I(s) = \sum_{m}^{N} f_m(\hat{s})^2 + \sum_{m}^{N} \sum_{n \neq m} f_m(\hat{s}) f_n(\hat{s}) e^{2\pi i \hat{s} \hat{r}_{mn}} \tag{3.4}$$

where N is the number of atoms in the electron-beam illuminated area, f_m is the electron scattering factor of the specified atom m, $\hat{s} = 2\sin\hat{\theta}/\lambda$, where $\hat{\theta}$ relates to the momentum transform of the scattered electrons and to the scalar of value of the scattering semi-angle; $\hat{r}_{mn}$ is, as previously described, the vector from the specified atom m to the atom n.

For a 3D isotropic structure the 3D projection of $\hat{s}\hat{r}_{mn}$ is reduced to a 1D scalar product of sr_{nm} and $e^{2\pi i \hat{s} \hat{r}_{mn}}$ becomes a sinc function after integration of $\hat{s}\hat{r}_{mn}$ over the full solid angle. Then the above formula becomes:

$$I(s) = \sum_{m}^{N} f_m(s)^2 + \sum_{m}^{N} \sum_{n \neq m} f_m(s) f_n(s) \frac{\sin(2\pi s r_{mn})}{2\pi s r_{mn}} \tag{3.5}$$

The first sum on the right-hand side of Eq. 3.5 is the single-atom scattering distribution which is a steadily decreasing function with increasing scattering angle. The second sum contains the structure information of the investigated material and oscillates around the background defined by the first sum.

Here, we use the definition of the reduced-PDF, Eq. 3.3, to replace the discrete term r_{mn} to continuous r, and because of $f_m(s) = f_n(s) = f(s)$ in a single-element compound material, Eq. 3.5 becomes:

$$\begin{aligned} I(s) &= Nf(s)^2 + f(s)^2 \int\limits_0^\infty \sum_m^N \sum_{n\neq m} \delta(r - r_{mn}) \frac{\sin(2\pi sr)}{2\pi sr} dr \qquad (3.6) \\ &= Nf(s)^2 + f(s)^2 \int\limits_0^\infty 8\pi r N G(r) \frac{\sin(2\pi sr)}{2\pi sr} dr + f(s)^2 \int\limits_0^\infty 8\pi N \rho_0 r^2 \frac{\sin(2\pi sr)}{2\pi sr} dr \end{aligned}$$

The term $f(s)^2 \int\limits_0^\infty 8\pi N\rho_0 r^2 \frac{\sin(2\pi sr)}{2\pi sr} dr$ contains the shape information of the illuminated specimen region. It generates signals located at very small scattering angles ($s < 0.1$ $\mathring{A}^{-1}$) which cannot be detected in the experiment. Therefore, this term can be ignored without any influence of the RDF results. Thus,

$$I(s) = Nf(s)^2 + Nf(s)^2 \int\limits_0^\infty 8\pi r G(r) \frac{\sin(2\pi sr)}{2\pi sr} dr \qquad (3.7)$$

Then

$$\frac{I(s) - Nf(s)^2}{Nf(s)^2} s = 4 \int\limits_0^\infty G(r) \sin(2\pi sr) dr \qquad (3.8)$$

Here we define:

$$\varphi(s) = \frac{I(s) - Nf(s)^2}{Nf(s)^2} s \qquad (3.9)$$

$\varphi(s)$ is called structure factor which can be extracted from the experimentally measured diffraction intensity, $I(s)$, by the equation defined above. Thus the reduced PDF, $G(r)$, is the reversed Fourier sine transform of the structure factor $\varphi(s)$:

$$G(r) = \frac{1}{4\pi r} \left[\frac{1}{2N} P(r) - 4\pi r^2 \rho_0 \right] = 8\pi \int\limits_0^{r_{max}} \varphi(s) \sin(2\pi sr) ds \qquad (3.10)$$

r_{max} is the maximum scattering angle recorded in the experiments.

For multi-component materials, an approximation can be defined, which is

$$\sum_m^N \sum_{n\neq m} \delta(r - r_{mn}) f_m(s) f_n(s) \approx \langle f(s) \rangle^2 \sum_m^N \sum_{n\neq m} \delta(r - r_{mn}) \qquad (3.11)$$

Then Eq. 3.10 is replaced by the elemental averaged structure factor defined below:

$$\varphi(s)_{ave} = \frac{I(s) - N\langle f(s)^2\rangle}{N\langle f(s)\rangle^2} s \tag{3.12}$$

where $\langle f(s)^2\rangle = \sum\limits_i \frac{N_i f(s)_i^2}{N}$ and $\langle f(s)\rangle^2 = \left(\frac{\sum\limits_i N_i f(s)_i}{N}\right)^2$, with i being the element type. Then, the elemental signal averaged reduced PDF can be calculated as

$$G(r)_{ave} = 8\pi \int\limits_0^{r_{max}} \varphi(s)_{ave} \sin(2\pi sr) ds \tag{3.13}$$

$G(r)$ in the above equation consists of signals from element-specific reduced PDFs (partial reduced PDF) which describe the distribution of elemental specific pairs, so here the partial PDF and the partial reduced PDF are defined:

$$\begin{aligned} P_{i-j}(r) &= \sum_{m\in i}^{N_i} \sum_{n\in j}^{N_j} \delta(r - r_{mn}) \qquad (3.14) \\ G_{i-j}(r) &= \frac{1}{4\pi r}\left[\frac{1}{N_i + N_j} P_{i-j}(r) - 4\pi r^2 \rho_{ij}\right] \\ &= \frac{1}{4\pi r}\left[\frac{1}{N_i + N_j} \sum_{m\in i}^{N_i} \sum_{n\in j}^{N_j} \delta(r - r_{mn}) - 4\pi r^2 \rho_{ij}\right] \qquad (3.15) \end{aligned}$$

where the i and j represent elemental species. The ρ_{ij} relate to the average density between elemental species i and j and contain information about the element distribution, the signal of which is located at small angles and can be neglected. To understand the partial reduced PDF, the following decomposition of the intensity caused by the structure in Eq. 3.5 in case of binary materials AB_x is made:

$$\begin{aligned} &\sum_{m}^{N} \sum_{n\neq m} f_m(s) f_n(s) \frac{\sin(2\pi s r_{mn})}{2\pi s r_{mn}} \\ &= \sum_{m\in A}^{N_A} \sum_{\substack{n\in A \\ n\neq m}}^{N_A} f_A^2 \frac{\sin(2\pi s r_{mn})}{2\pi s r_{mn}} + \sum_{m\in B}^{N_B} \sum_{\substack{n\in B \\ n\neq m}}^{N_B} f_B^2 \frac{\sin(2\pi s r_{mn})}{2\pi s r_{mn}} \\ &+ \sum_{m\in A}^{N_A} \sum_{n\in B}^{N_B} f_A f_B \frac{\sin(2\pi s r_{mn})}{2\pi s r_{mn}} + \sum_{m\in B}^{N_B} \sum_{n\in A}^{N_A} f_B f_A \frac{\sin(2\pi s r_{mn})}{2\pi s r_{mn}} \qquad (3.16) \end{aligned}$$

Here the definition of the partial PDF is used to introduce the continuous r as follows:

$$\int_0^\infty \sum_m^N \sum_{n\neq m} \delta(r - r_{mn}) f_m(s) f_n(s) \frac{\sin(2\pi sr)}{2\pi sr} dr =$$
$$\int_0^\infty \sum_{m\in A}^{N_A} \sum_{\substack{n\in A\\ n\neq m}}^{N_A} \delta(r - r_{mn}) f_A^2(s) \frac{\sin(2\pi sr)}{2\pi sr} dr + \int_0^\infty \sum_{m\in B}^{N_B} \sum_{\substack{n\in B\\ n\neq m}}^{N_B} \delta(r - r_{mn}) f_B^2(s) \frac{\sin(2\pi sr)}{2\pi sr} dr$$
$$+2\int_0^\infty \sum_{m\in A}^{N_A} \sum_{n\in B}^{N_B} \delta(r - r_{mn}) f_A(s) f_B(s) \frac{\sin(2\pi sr)}{2\pi sr} dr \qquad (3.17)$$

Then,

$$\int_0^\infty G_{ave}(r) \sin(2\pi sr) dr =$$
$$\int_0^\infty \left[\frac{4N_A f_A(s)^2}{N\langle f(s)\rangle^2}\right] G_{A-A}(r) \sin(2\pi sr) dr + \int_0^\infty \left[\frac{4N_B f_B(s)^2}{N\langle f(s)\rangle^2}\right] G_{B-B}(r) \sin(2\pi sr) dr$$
$$+ \int_0^\infty \left[\frac{2(N_A + N_B) f_A(s) f_B(s)}{N\langle f(s)\rangle^2}\right] G_{A-B}(r) \sin(2\pi sr) dr \qquad (3.18)$$

Then a reverse Fourier transform on both side of the above equation is applied,

$$G_{ave}(r) = \left[\frac{4N_A f_A(s)^2}{N\langle f(s)\rangle^2}\right] \otimes G_{A-A}(r) + \left[\frac{4N_B f_B(s)^2}{N\langle f(s)\rangle^2}\right] \otimes G_{B-B}(r)$$
$$+ \left[\frac{2(N_A + N_B) f_A(s) f_B(s)}{N\langle f(s)\rangle^2}\right] \otimes G_{A-B}(r) \qquad (3.19)$$

This equation reveals that the elemental averaged reduced PDF is a sum of partial reduced PDFs convoluted with the Fourier transform of the terms containing element-specific scattering factors. It is difficult to extract partial PDFs from only one electron diffraction experiment, but it is possible if one can combine diffraction experiments with different scattering power for the same elements, such as combining X-ray and neutron for binary materials. Here we could use only electrons. Therefore, the solution to achieve a deeper understanding of the experimental RDFs in this work is calculating the partial PDFs from molecular dynamic simulation data and comparing them to the experimental results.

A more detailed description of the above equations can be found in D. J. H. Cockayne's work [44, 45], where the reduced-PDF is also called reduced density function (RDF). However, X-ray researchers use the term pair distribution function (PDF) for $G(r)$. To be consistent with X-ray literature, the term pair distribution function (PDF) is kept instead of reduced PDF or RDF in this thesis.

3.4 Derivation of the PDF from real electron diffraction experiments

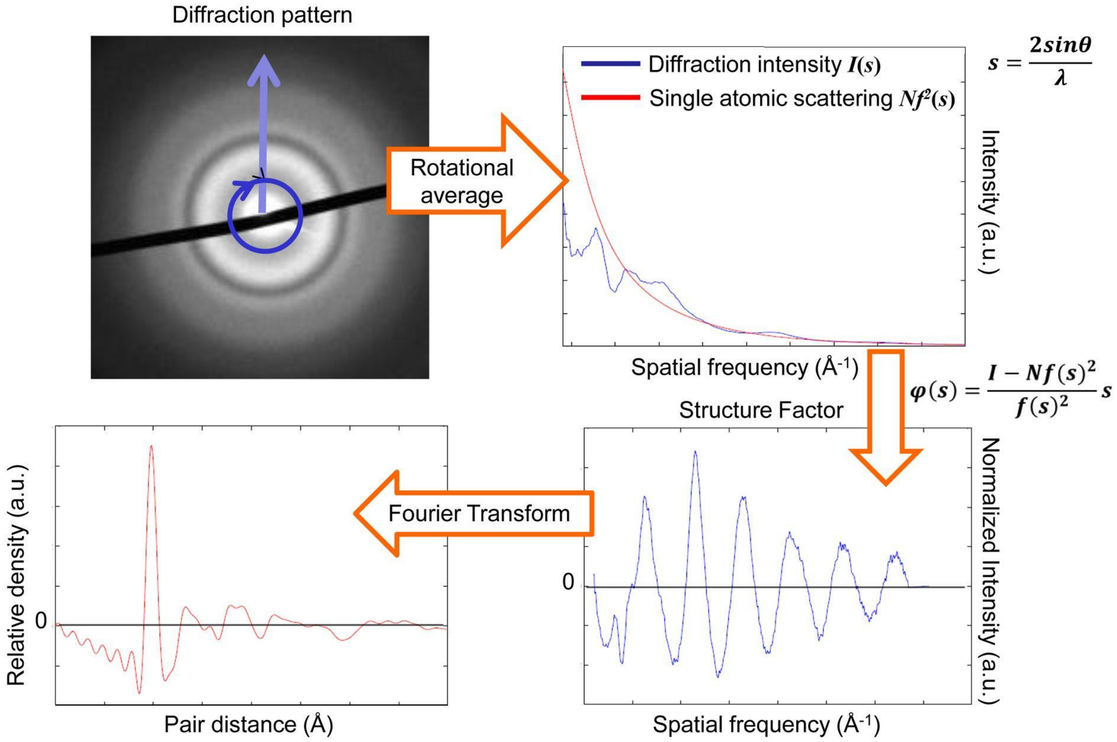

Figure 3.3: Scheme of PDF extraction from diffraction experiment

From electron diffraction experiments circularly symmetric patterns can be obtained. As Fig. 3.3 shows, the electron diffraction patterns are azimuthally integrated and averaged. According to Eq. 3.12, the structure factors are extracted from the experimental diffraction profiles. The PDFs are then calculated according to Eq. 3.13.

The scattering factor of the investigated materials used here is calculated from the parameterized elemental scattering factors [61] with their stoichiometric ratios.

Energy-filtered electron diffraction

The PDF theory is established in the assumption that all electrons are elastically scattered. Although inelastic electron scattering is confined to a small angular distribution in the diffraction pattern, the dynamic process (multiple elastic + inelastic scattering) will remarkably increase the amount of inelastic scattered electrons at high angles. Therefore, the influence of inelastic scattering should be considered.

Figure 3.4 shows an example of diffraction experiments for an amorphous carbon film with around 30 nm thickness. It reveals the difference between experimental energy-filtered and non-filtered diffraction. Figure 3.4a shows that the signal in the small-angle range of the non-filtered diffraction data is more intense than that of the energy-filtered diffraction data. Figure 3.4b shows the extracted structure factors (from the data in Fig. 3.4a), where the main differences are in the small angle region below 1.5 Å^{-1}. These differences result in low-frequency deviation in real space and thus cause differences of peak heights between energy-filtered and non-filtered PDFs. Such differences are demonstrated in Fig. 3.4c. The influence of the inelastic scattering becomes stronger in thicker specimens, such as used in the present project (e.g. the 80 nm thick MgF_2 film in chapter 5).

In the experiment, a 15-eV slit is used for selecting the zero energy-loss of the scattered electrons. The materials investigated in this project are all insulators with valence-conduction band gap larger than 8 eV (note that the zero-loss peak is put at the centre of the slit) so that the selected electrons can be regard as energy-loss free, i.e. purely elastically scattered. The theory in section 3.3 then can be applied in the analysis of the experimental data.

Large-angle acquisition

Residual lens aberrations of the Ω-type energy filter used in the Zeiss EM912 limit the maximum transmission angle in diffraction patterns. Acquisition of diffraction patterns containing both low-angle and high-angle information is impossible. Therefore, in this

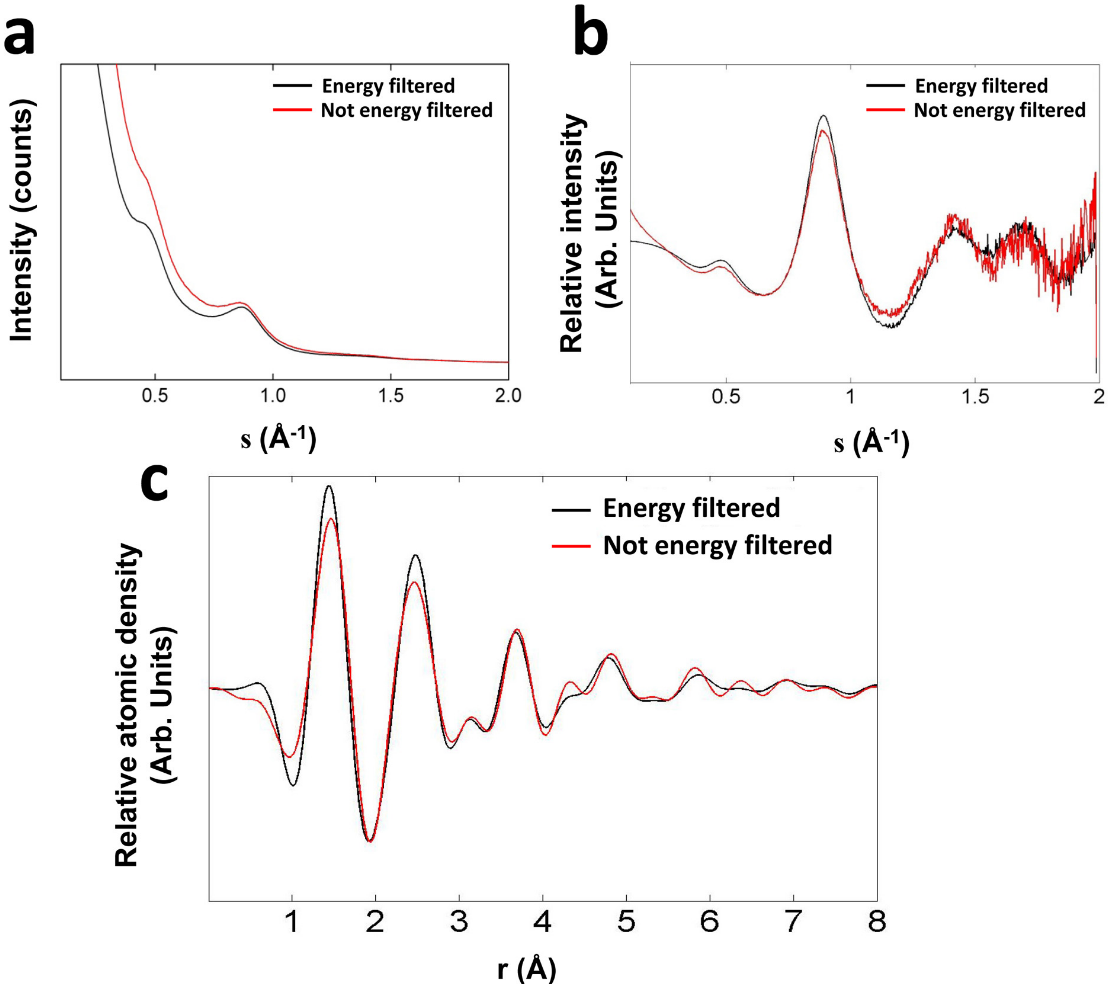

Figure 3.4: An illustration of the effect coming from inelastic electron scattering (data is from a 30 nm thick amorphous Carbon film): (a) electron diffraction profiles from energy-filtered (black) and non-filtered (red) experiments; (b) structure factors extracted from (a); (c) PDFs calculated from the structure factors in (b).

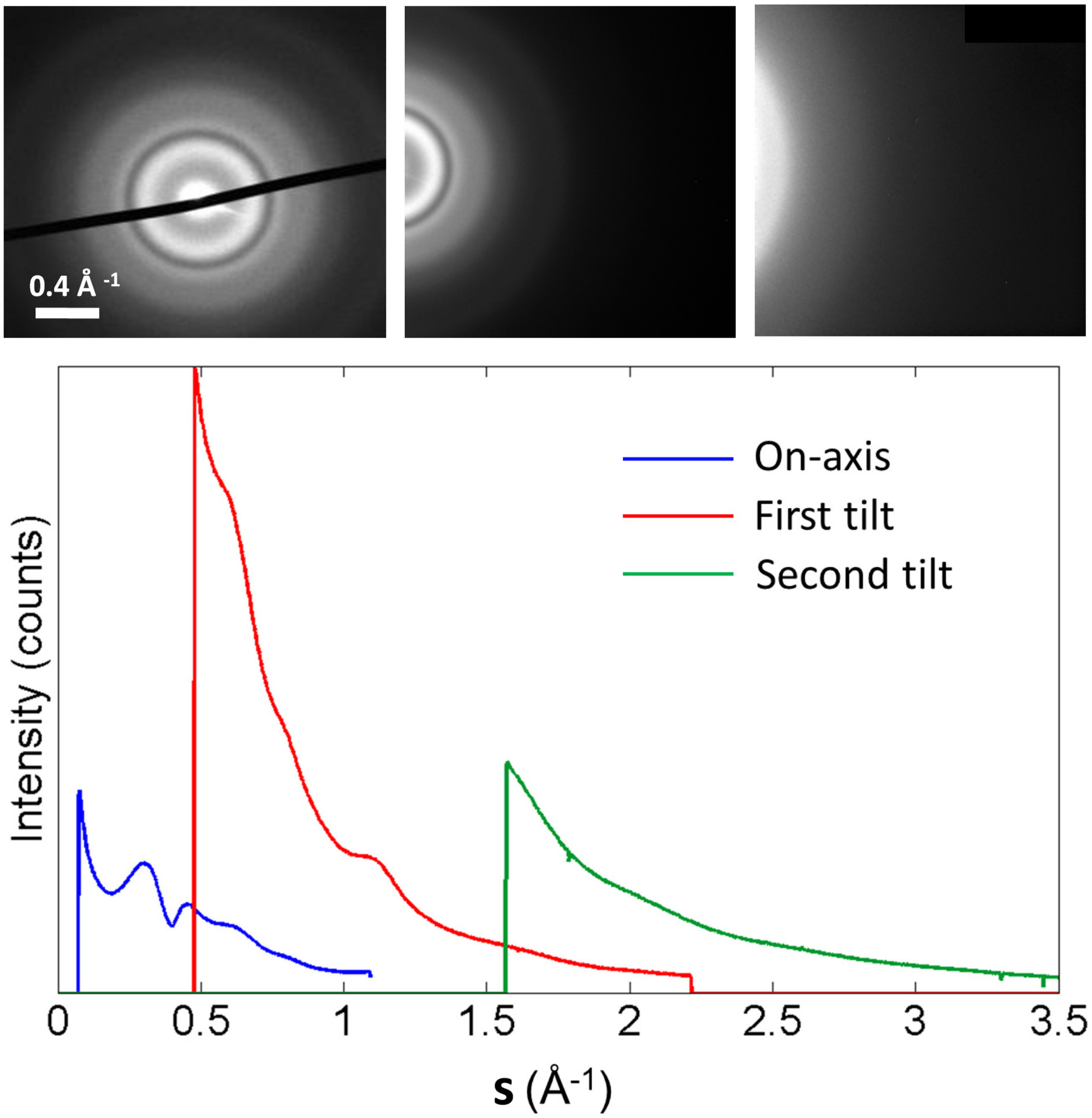

Figure 3.5: Illustration of the high angle acquisition (multi-pattern diffraction acquisition). Top: diffraction patterns at different tilt angles, the on-axis pattern (top left), the first tilt to the intermediate angular range (top middle), and the second tilt to the large angular range (top right). Bottom: diffraction profiles of the different angular ranges, azimuthally averaged from the patterns in the top. Data are from experimental diffraction data of MgF_2.

work, the strategy of beam tilting is used. Three diffraction patterns at different, well-calibrated, illumination beam tilts and with relatively large camera length were acquired and spliced in order to access a large range of scattering-angles, up to 4.5 Å $^{-1}$ (Fig. 3.5 as an example taken from diffraction data of MgF_2). For splicing together the diffraction patterns at different tilt angles, the relative shifted of each diffraction pattern was determined from the prior calibration of the beam tilt. Another advantage of this beam-tilt strategy is that the path of the recorded scattered electrons always passes close to the optical axis of the lens system. This effectively reduces the effect of projector lens distortions.

Improvements of data processing in the extraction procedure

Because of the thickness of the specimen, the effect of multiple scattering in electron diffraction is not negligible. Furthermore, thermal diffuse scattering which has almost zero energy loss cannot be eliminated by energy filtering. Therefore, the diffraction profiles cannot be fitted by the calculated average scattering factor at both small and large angles simultaneously [62, 63], as Fig. 3.6a shows (an example from diffraction data of the MgF_2). The blue line is the experimental diffraction profile and the green line is the calculated average atomic scattering factor. The extracted structure factor, which ideally should oscillate around zero (as shown in Fig. 3.3, bottom right), significantly deviates from zero (Fig. 3.6b, blue line). This deviation leads to a strongly oscillating PDF at small radial distances, as illustrated in Fig. 3.6c (blue line). In order to remove this parasitic low-frequency component, a smooth 4^{th}-order polynomial function was applied to fit the inflection points of the structure factor (Fig. 3.6b, red line). This polynomial function was then subtracted from the structure factor. The new scattering factor hence oscillates around zero, as shown in Fig. 3.6d. The PDF calculated from the new structure factor is shown in Fig. 3.6c (red line), where the oscillation at small radial distance is removed.

The abrupt intensity truncation to zero at larger angles of the measured structure factor can cause high-frequency artifacts in the obtained PDF due to the Fourier transformation. These were minimized by defining a zero crossing of the 4^{th}-order polynomial function as truncation point of the structure factor (as shown in Fig. 3.6b).

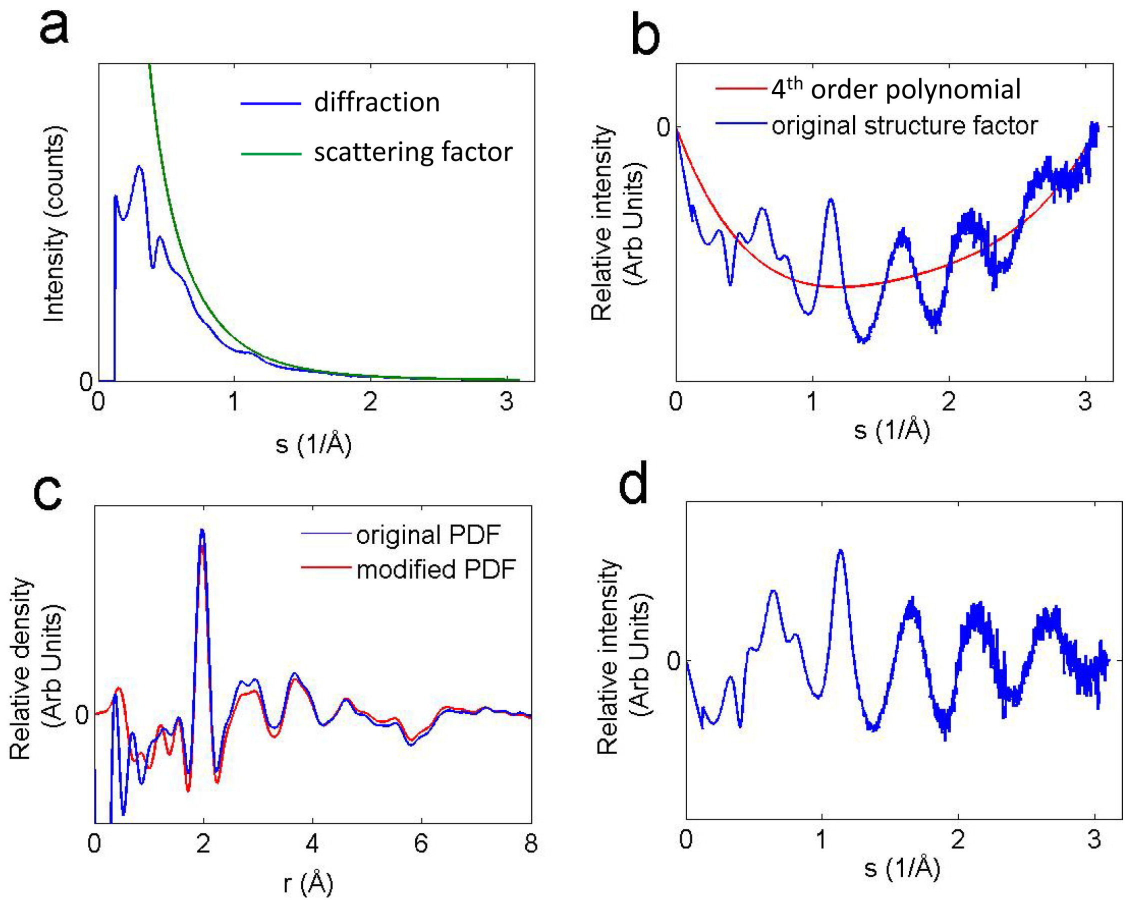

Figure 3.6: An illustration of the effect of multiple scattering and thermal diffuse scattering as well as the details of the modified PDF extraction (diffraction data from MgF_2, 80 nm thick). (a) The diffraction profile from the experiment (blue) and the average scattering factor (green). (b) Structure factor by normalization of the experimental diffraction profile (blue) and the 4^{th} order polynomial fitting (red). (c) Blue: PDF calculated from the raw structure factor in (b, blue line); red: modified PDF calculated from the modified structure factor in (d). (d) The modified structure factor obtained by subtracting the 4^{th} order polynomial from the raw structure factor.

This results in a structure factor that is terminated at large angles at zero intensity (Fig. 3.6d).

The noise of the diffraction data at large angles can cause high-frequency artifacts in the derived PDF. Previously, the noise effect was reduced by applying a damping function [44, 64] to the experimental structure factor. However, the damping function does not only suppress the high-frequency artifacts in PDFs but also reduces the useful information inside the noisy signal. One then loses spatial resolution in the derived PDF. The damping function in reciprocal space is equivalent to a convolution in real space between the PDF and a point-spread function which is the Fourier transform of the damping function itself. Therefore, a splines interpolation of 2^{nd}-order polynomial functions was applied fitting the noisy data at large angle to minimize the noise effect and maximize the real space resolution, instead of multiplying a damping function.

Errors

Diffraction pattern calibration and centre determination of the diffraction patterns cause an error much smaller than ± 0.005 Å at the radial range up to around 5 Å where normally the first, second and third peaks (the first three coordination shells) are located. After the mathematical processes described above, the error caused by multiple scattering, abrupt truncation of the measured data and noise in our experimental PDF is minimized. The real diffraction experiments only extend up to 3.5 Å^{-1} in reciprocal space, instead of an infinite range, due to the fast decrease of the scattering power at large angles and the limited life time of the materials under the electron illumination. The limitation of the finite recording-angle causes an error of the measured PDF, as illustrated in Fig. 3.7.

The effect of the limited angular range is equivalent to a convolution of the true PDF with a sinc function [32] $S = sin(Q_{range} \cdot r)/r$ (Fig. 3.8) where Q_{range} is the maximum recording angle and r is the radius in real space. It includes a pronounced peak at the centre and two tails oscillating around zero. The oscillation strength of the tails is inversely proportional to the recorded angular range. By convolution, the tails from the sinc function contribute redundant oscillations around the true PDF. The redundant oscillations become observable in radial ranges without true signal so that visible artificial peaks are formed (Fig. 3.7a, high-lighted by red arrows for the blue line), whereas these

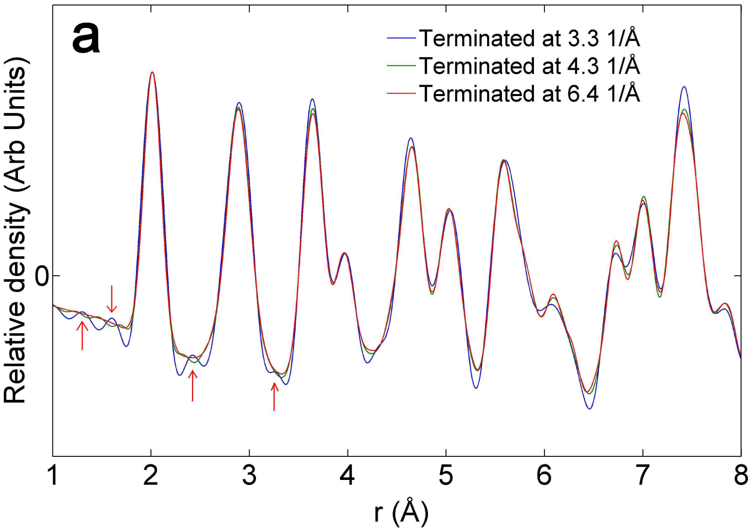

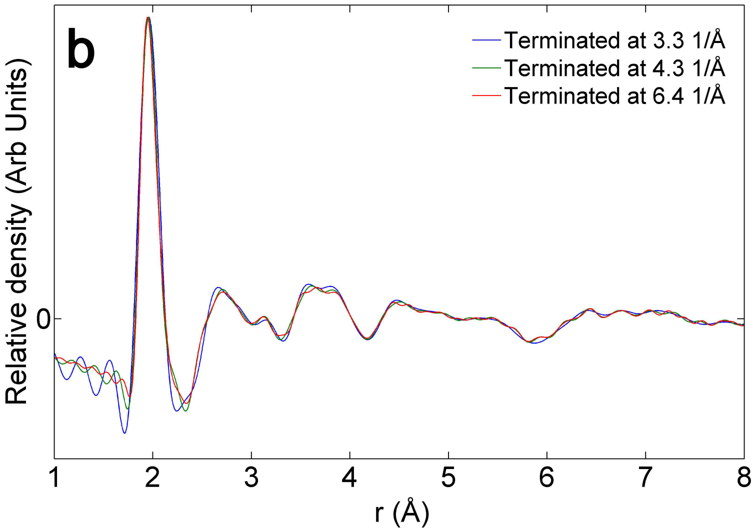

Figure 3.7: (a) PDFs of a $CaCl_2$-type MgF_2 crystalline model with 6150 atoms, Fourier transformed from its structure factor with different truncation ranges; (b) PDFs of an amorphous model with 6150 atoms, Fourier transformed from its structure factor with different truncation ranges.

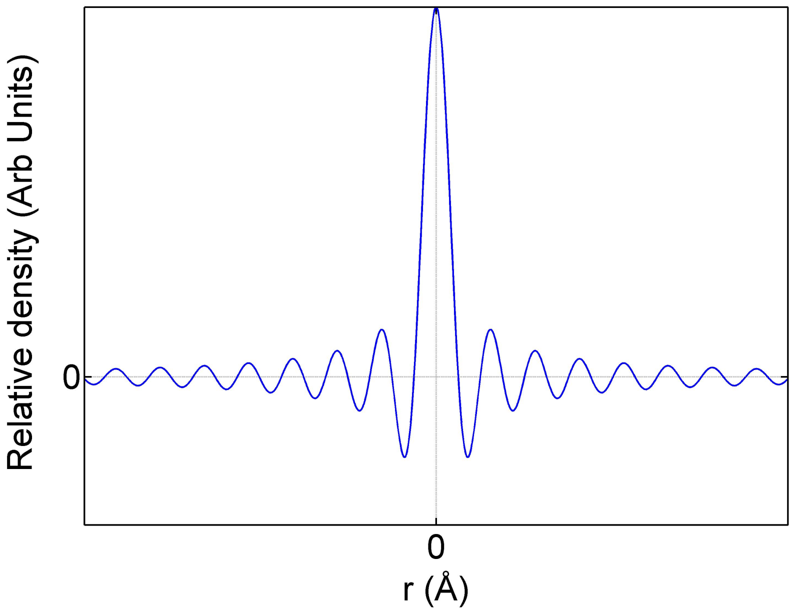

Figure 3.8: A sinc function in the formula of $S = sin(Q_{range} \cdot r)/r$.

artifacts are submerged in the range with strong true peaks and only slightly influence peak positions and heights. The error is small for crystalline materials (Fig. 3.7a). The shift of peak positions is much smaller than 0.005 Å, even in the radial range above 5 Å, because of the sharply pronounced peaks in the crystalline PDF. For the amorphous materials the error is more remarkable (Fig. 3.7b) due to weaker peaks, but still smaller than 0.01 Å in the range between 0 and 5 Å and does not change the tendency of the curves (Fig. 3.7b). In the situation of comparing experimental PDF with theoretical modelling results, all artifacts and, even further, the small peak shifts can be correctly simulated with taking into account of the sinc function (the finite angular recording range) in the PDF calculation.

Overall, the total error bar for the peak positions in the range of the first several pronounced peaks (approximately 0–5 Å) is estimated to be less than ±0.02 Å which was confirmed by repeating the experiments multiple times. The situation can be even better for the first peaks, where the error bar is always smaller than ±0.01 Å.

3.5 Computation of the PDF from a simulated model

To understand and interpret the measured PDF is still far from trivial because only spatially averaged data is provided. A way to circumvent this is to build models of possible atomic structures and compare their PDFs with their experimental counterparts. Such an approach is used, for example, in routines based on molecular dynamics (MD) simulations or reverse Monte-Carlo (RMC) modeling [65–68], possibly accompanied by ab-initio structure relaxation [64, 69, 70]. The advantage of MD is that it allows simulating relatively large volumes and large time scale giving access to the modelling of the (glass) transition from a liquid to the amorphous solid state [71–74]. Therefore, the MD method is chosen to obtain reasonable models for this work

To comparing the experiments with the theoretic simulation results, accurate PDFs calculation from the given models, comparable to the experimental data, is required. There are two ways to obtain the PDF from the atomistic model.

One is based on the PDF definition. First, a PDF (in the definition of Eq. 3.2) is obtained by directly counting the number of pairs against the radial distance between specific atoms. An illustration is given in Fig. 3.9 where partial PDFs in (a) are counted in number of pairs from a rutile-type MgF_2 model with 10×10×10 unit cells; partial PDFs in (b) are counted from an amorphous MgF_2 with a cluster containing 6150 atoms. The obtained partial PDFs are then summed together to obtain the total PDFs shown in Fig. 3.9c,d. Then the total PDFs are subtracted by the averaged density term $4\pi r^2\rho_0$ following Eq. 3.3 to be consistent to the experimental acquisition (the reduced PDF). The final (reduced) PDFs which are compared to the experimental data are then achieved by convolution of the sinc function with Q_{max} in agreement with the experimental setting, shown in Fig. 3.9e,f. This way is routine for cyclotron X-ray diffraction [32, 33, 36], where models are built of infinite size with periodic extension.

However, the above way to calculate PDFs will involve significant deviations from the experimentally obtained PDFs, when the model contains only a few thousand atoms (individual supercells) and/or has medium-scale ($\sim$ 10 Å) density fluctuations. The PDFs directly counted from the supercells will include information of the cell size and shape as well as low-frequency (medium-scale) density oscillations from the average density (Fig. 3.10). However, all this information is missing in the diffraction

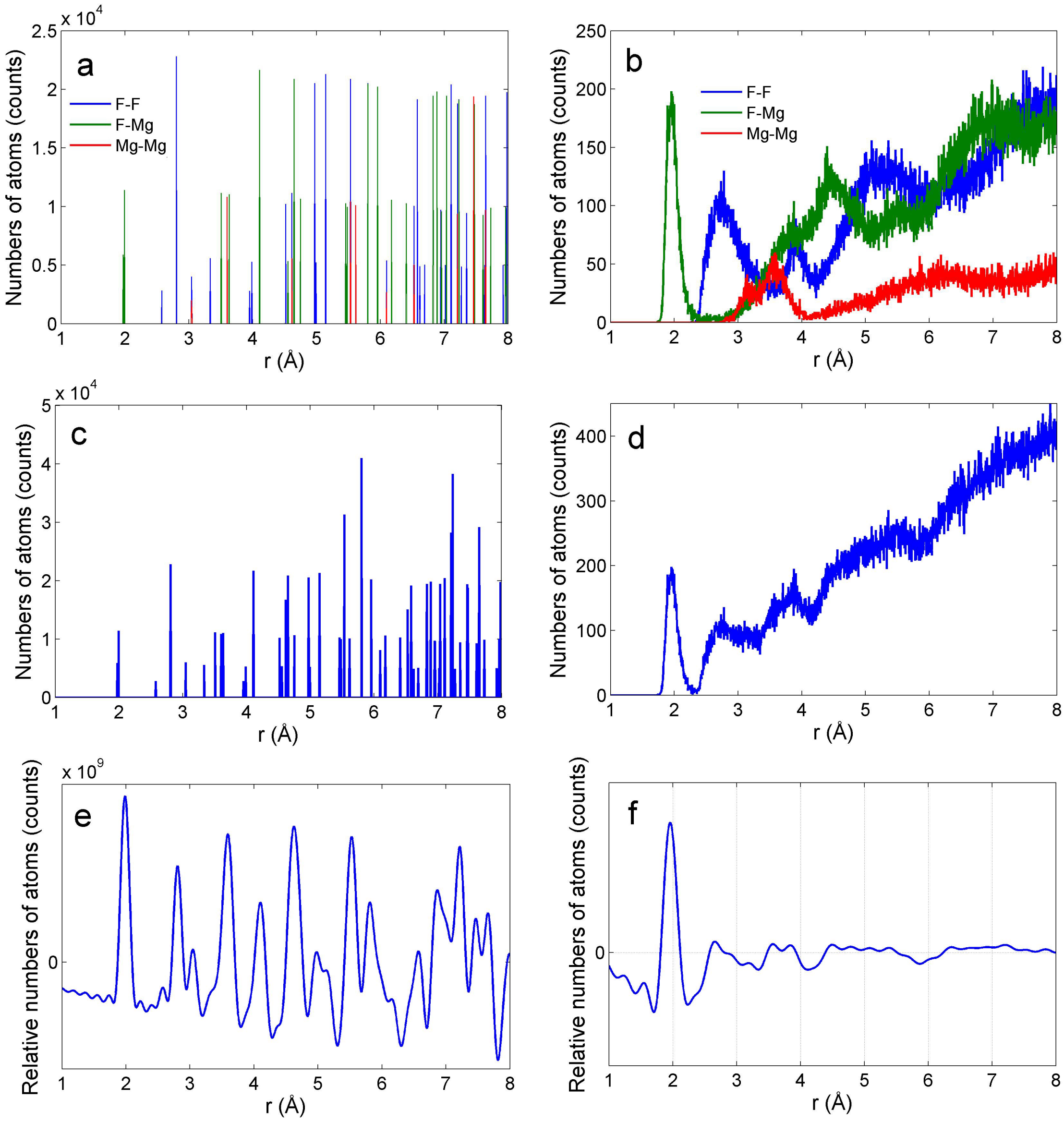

Figure 3.9: Illustration of the direct counting method. Directly counted partial PDFs from models of (a) crystalline rutile-type MgF_2 in the size of $10 \times 10 \times 10$ and (b) amorphous MgF_2 with 6150 atoms. Total PDFs of (c) the crystalline and (d) the amprphous model obtained by summing up all partial PDFs in (a) and (b) weighted with elemental scattering factors. Final (reduced) PDFs of (e) the crystalline and (f) the amorphous model obtained by subtracting the average density term $(4\pi r^2\rho_0)$ from the PDFs in (c) and (d) and convoluting them with the sinc function.

experiments because the small-angle scattering, which contains larger-scale information in real space (hence the information of the shape and size of the sample), cannot be detected. In this work, the models from MD simulations are supercells containing several thousand atoms, and the amorphous model even has an irregular shape and an inhomogeneous density distribution at the medium-scale (Fig. 5.6b). Moreover, to periodically extend the supercells without physical consideration, such as MD or ab-initio-based structural relaxation, could cause seriously false results (chapter 8) due to the loss of structural coherence. Therefore, an alternative way is considered. It is based on the same procedure as was used for the PDF extraction from the experimental data. Namely, one first calculates the kinematical diffraction profile from the MD simulation data by Eq. 3.5 and the element-specific partial intensity according to Eq. 3.16. Then the total PDF and the element-specific partial PDF are extracted by using Eq. 3.13 and Eq. 3.10. This method is actually a simulation of the PDF extraction of experimental diffraction data, and all experimentally related parameters can be taken into account. By considering the difference between the size of the MD supercell and the experimentally observed crystals, the grain-size-related peak broadening in the diffraction profile is taken into account by convoluting a Gauss function $e^{-A_{size}s^2}$, where A_{size} relates to the size

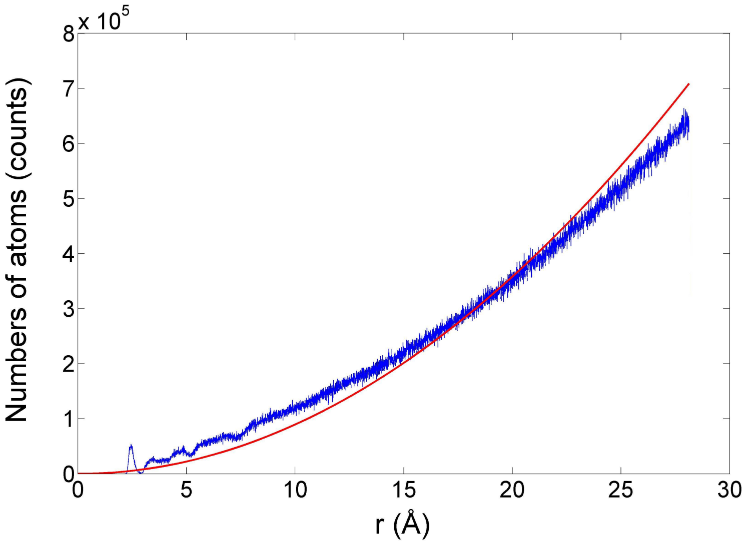

Figure 3.10: An illustration of the amorphous 6150-atom MgF_2 model showing the directly counted PDF (blue) deviating from the average density $(4\pi r^2\rho_0)$ (red).

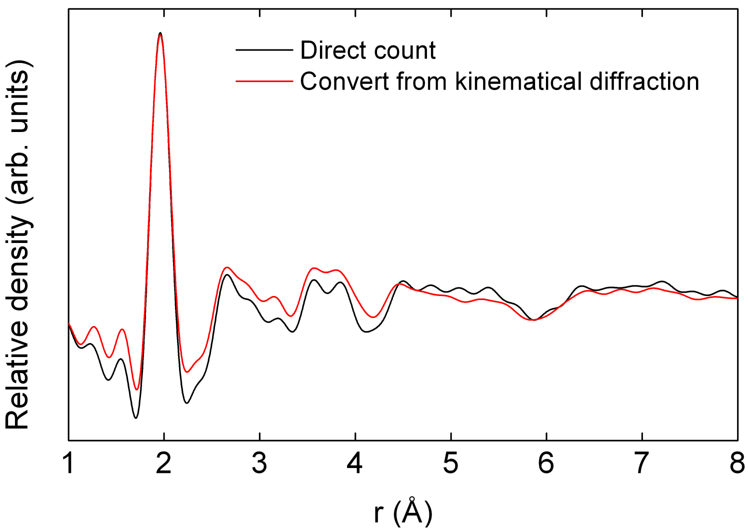

Figure 3.11: Difference between the directly counted PDF (black) and the PDF converted from the calculated PDF assuming kinematic electron diffraction (red) of the amorphous MgF_2 model with 6150 atoms.

difference. The point-spread function, due to spatial coherence of the LaB_6-source in the Zeiss EM912 and the crosstalk within the CCD camera, can also be taken into account by convolution of the diffraction profile with a Gaussian function e^{-Bs^2}. B is a fitting parameter which corresponds to the full width at half maximum of the point-spread function. The thermal vibration of the atoms was taken into account by multiplying the diffraction profile by a Gaussian damping function e^{-Us^2}. $U(T)$ is the 3-D isotropic Debye–Waller factor which is a function of the temperature T. The angular range between 0.1 and 3.3 Å^{-1} is selected for the Fourier transformation to be consistent with the experimental setting. After all these experimental considerations, the PDF comparison between the model and the experiments is reliable. The difference between the two discussed methods is illustrated in Fig. 3.11, yielding a low-frequency deviation between the two PDFs resulting from the two different methods.

4 Experiments and simulations

4.1 Experiments

Thin films of MgF_2, CaF_2, SrF_2, BaF_2 and their mixtures were generated from evaporation of MgF_2, CaF_2, SrF_2, BaF_2 (99.99 %, Aldrich, USA, dried at 473 K) by an effusion cell (MBE Komponenten GmbH, Germany) in high vacuum (1×10^{-8} mbar) and subsequent deposition of the gas phase directly onto a cooled (123 K) amorphous carbon substrate (2 nm thick, Quantifoil Micro Tools GmbH). The deposited specimen was transferred under vacuum and under cooling at the deposition temperature to the electron microscope (Zeiss EM912 Omega, 120 keV, Zeiss, Germany) using a dedicated low-temperature high-vacuum transfer holder (CHVT 3007, Gatan, USA) as shown in Fig. 4.1. The transfer holder is shown in Fig. 4.1a, the transfer process in Fig. 4.1b and the final view of the microscope with the holder inserted is presented in Fig. 4.1c. Using this holder the temperature can be increased up to 328 K. For the high-temperature range the specimen was transferred to a Gatan heating holder undergoing a short exposure to air. No structural changes of the material could be detected by this transfer.

Due to a high interface energy between the deposited materials and the amorphous carbon support, islands with average diameters of a few of tens nanometers initially form in the deposition process; therefore the film used in this work cannot be thinner. In order to gain homogeneous films, the films have to be deposited with thickness of (80 ± 20) nm for the MgF_2, (20 ± 5) nm for the CaF_2 and BaF_2, (40 ± 10) nm for SrF_2, and (35 ± 10) nm for the mixture of CaF_2 and BaF_2 and the mixtures of MgF_2 and BaF_2, confirmed by electron energy-loss spectroscopy (EELS).

For the electron diffraction experiments, energy-filtered diffraction was performed by using a 15 eV energy-selecting slit, centred at 0 eV energy loss. This slit is small enough to eliminate inelastic contributions because of the large band gap of the alkali-

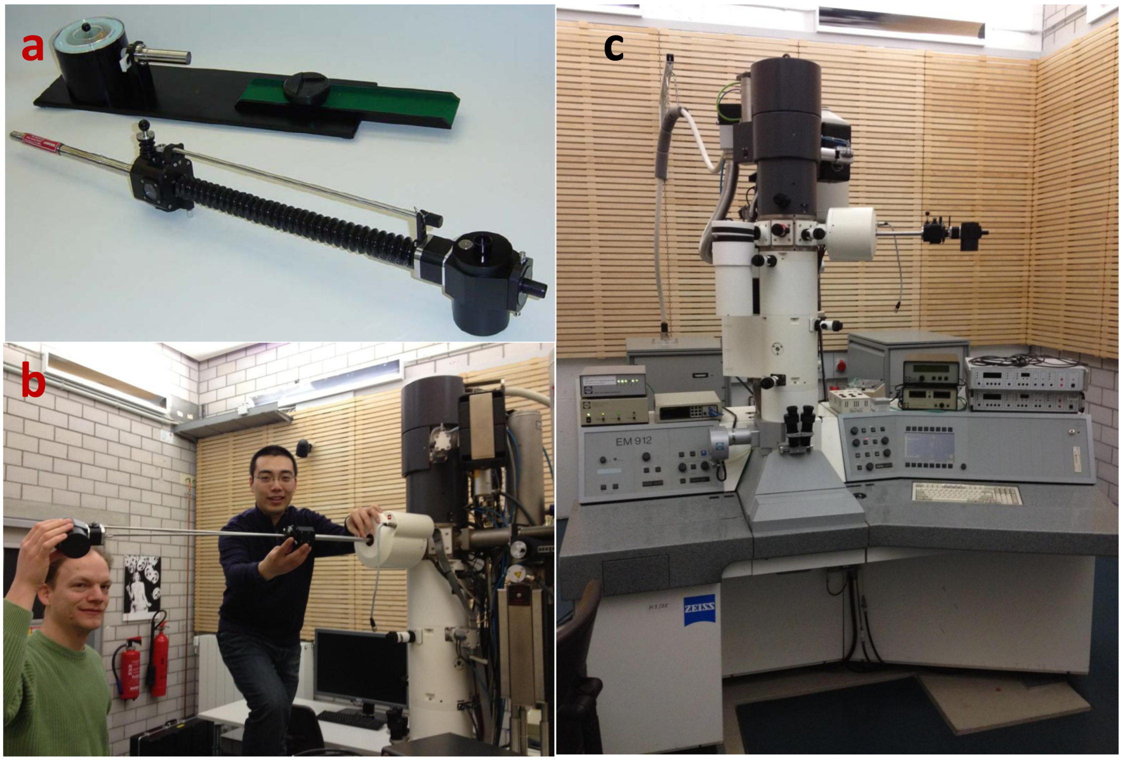

Figure 4.1: (a) Low-temperature high-vacuum transfer holder. (b) Inserting the transfer holder to microscope (c) Final view of the microscope with the holder inserted.

earth fluorides (around 10 eV). A selected area aperture of 1.2 μm diameter and an illumination area larger than 8 μm diameter were used. The illumination convergence angle was very small (0.08 mrad) owing to the design of Zeiss microscope (see section 3.2). For each measurement three diffraction patterns at different illumination beam tilts were acquired and spliced in order to access a large range of scattering-angles, up to 4.5 Å^{-1}. To splice the three patterns together the relative shift between each diffraction pattern was determined by calibration of the beam tilt shown in Fig. 4.2. A slow-scan CCD (MegaScan, Gatan, 2048×2048 pixels) was used with binning 2.

To determine the centre of the diffuse diffraction rings, a Digital Micrograph script written by Konstantin Borisenko in Oxford was used, shown in Fig. 4.3. 7 pixel coordinates have to be entered into the script (Fig. 4.3, highlighted by the red dashed ellipse) to calculate the concentric circle of the diffuse diffraction rings. The 7 inputs

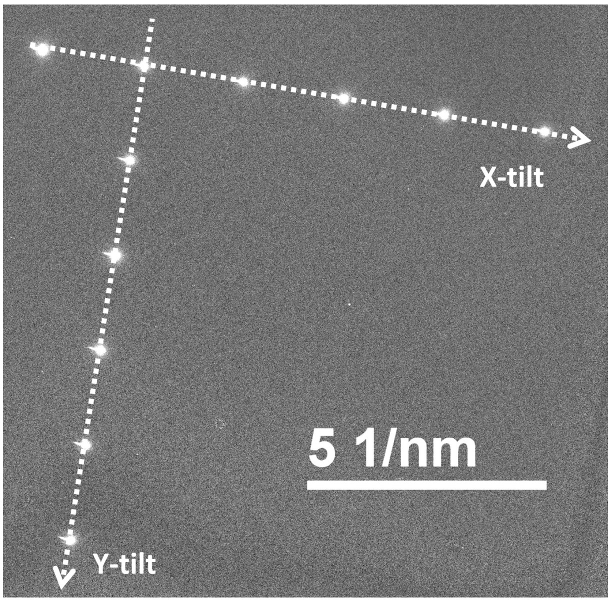

Figure 4.2: Calibration of the beam tilt. Bright spots are due to exposures of the central beam in diffraction mode with fixed beam tilt steps in two perpendicular directions (X-tilt and Y-tilt highlighted by the arrowed lines). No specimen was inserted.

are determined by manually selecting 7 different locations in the diffraction pattern located at the intensity maxima of the diffuse ring. The exact coordinates of maximum intensity are found by applying a line scan across the diffraction ring. The centre of the diffraction pattern is determined by fitting a circle to the 7 points (Fig. 4.4a) and then read out from the dialogue box. Figure 4.4a shows the calculated circle with the diffraction pattern in Fig. 4.3. Figure 4.4b shows a pattern recorded at larger beam tilt, the centre of which was determined by the centre of the non-tilted pattern plus the calibrated tilting value and then was input into the script dialogue box. The area which has to be avoid in diffraction patterns, such as the shadows of the energy slit and the beam stopper as well as the camera overexposure regions, can be eliminated by the mask control function in the script, an example of which is given by Fig. 4.4b. After the centre determination, Borisenko's script can then calculate the azimuthally averaged diffraction profile, which can be imported into Matlab or Origin for further analysis.

The initial structure (amorphous) of the deposited films is quite fragile even at moderate electron doses. Therefore, very low electron doses (less than 0.5 C/cm^2) were

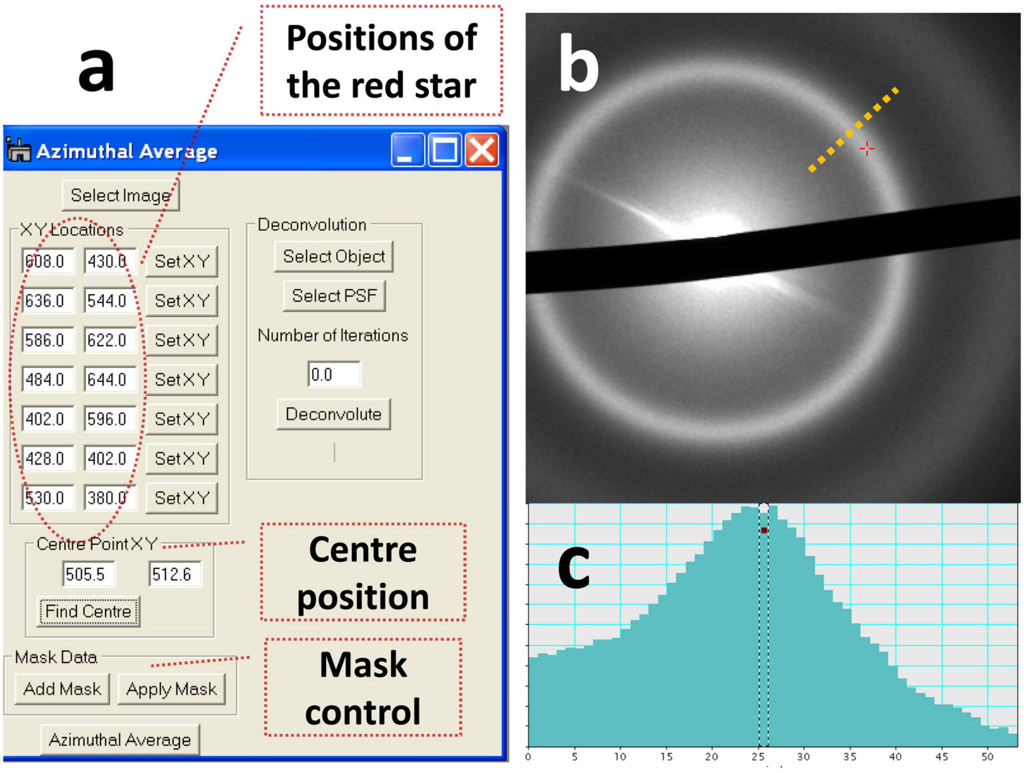

XY Locations

608.0	430.0
636.0	544.0
586.0	622.0
484.0	644.0
402.0	596.0
428.0	402.0
530.0	380.0

Number of Iterations 0.0

Centre Point XY 505.5 512.6

Figure 4.3: Centre determination by Borisenko's script. (a) The dialogue box of the script. (b) A diffraction pattern where the red cross is a handle to input pixel coordinates. (c) A line-scan across a diffused diffraction ring of the diffraction pattern (b, dashed orange line); the intensity maximum is highlighted by the dashed box.

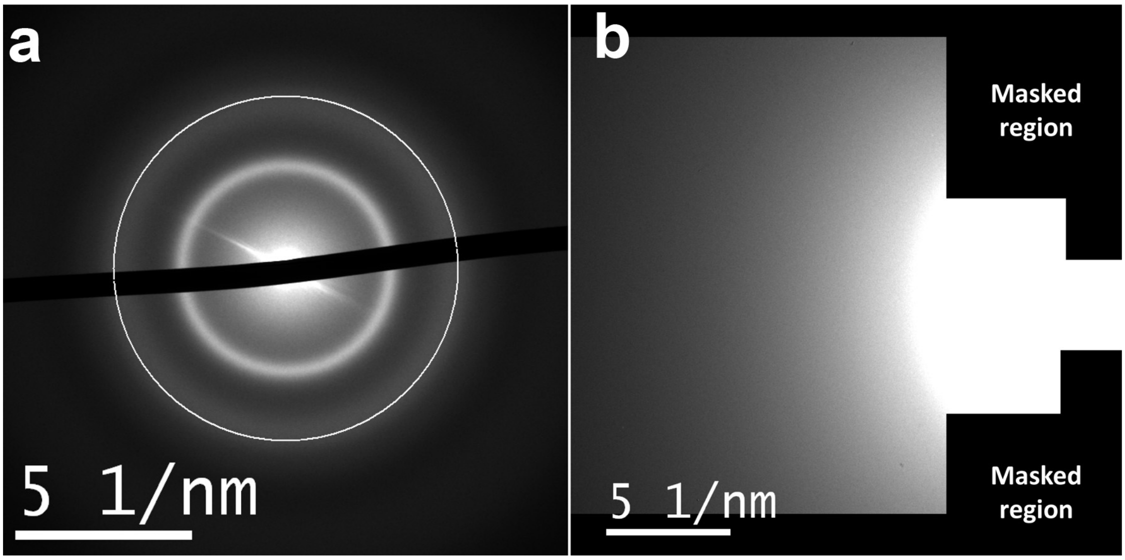

Figure 4.4: (a) A non-tilted diffraction pattern with the fitted concentric circle obtained by Borisenko's script. (b) A large-angle tilted diffraction with eliminating masks.

applied to avoid beam-induced structure alteration. This radiation sensitivity also limits the maximum recording angle up to 3.3 $Å^{-1}$ due to the drop of intensity with scattering angles, and did not allow high-resolution imaging (HREM) and EELS core-loss analysis for the MgF_2, CaF_2, SrF_2, and BaF_2 samples. The first non-tilted and the second tilted diffraction patterns were acquired with exposure time of 8 and 15 s, respectively. The third one was acquired with 15–200 s depending on the stability of material. These diffraction patterns were acquired immediately after selecting the area of interest and subsequent patterns were always taken from new, non-irradiated areas.

Fortunately, the mixtures are more stable than the pure binaries; thus the recording angle reached up to 4.0 $Å^{-1}$. Therefore EELS, EFTEM and HRTEM as well as EDX were also applied on the mixtures. The EELS spectra and STEM images were obtained on the SESAM (sub-eV sub-angstrom microscope based on the Zeiss Libra 200 KeV, field emission gun (FEG), equipped with the MANDOLINE filter and monochromator [75]). The EELS spectra were measured with parallel illumination (50 μrad) and a 3.1 mrad collection angle. The EFTEM measurements were performed on the Zeiss EM912 Ω with a 2 eV energy slit, 1 eV step size and 4.7 mrad collection angle.

4.2 Molecular dynamic simulations

The MD simulations were implemented in this project by a theory group, who applied the same method as for the study of the LT-ABD technique in the xenon system [76]. Due to the main interest in MgF_2 and the complexity of ternary systems (the mixtures), MD simulations were only performed on the structure transformation of the MgF_2 system.

To compare with the annealing experiment, MD simulations were performed via a deposition strategy [76], where atomic clusters were deposited onto a crystalline rutile-type substrate at different fixed temperatures. The deposition rate was much higher in the simulations than in the experiment. For this reason, considerable disorder was introduced during the simulated deposition, thus resembling the amorphous state in the experiment. Therefore the simulations describe the crystallization processes in the real experiment where the crystallization occurs from the bottom of the film close to the annealed substrate and develops upwards to the top surface of the film.

All simulations were performed using classical theories. A Coulomb-plus-Buckingham-type potential derived by Catti et al. [77] was used to describe the Mg–Mg, Mg–F, and F–F interactions. Newton's equations of motion were solved using the velocity Verlet algorithm. The linear MgF_2 monomer and the D_{2h} dimer were deposited on the (100) and the (110) surfaces of a rutile-type MgF_2 substrate with a fifty percent probability every 10^{-11} seconds. These were specifically chosen as a previous study on the vapor phase of MgF_2 indicated the presence of monomers and dimers in the vapor phase in our apparatus [29, 78]. The system was oriented such that the surface of the substrate lay in the x–y plane and the vertical direction was parallel to the z-axis. The exposed surface of the substrate had vertical z-coordinate set as zero. A rectangular simulation cell periodic in two dimensions was used. The cell dimensions were 48.895 and 49.686 Å in the x- and y-direction. The clusters were deposited from a height of 10 Å with an initial kinetic energy of 200 meV. Every MD step corresponded to a time step of 6 fs.

The substrate comprised 3600 atoms with the bottom two layers fixed in order to reproduce the effect of the bulk. A simple thermostat based on the velocity rescaling was used and applied to all atoms lying within a distance less than one third of the slab height from the bottom of the slab. Before starting the deposition, the slab was equilibrated for 2 ps at the temperature of deposition. The deposition of the monomer and dimer were carried out at temperatures of 50 K, 100 K, 300 K, 500 K, and 1000 K on the equilibrated slab.

5 Magnesium difluoride (MgF_2)

5.1 Structure of MgF_2

The structure evolution of MgF_2 from its low-temperature amorphous deposit to high-temperature polymorphs has been investigated [28]. By using an X-ray powder diffraction refinement technique, it was confirmed that the new MgF_2 polymorph found after the annealing process from the initially amorphous deposit was a metastable phase exhibiting the $CaCl_2$-type structure (space group Pnnm). The metastable phase finally transformed to the rutile-type phase after further annealing.

As the diffraction work [28] showed, XRD (Cu-$K\alpha$) has an intrinsic deficiency to characterize amorphous structures owing to the small scattering factor, especially for the in-situ measurements which need time resolution. The long wavelength of the X-rays results in a small sampling range in reciprocal space resulting in a loss of short-range information in real space, e.g. the short-range ordering in amorphous structure and distortions in crystalline structures. Therefore, electron diffraction was applied for understanding the amorphous phase and highly distorted crystalline phases.

In the previous work [28], the initially amorphous deposit was analysed, according to the analysis it was assumed that Mg-centred MgF_6 octahedra already exist in the amorphous phase. However, this interpretation from only experimental data remained speculative. In order to overcome this uncertainty structure modelling by theoretical simulation was necessary, particularly because previous theoretical calculations [79] and our own ab-initio structure relaxations prove that no energy barrier exists between the perfect (defect-free) bulk $CaCl_2$-type structure and the rutile-type structure. This puts the previously observed stability of the metastable phase into question.

Therefore, it will be shown that this discrepancy probably originates from the lack of properly describing disorder and distortion in ab-initio methods. In the present study in-situ electron diffraction measurements combined with MD simulations is used to analyze the PDFs of the different phases in the transformation processes. Electron scattering data is analyzed with a modified procedure which improves the reliability of the experimental PDFs. An excellent match between the experimental data and the MD simulations is obtained without any further numerical refinement in the simulated data. This is strong evidence for the reliability of the PDF analysis. From the elaborate analysis of the structural disorder and distortions, the existence of a $CaCl_2$-type arrangement of octahedra in the initially amorphous phase acting as nuclei in the following crystallization is confirmed. Furthermore, intergranular regions with disordered structure in the crystalline phase are found. A conclusion of that the $CaCl_2$-type crystals are most likely stabilized by strong strains generated by these regions is given. Furthermore, it is found that the experimentally observed $CaCl_2$-type metastable phase has a short-range structural distortion toward the rutile-type. Finally, by considering the above findings, the structure evolution is summarized within the energy landscape concept.

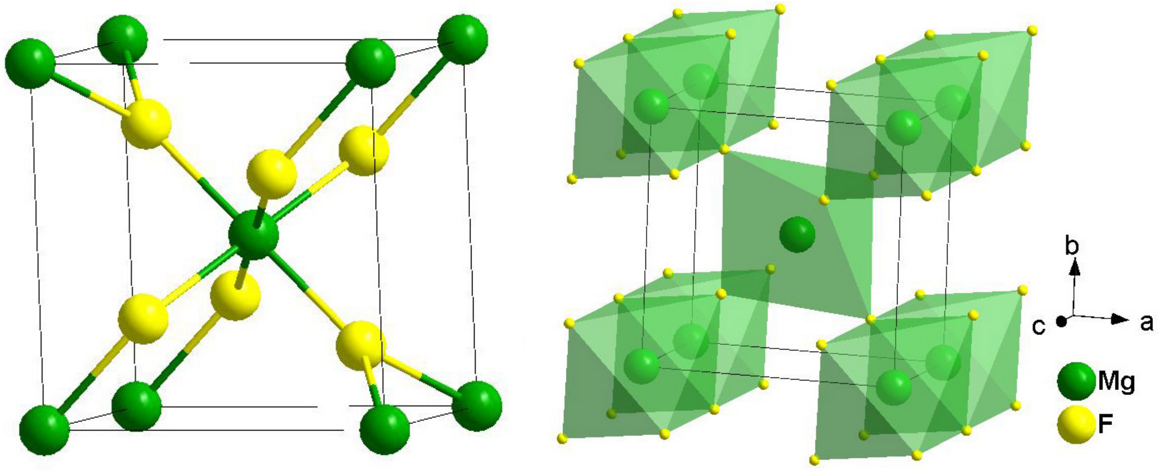

Figure 5.1: The unit cell of rutile-type MgF_2. The green polyhedra indicate the central Mg with six-fold coordinated F octahedra.

Figure 5.1 shows one unit cell of the rutile-type MgF_2 which is orthorhombic. The Mg^{2+} ions are coordinated by 6 F^- ions forming MgF_6 octahedra, and the F^- ions are coordinated by 3 in-plane Mg^{2+} ions. Figure 5.2 shows an overview of the crystalline

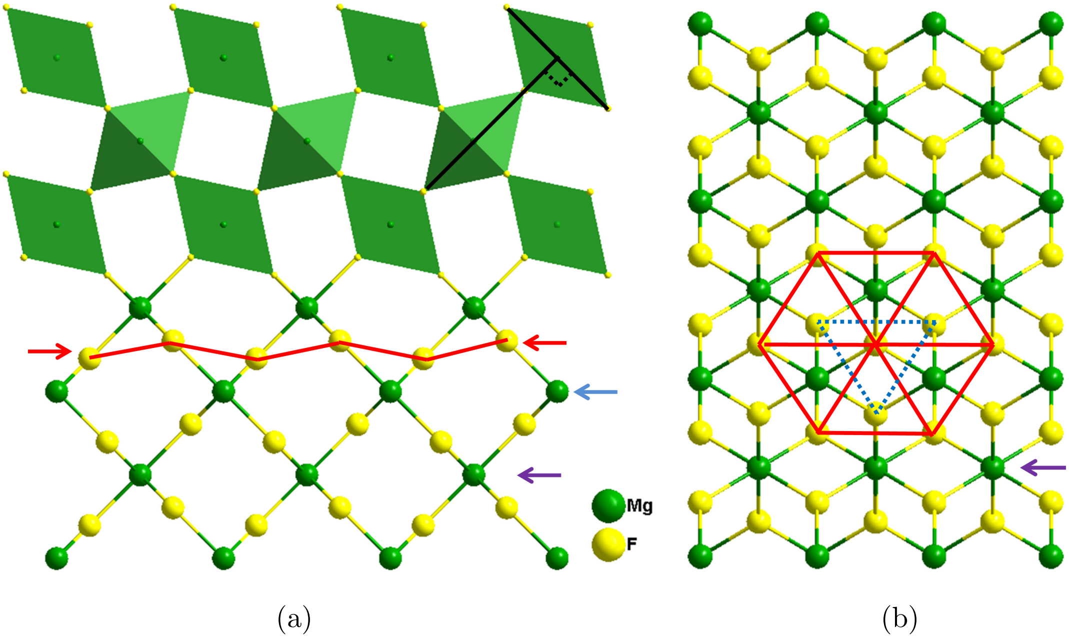

Figure 5.2: Crystalline structure of rutile-type MgF_2 viewed along the (a) [001] and (b) [100] directions.

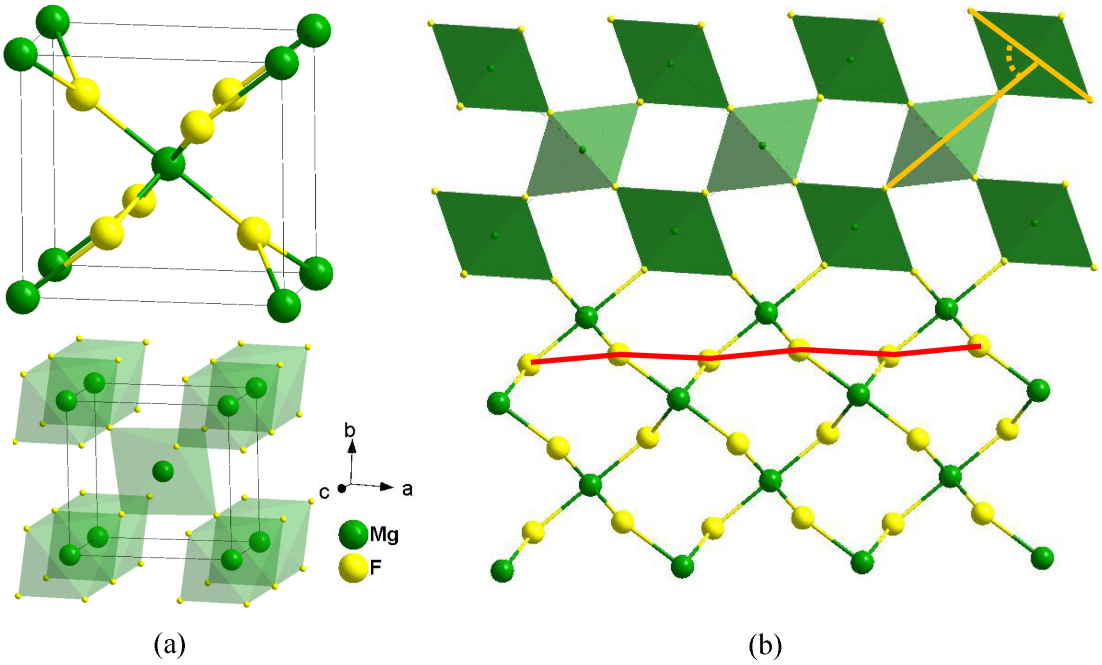

Figure 5.3: Crystalline structure of $CaCl_2$-type MgF_2, (a): unit cell. (b): view along the [001] direction.

rutile-type MgF_2 from the view direction of [001] (a) and [100] (b). The octahedra are perpendicular to each other in the a-b plane (Fig. 5.2a, black sticks). The red solid lines (Fig. 5.2) highlight the hexagonally packaged F^- anions, which form zigzag planes as indicated. The blue-dashed lines in Fig. 5.2b indicate the hexagonal stacking geometry of the F^- anions in the next plane. The dark-blue arrows indicate the array of Mg^{2+} cations stacked above the F^- plane highlighted by the red-solid sticks; the purple arrows indicate the array of the Mg^{2+} cations attached below the highlighted F^- plane.

Figure 5.3a shows the unit cell of the $CaCl_2$-type crystalline MgF_2. All coordination geometries are the same as those of the rutile-type structure, but because of a small twist of the octahedra in the [001] plane illustrated by the orange sticks (Fig. 5.3b), the octahedra are not perpendicular as in Fig. 5.2a. Consequently the planes formed by the hexagonally packaged F^- ions become more flat (indicated by the red solid line in Fig. 5.3b) than in the rutile-type structure. This small twist of the octahedra makes the structure lose symmetry elements and transforms from the space group $P4_2/MNM$ (136, rutile-type) to the space group PNNM (58, $CaCl_2$-type).

5.2 PDF analysis

In this section the experimental PDF is combined with MD simulation data to evaluate the structure evolution of MgF_2 from the amorphous deposit to the polycrystalline polymorphs.

5.2.1 In-situ electron diffraction

Temperature dependent 2D- and azimuthally averaged 1D-diffraction patterns of the structure evolution of the MgF_2 deposit are shown in Figs. 5.4 and 5.5. The broad peaks in the experimental diffraction pattern (Fig. 5.4a) and the extracted structure factor (Fig. 5.5a, green line, bottom) show that the initial phase of the deposit at 123 K is amorphous. After annealing, the amorphous specimen crystallizes at around 458 K and forms a polycrystalline phase, shown by the diffraction patterns recorded at 463 K (Fig. 5.4b) and the corresponding structure factor (Fig. 5.5a, blue line, middle). The polycrystal has grain sizes of 5–8 nm determined by TEM dark-field

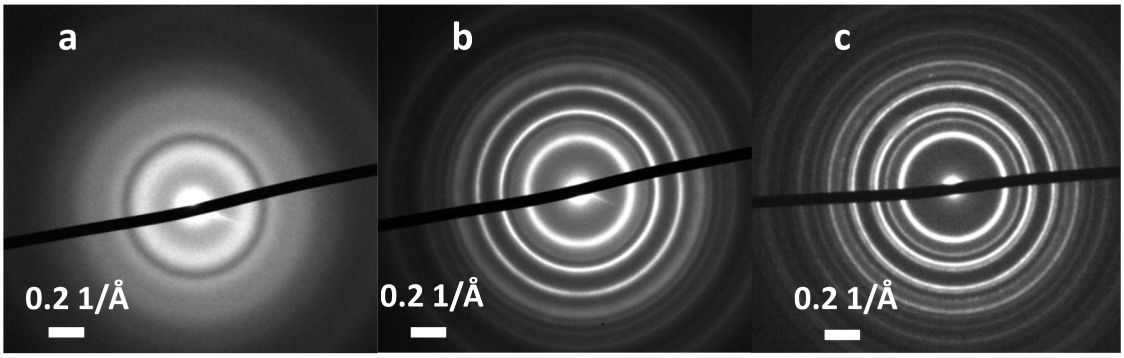

Figure 5.4: Experimentally measured electron diffraction patterns recorded at (a) 123 K, (b) 463 K, and (c) 733 K of the MgF_2 film.

imaging (not shown here). The structure of this polycrystalline phase is $CaCl_2$-type [28]. The specimen undergoes a second crystallization at around 653 K. The third phase formed after this crystallization step exhibits a polycrystalline rutile-type structure shown by the diffraction pattern recorded at 733 K (Fig. 5.4c) and the corresponding structure factor (Fig. 5.5a, red line, top). The grain sizes are between 10 and 20 nm measured by TEM dark-field imaging (not shown here).

Figure 5.5b depicts PDFs calculated from the experimental structure factors shown in Fig. 5.5a. Because of multiple-scattering, peak heights of the experimental PDFs cannot be accurately analyzed. Thus, the most pronounced peak at 1.99 Å was used to align all PDF curves in this work to the same height (peak maximum) to obtain a reasonable relative height comparison.

All three experimentally measured PDFs have a well-defined peak at around 1.99 Å which corresponds to the radius of the first coordination shell of Mg–F. It reveals the closest atomic distance between Mg and F atoms in both, the amorphous and the polycrystalline phase. The PDF of the amorphous phase (bottom, green line in Fig. 5.5b) shows a remarkable weakening of peaks at distances larger than 2.4 Å. This weakening explicitly demonstrates the lack of long-range order characteristic of amorphous phases. However, the damped and broad peaks of this PDF at 2.71, 2.97, 3.68 and 4.63 Å are still present and the positions are close to the peaks of the $CaCl_2$-type phase (middle, blue line in Fig. 2b) and rutile-type phase (top, red line in Fig. 5.5b). This implies that the structure of the amorphous phase already contains a certain degree of short-range order

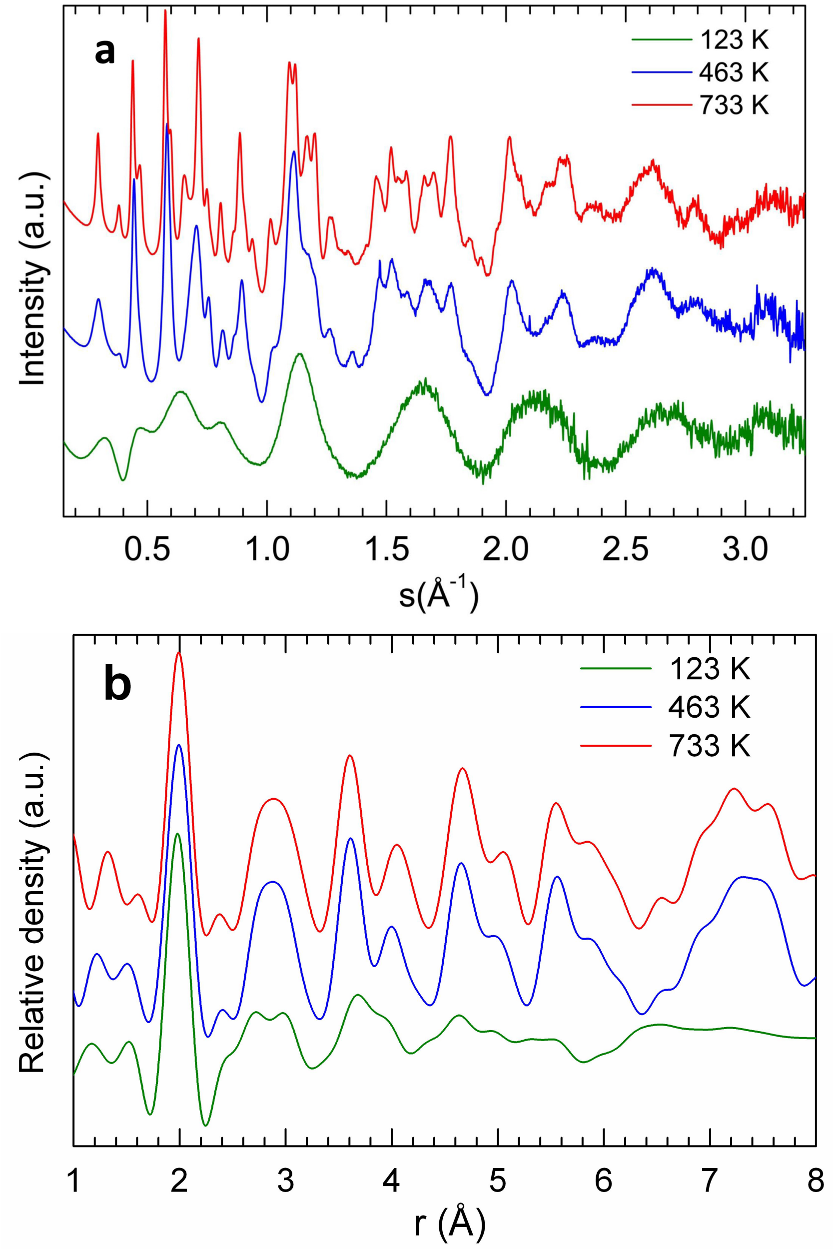

Figure 5.5: (a) Experimental structure factors and (b) corresponding PDFs of the amorphous phase at 123 K (green, bottom), the $CaCl_2$-type phase at 463 K (blue, middle), and the rutile-type phase at 733 K (red, top).

similar to the one present in the (meta)stable crystalline phases. In contrast, the more pronounced and sharp peaks in the PDFs of the two crystalline phases at large r values demonstrate the long-range order established after crystallization. In the following, It will be shown that, with the help of the MD simulations, a deeper understanding of the experimental data is achieved.

5.2.2 MD simulations

Figure 5.6 shows the MD simulation results. Figure 5.6a shows the evaporation process where neutral and ionic (MgF_2)-clusters in the gas phase are obtained. Figure 5.6b shows an amorphous MgF_2 network that has formed during the deposition simulation on the MgF_2 rutile (100) substrate at 50 K. Figure 5.6c shows the mostly crystalline MgF_2 network (distorted rutile-type structure) at the end of the deposition simulation on the MgF_2 rutile (100) substrate at 500 K. It is observed that the crystalline network exhibits the highest degree of order in the bottom region near the substrate, while in the top region far away from the substrate a disordered amorphous-like structure is present. This is due to the fact that the first layers of atoms have had enough time at 500 K to transform from the initially amorphous structure formed right after deposition to an ordered atom arrangement.

Structure factors and corresponding PDFs are calculated from the above MD simulation results and also from the perfect crystalline structure of both $CaCl_2$-type and rutile-type structures whose parameters are taken from [28]. They are then compared to the experimental structure factors and PDFs.

5.2.3 Comparison between experiment and simulation

Figure 5.7a shows the experimental structure factors of the specimen measured at 733 K (Fig. 5.7a, black solid line) and of the MD simulation at 500 K using all atoms of the MD cell (Fig. 5.7a, red solid line) and of the perfect model of rutile-type structure (Fig. 5.7a, blue dotted line). Peak positions of the experimental structure factor show good agreement with those of the perfect model of the rutile-type structure. This agreement confirms that the structure of the specimen annealed at 733 K is close to rutile-type. However, the peaks of the experimental structure factor are strongly damped compared

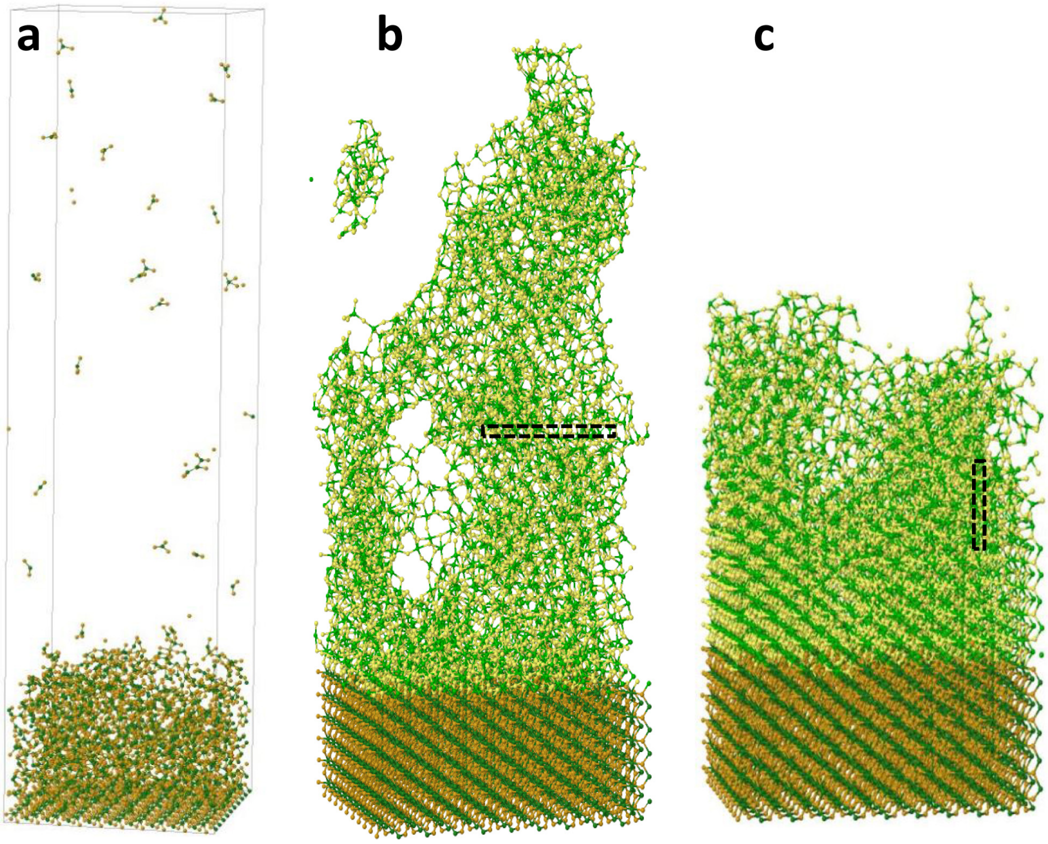

Figure 5.6: (a) Evaporation on crystalline rutile MgF_2 substrate to obtain the cluster structure in the glassy phase. (b) Structure obtained by MD simulations at 50 K (amorphous) and (c) 500 K (crystalline). The regions in the black dashed rectangular boxes in (b) and in (c) are shown enlarged in Fig. 5.8 and Fig. 5.10.

to the perfect rutile-type model. On the other hand, the experimental structure factor shows excellent agreement, both in peak heights and widths, with the structure factor calculated from the 500 K MD model. Because the 500 K MD simulation contains highly ordered as well as disordered regions, it is concluded that the specimen annealed at 733 K also contains disordered regions. According to that the MD simulation mimics the crystallization process along the bottom-up direction in the MD supercells, these regions most likely correspond to grain-boundary regions and occupy a large volume fraction in the nanocrystalline structure of the specimen annealed at 733 K. A disordered grain boundary (from MD results) is shown in the top part of the supercell in Fig. 5.6c and enlarged in figure 5.8a, where the MgF_6 octahedra (highlighted by green polyhedra, above the two black arrows) are strongly distorted and in disordered arrangement.

From the 500 K MD simulation result one can calculate element-specific partial PDFs, and these are shown in Fig. 5.7b: F–F (blue), Mg–F (pink), and Mg–Mg (green). These partial PDFs allow us to better understand the presence of peaks of the total PDFs. The first pronounced peak at 1.99 Å is due to the Mg–F first coordination shell. The second pronounced peak at 2.83 Å is mainly attributed to the first F–F coordination shell. Therefore, the F–Mg–F triangle is defined by the first and second peaks in the PDF obtained from the experimental data, which reveals the approximately average bonding angle of F–Mg–F of 90°, and hence prove the existence of the Mg-centered MgF_6 octahedra in the annealed specimen. The broadening of the second peak toward 3.10 Å and the third pronounced peak at 3.60 Å correlate with two Mg–Mg peaks which come from two different geometric configurations of the adjacent Mg–Mg atom pairs in the rutile-type structure. The first configuration is due to two adjacent MgF_6 octahedra sharing one edge, i.e. two nearby Mg atoms share two F atoms, to form the first Mg–Mg coordination shell (Fig. 5.8b, red dashed line). The second configuration is due to two adjacent MgF_6 octahedra sharing only one corner, namely one F atom, to form the second Mg–Mg coordination shell (Fig. 5.8b, blue dashed line).

The experimental structure factor of the specimen deposited and measured at 123 K (Fig. 5.9a, black) shows a very good agreement with the structure factor of the 50 K MD simulation result (Fig. 5.9a, red line). The broad peaks in both structure factors confirm the amorphous structure. The element-specific partial structure factors, F–F (Fig. 5.9a, blue line), Mg–F (Fig. 5.9a, pink line), and Mg–Mg (Fig. 5.9a, green line)

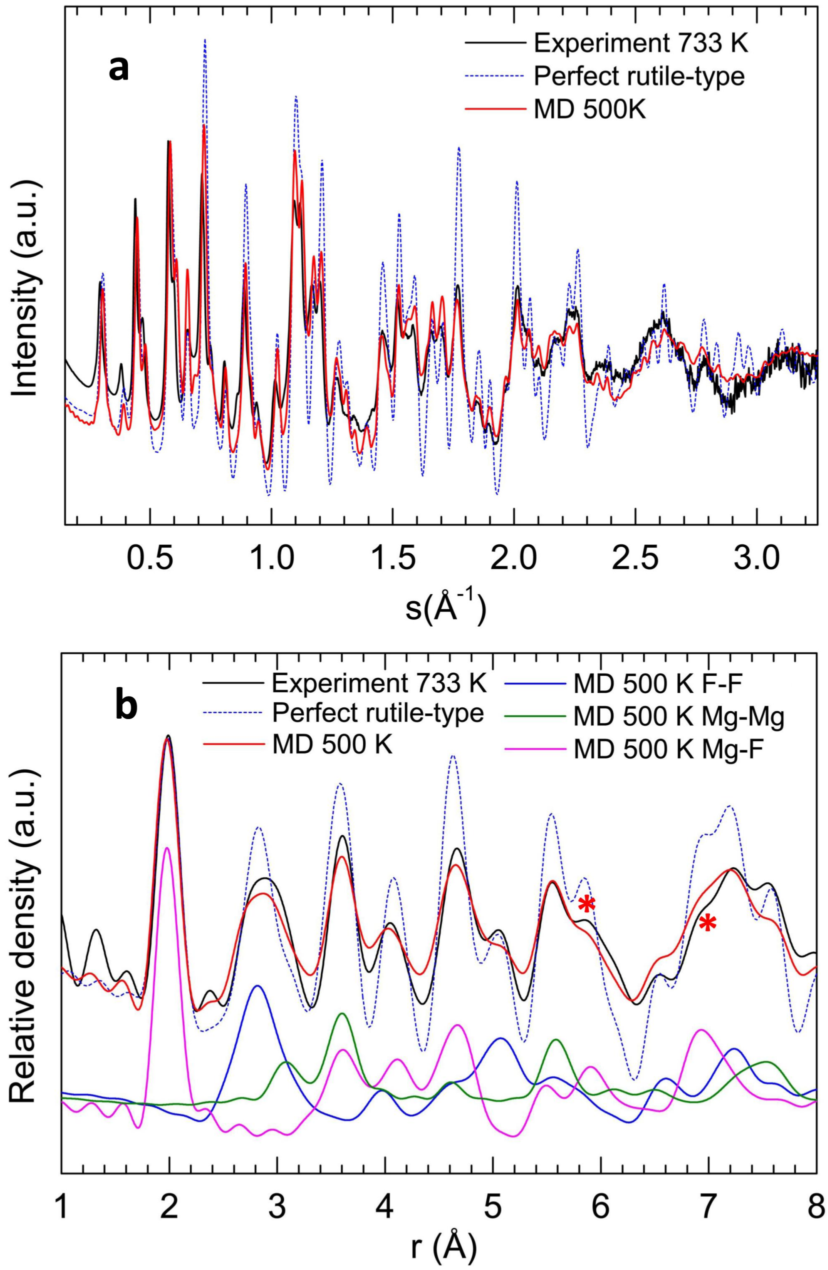

Figure 5.7: (a) Structure factors obtained from experiment at 733 K (black, solid) and MD simulation at 500 K (red, solid), as well as the perfect rutile-type structure (blue, dotted). (b) PDFs obtained from the experiment at 733 K (black, solid), MD simulation at 500 K (red, solid) and the perfect rutile-type structure (blue, dotted). Also shown (bottom three curves) are the element-specific partial PDFs, F–F (blue), Mg–F (pink), and Mg–Mg (green), calculated from the atomic structure of the MD simulation at 500 K.

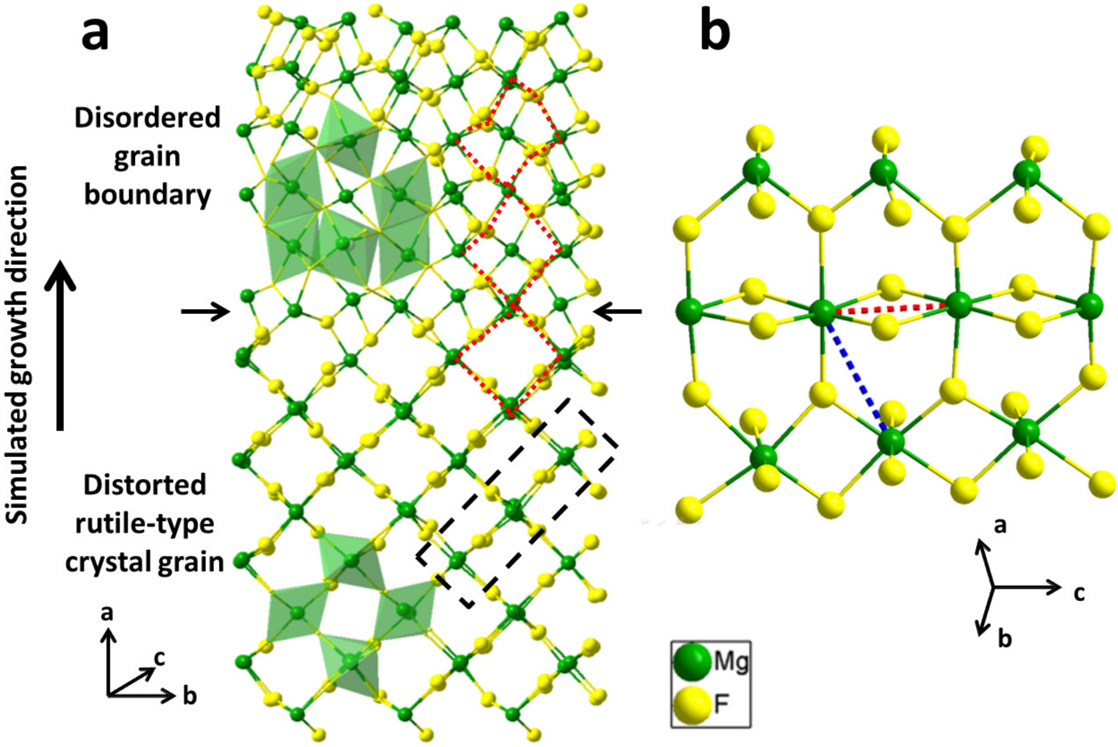

Figure 5.8: (a) Enlarged section of the MD 500 K simulated network taken from Fig. 5.6c (black dashed rectangular box). The black arrows indicate the boundary between the rutile-type structure and the strongly disordered region. The red dashed lines highlight the increasing disorder far from the boundary. (b) Enlarged local structure from the black dashed rectangular box in (a).

show that at large angles the total structure factor is dominated by the Mg–F partial structure factor. The F–F and Mg–Mg partial structure factors are strongly damped in the large-angle region.

The corresponding PDFs and partial PDFs are shown in Fig. 5.9b. Again, experimental and simulated total PDFs show good agreement. From the partial PDFs it is seen that the first pronounced peak at 1.99 Å corresponds to the Mg–F first coordination shell, similar as for the rutile-type (Fig. 5.7b). The peak around 2.72 Å in the experimental PDF correlates to the short-range ordered structure of the F–F octahedra. Compared to the crystalline state (Fig. 5.7) the peak at 2.72 Å is strongly damped in the experimentally obtained PDF of the amorphous material. This implies

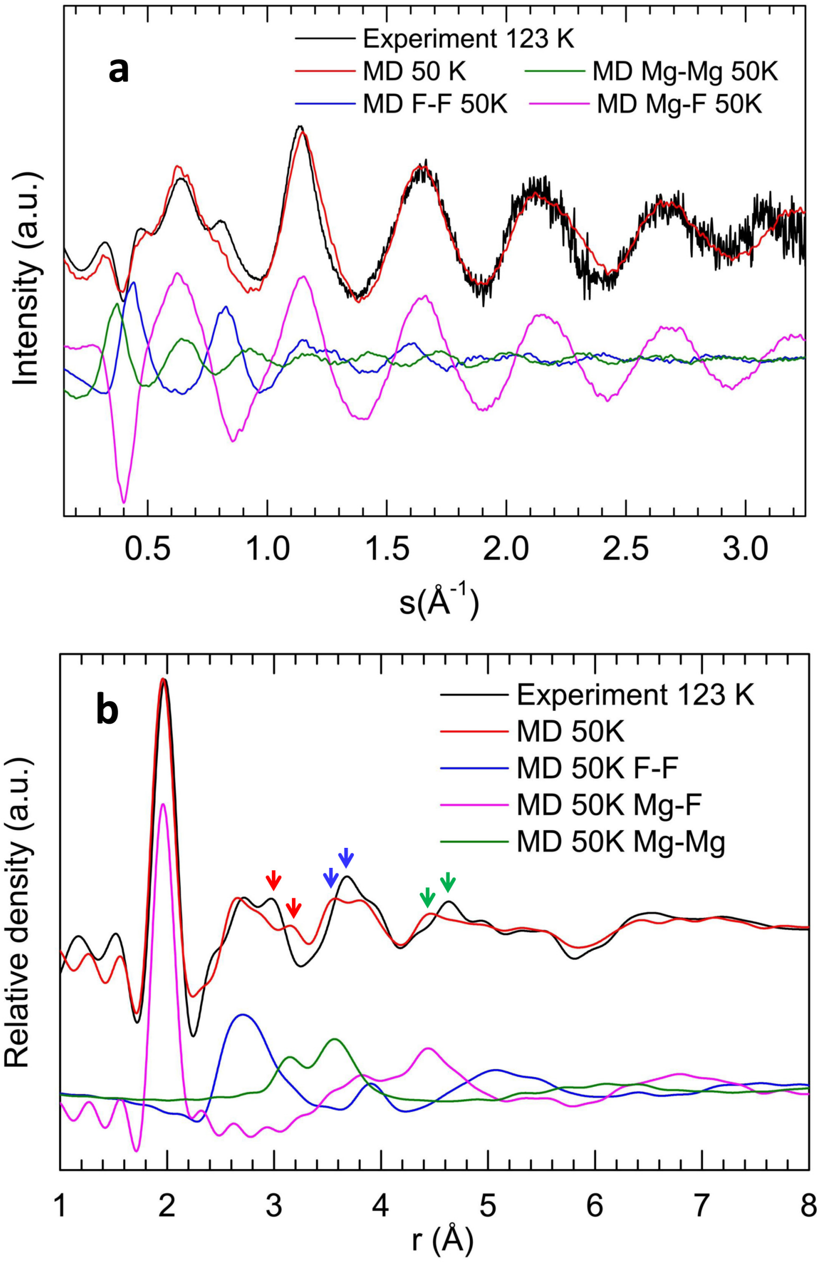

Figure 5.9: (a) Structure factors obtained from the experiment at 123 K (black) and MD simulation at 50 K (red), as well as the element-specific partial structure factors, F–F (blue), Mg–F (pink), and Mg–Mg (green), calculated from the MD model annealed at 50 K. (b) PDFs obtained from the experiment at 123 K (black), MD simulation at 500 K (red) and the element-specified partial PDFs (bottom three curves), F–F (blue), Mg–F (pink), and Mg–Mg (green), calculated from the atomic structure of the MD simulation at 50 K.

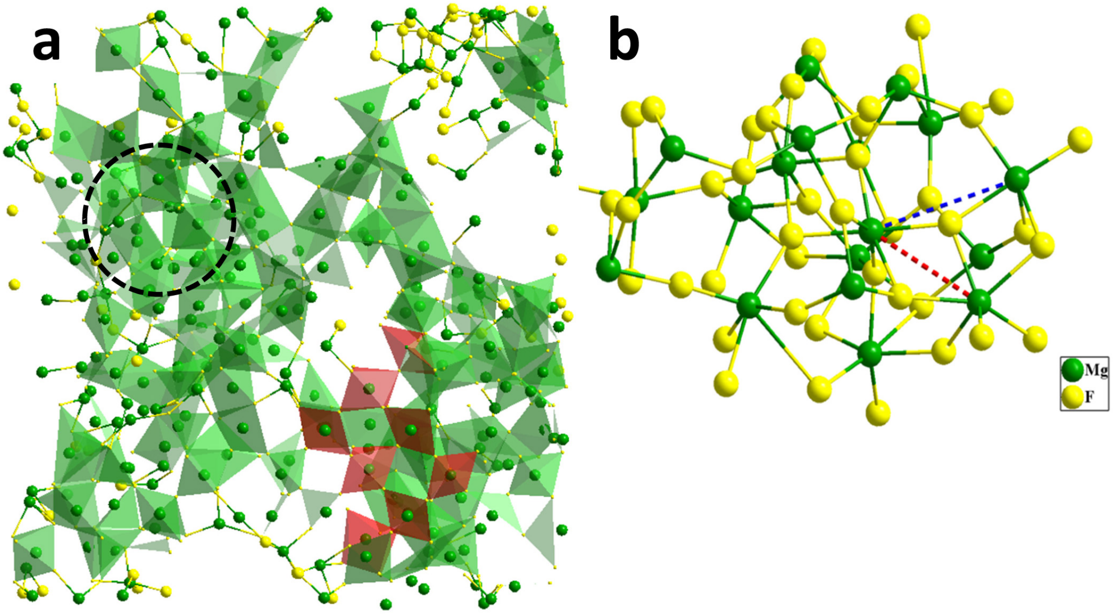

Figure 5.10: (a) Enlarged piece of the MD 50 K simulated network taken from Fig. 5.6b (black dashed rectangular box). The red-colored polyhedra indicate a set of ordered octahedra as a nucleus. (b) Enlarged local structure from (a) (black dashed circle).

that the F–F octahedra are significantly distorted and some of the Mg atoms may even have only 4 or 5 F neighbours. Figure 5.10a, enlarged from Fig. 5.6b (black dashed rectangular box), depicts the disordered arrangement of distorted octahedra (green polyhedra).

Despite the overall good agreement between experimental and MD PDF data, there are several small differences marked by arrows in Fig. 5.9b. The red arrow on the 50 K MD PDF points out the first Mg–Mg peak which occurs when two adjacent Mg atoms share two F atoms (Fig. 5.10b, red dashed line), i.e. the first Mg–Mg coordination shell. The blue arrow on the 50 K MD PDF indicates the second Mg–Mg peak which corresponds to two adjacent Mg atoms sharing only one F atom (Fig. 5.10b, blue dashed line), i.e. the second Mg–Mg coordination shell. As the contributions of the Mg–F peaks in the region between 2.9 and 3.8 Å are not expected to be very pronounced, the positions of the two arrow-marked peaks should mainly be dominated by the Mg–Mg contribution. Therefore, it is assumed that the red arrow at 2.97 Å on the experimental

PDF is related to the first Mg–Mg coordination shell, and the blue one at 3.68 Å to the second Mg–Mg coordination shell, respectively. The mismatches marked by the red and blue arrows in Fig. 5.9b can be attributed to different Mg–Mg distributions of the experimental and simulated structure. The first Mg–Mg coordination shell in the experiment has a smaller radius than the one in the MD model. The second Mg–Mg coordination shell in the experiment has a larger radius than in the MD simulation result. The radial difference between the first Mg–Mg coordination shell and the second Mg–Mg coordination shell in the experiment is larger than that in the MD model. It can be explained that this difference might be connected to the mismatch marked by the green arrow in Fig. 5.9b which is contributed by the Mg–F pairs.

Figure 5.11a shows the comparison between the structure factor of the specimen annealed at 463 K (black) and the perfect rutile-type crystalline structure (red). Fig. 5.11b shows the comparison between the structure factor of the specimen annealed at 463 K (black) and the perfect $CaCl_2$-type crystalline structure (red). In Fig. 5.11b, the structure factor of the annealed specimen shows good agreement with that of the perfect $CaCl_2$-type structure in the low-angle range (left side of the blue dashed line), which contains information about the long-range periodicity of the structure. However, from the peak position point of view, the structure factors between experiment and perfect $CaCl_2$-type do not match in the high-angle range (right side of the blue dashed line), which contains information about the short-range periodicity. On the other hand, in Fig. 5.11a, peak positions of the structure factor of the annealed specimen agree with peak positions of the structure factor of the perfect rutile-type structure in the high-angle range. This angular-dependent agreement implies that the structure observed in the experimental specimen annealed at 463 K contains long-range periodicity similar to the one in the metastable $CaCl_2$-type structure together with a short-range distortion towards the thermodynamically stable rutile-type structure.

Figure 5.11c shows the PDF of the specimen annealed at 463 K (black) showing strong damping compared to that of the perfect $CaCl_2$-type structure (red). The damping reveals that the annealed specimen is strongly distorted from the perfect $CaCl_2$-type structure. The positions marked by red stars show even the same feature as the PDF of the specimens annealed at 733 K (Fig. 5.11b, red stars), which has rutile-type structure.

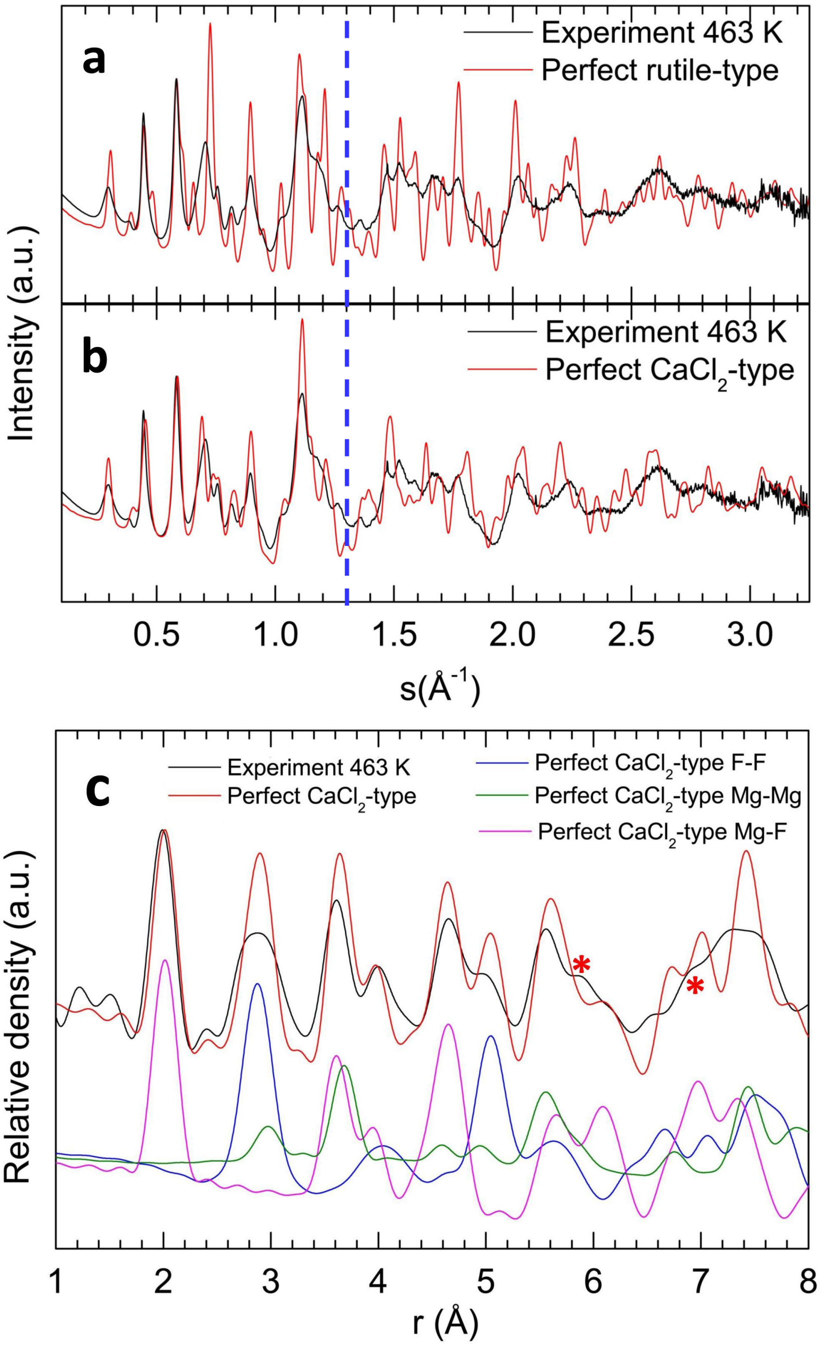

Figure 5.11: (a) Structure factors of the experiment measured at 463 K (black) and perfect rutile-type structure (red); (b) experimental structure factors measured at 463 K (black) and perfect CaCl$_2$-type structure (red); (c) experimental PDFs measured at 463 K (black) and perfect CaCl$_2$-type structure (red line) as well as the element-specific partial PDFs (bottom three curves), F–F (blue), Mg–F (pink), and Mg–Mg (green), calculated from the perfect CaCl$_2$-type structure.

Therefore it can be assumed that the observed structure in the specimen annealed at 463 K contains features of both, the $CaCl_2$-type and the rutile-type structure.

The $CaCl_2$-type structure also contains MgF_6 octahedra. These octahedra have an arrangement similar to the slightly tilted ones present in the ideal rutile structure. The partial PDFs, F–F (Fig. 5.11c, blue line), Mg–F (Fig. 5.11c, pink line), and Mg–Mg (Fig. 5.11c, green line), obtained from the perfect $CaCl_2$-type structure confirm these geometric configurations. The Mg–Mg partial PDF shows the first Mg–Mg peak at 2.97 Å and the second Mg–Mg peak at 3.68 Å. The two Mg–Mg peaks have exactly the same positions as those in the experiment at 123 K (Fig. 5.9b, red and blue arrows). However, the corresponding peaks in the rutile-type structure are at 3.08 and 3.60 Å, which differ from the Mg–Mg first and second peaks in the experiment at 123 K and the differences are outside of the error bar. This reveals that the specimen deposited at 123 K has locally the same Mg–Mg distribution as the $CaCl_2$-type structure.

5.3 Discussion

The phase transformation from the amorphous phase through the polycrystalline $CaCl_2$-type phase to the rutile-type phase is observed in the experiment and this phase transformation is not reversible when the temperature is reduced. The $CaCl_2$-type structure is attributed to a metastable phase, while the rutile-type phase is thermodynamically stable.

The very good match between the PDFs obtained from the experimental data and from the MD simulation, both in the crystalline rutile-type phase as well as the amorphous phase, shows that our PDF data are reliable. It is also a confirmation for the applicability of the applied pair potential to the amorphous and crystalline phases.

The specimen deposited at 123 K contains the same Mg–Mg geometric local structure as the metastable $CaCl_2$-type phase. This indicates that already during the atom deposition process the deposited clusters rearrange their positions locally to reduce the free energy, i.e. the as-deposited state is not the ideally random distribution of the gas-phase clusters. Obviously the deposit reaches a local minimum in the energy landscape whose free energy is in between the ideally amorphous phase and the $CaCl_2$-type phase. Differences between the simulated and experimental PDFs are most likely due to the difference in temperature (50 K versus 123 K) and the difference in time (nanoseconds versus hours). In the MD simulation, gas-phase clusters are deposited in random locations on the substrate, and because of the low temperature not enough local rearrangements can take place inside this amorphous phase during the limited simulation time.

The local $CaCl_2$-type magnesium atom arrangement in the experimental amorphous specimen plays the role of crystallization nuclei to guide the crystallization process toward the $CaCl_2$-type phase when the specimen is annealed at 458 K. The direct structure evolution to the crystalline rutile-type structure, which constitutes the global minimum of the (free) energy landscape in the MgF_2 system, is thus suppressed. The high density of the $CaCl_2$-type nuclei leads to small grain sizes (5–10 nm) even at an annealing temperature of 463 K. At this temperature, the structure of the intergranular regions is still essentially amorphous. We note that previous theoretical calculations [79] and our ab-initio structure relaxation show that the perfect (defect-free) bulk $CaCl_2$-type structure is not separated by an energy barrier from the rutile-type structure. Therefore, crystallization from the amorphous phase should directly lead to the energetically stable rutile-type phase. However, the experimental data suggest the presence of a barrier between the $CaCl_2$-type and rutile-type phases. Haines et al. [80] reported an experimental observation of a second-order phase transformation of MgF_2 from the rutile-type structure to the $CaCl_2$-type structure at high ambient pressure (9.1 GPa). This indicates that strain can stabilize the $CaCl_2$-type structure. It is suggested that in the samples this structure is stabilized by the presence of intergranular strain between the nanocrystals caused by the disordered intergranular regions. This strain generates a barrier on the energy landscape which stabilizes the $CaCl_2$-type structure. To confirm this statement, an abinitio calculation was also performed, where a $2\times2\times2$ supercell of the $CaCl_2$-type modification (structure data taken from experiment [28]) was relaxed on ab-initio level while keeping the cell parameters of the supercell fixed. This boundary condition mimics the application of an external strain to a nanoscale crystal. Even though the Mg- and F-atoms were free to move within the supercell, no distortion towards a rutile-like atom arrangement occurred. In contrast, if the cell parameters were allowed to vary during the relaxation, the structure directly transforms to the rutile-type modification. Thus, these calculations strongly support the hypothesis that the $CaCl_2$-type nanocrystals are stabilized by intergranular strains.

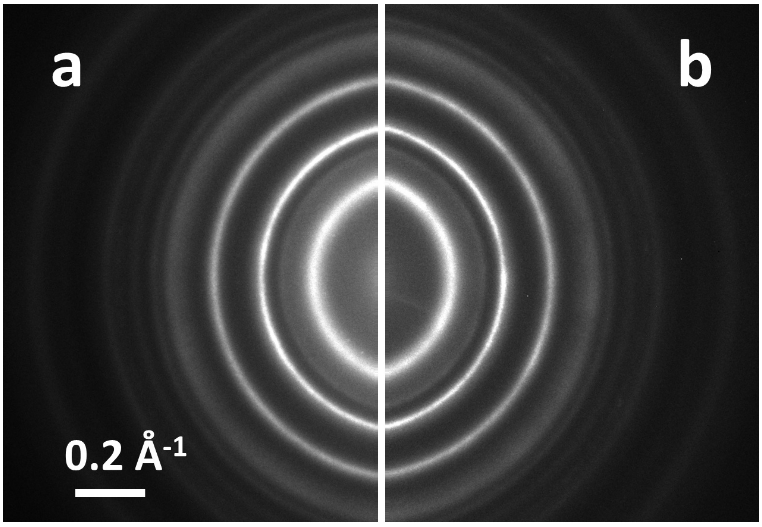

Figure 5.12: Diffraction patterns measured at 463 K (a) immediately following the crystallization and (b) after 18 hours.

Because of the metastability of the $CaCl_2$-type phase, the structure factor and PDF measured at 463 K show a mixed structural configuration between long-range $CaCl_2$-type periodicity and short-range distortion towards the rutile-type structure. The first crystallization to the $CaCl_2$-type structure happened very fast (within a few seconds) when the temperature reaches about 458 K. The specimen was kept at 463 K for around 18 h and diffraction patterns were acquired at different times to monitor whether the structure changed during heating. As shown in Fig. 5.12, no discernible structure change was found from the time-resolved diffraction patterns. Moreover, to fit perfect rutile-type and perfect $CaCl_2$-type structure factors to the structure factor measured at 463 K with different composition ratios was tried, but no better match could be obtained both in the low-angle and the high-angle regions. Therefore, it is believed that the phase observed at 463 K is not simply a mixture of $CaCl_2$-type and rutile-type phases, but a single phase with a structure possessing both the $CaCl_2$-type in long-range order and the rutile-type in short-range order.

Upon annealing at temperatures above 653 K, the crystal size grows, the volume of the intergranular regions decreases, and thus the intragranular strain is reduced. The long-range order of the $CaCl_2$-type crystalline grains finally transforms to the rutile type.

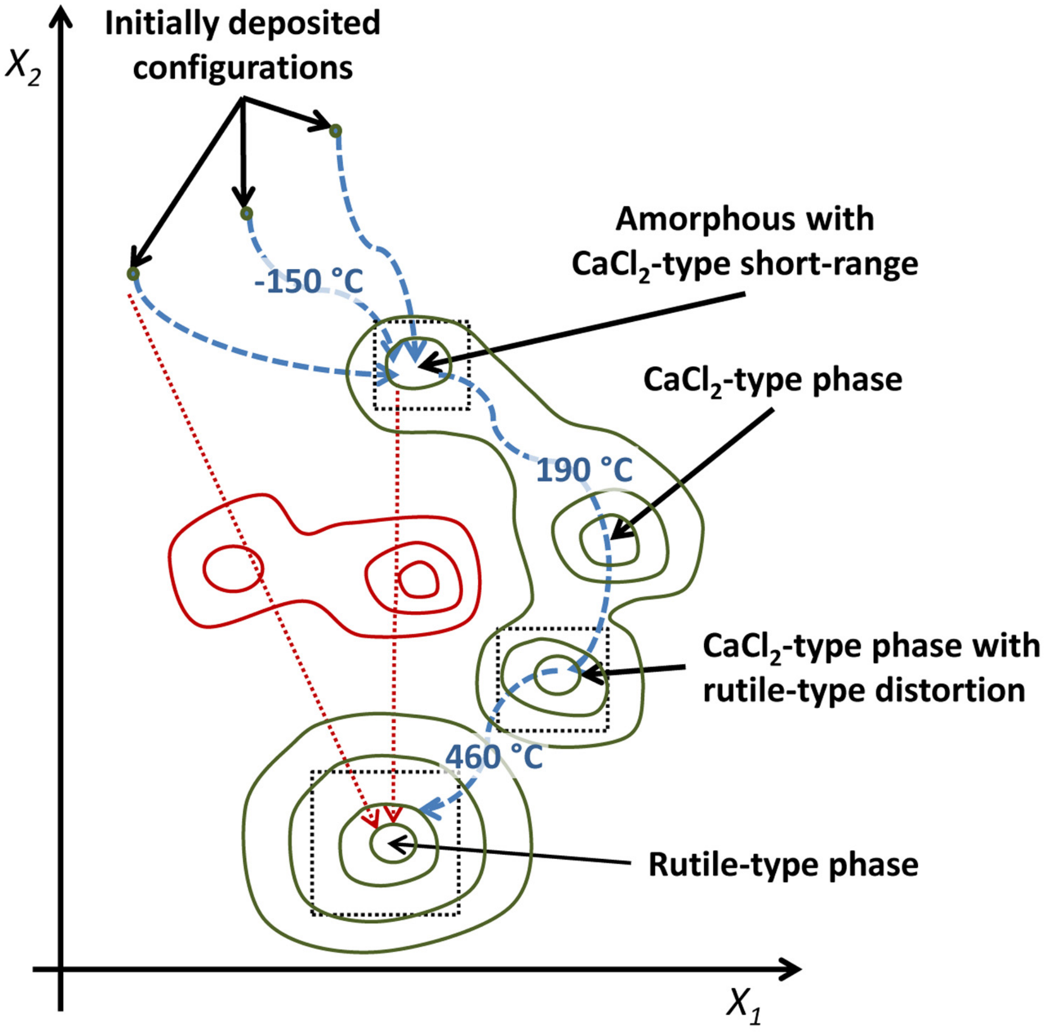

Figure 5.13: Sketch of the structure evolution on the explored energy landscape of the MgF_2 system. Blue level lines delineate minima regions representing metastable structures; and red level lines delineate mountain regions representing thermodynamically forbidden structures. Black dot boxes correspond to experimentally observed phases. Blue dashed lines illuminate directions of random walks of system configurations at the experimental annealing temperature; red dashed lines demonstrate two forbidden paths for the experimental annealing strategy.

The structure evolution is summarized using a schematic of the energy landscape of the MgF_2 system as follows (Fig.5.13): An amorphous MgF_2 film is formed by low-temperature atom beam deposition at 123 K. The deposited MgF_2-clusters undergo movements to reach configurations corresponding to a local minimum in the energy landscape of the MgF_2 system. The rearranged structure possesses the same short-range structure as the $CaCl_2$-type phase. Because of the low temperature no long-range motion of atoms is possible and the rearranged structure does not show long-range order.

When the temperature reaches 458 K, the random motion of Mg and F atoms is sufficiently increased in the amorphous phase to allow ordering to take place. Owing to the high density of the local $CaCl_2$-type atomic arrangement in the amorphous phase, structure development towards the rutile-type phase is suppressed. Instead, a thermodynamically metastable phase with $CaCl_2$-type structure develops with nanometer-sized grains and disordered grain boundaries. This phase constitutes a local minimum in the energy landscape with lower (free) energy than the experimentally observed amorphous phase. The new metastable phase contains structural features of both the $CaCl_2$-type structure (at long-range) and the rutile-type (at short-range).

At temperatures above 653 K, Mg and F atoms gain enough thermal activation in order to overcome the (free) energy barrier between the nanocrystalline $CaCl_2$-type phase and the nanocrystalline rutile-type phase. Hence, the structural configuration finally reaches the global minimum on the energy landscape, namely the thermodynamically stable rutile-type phase. However, disorder at grain boundaries still exists in this final state. This implies that a high energy barrier exists between the polycrystalline arrangement of nano-sized rutile-type crystals and the perfect single-crystalline rutile-type phase.

5.4 Conclusion

By a combination of electron diffraction, a modified PDF analysis, and MD simulations, the short-range order of the amorphous phase and the distorted crystalline phase were analysed. Raw simulation data were used without any structure refinement aiming at an optimization of the two data sets. The excellent correspondence of experimental and MD data is a strong evidence for the reliability of the PDFs from electron diffraction and the high quality of the used interatomic potentials, and gives us high confidence in our data analysis.

This study successfully answered open questions of previous studies: the short-range structure of the amorphous phase was detected and the previous assumption of the existence of $CaCl_2$-type nuclei in the amorphous phase was confirmed. It is shown that the observed $CaCl_2$-type phase contains structural features of both, the metastable $CaCl_2$-type in the long range and the rutile-type in the short range. Disordered intergranular regions were found which most likely stabilize the $CaCl_2$-type phase.

As an extension of the present work, the exploration of the phase behaviour of other metal fluorides, such as other earth alkali fluorides, will be shown in next the chapter, in order to clarify the influence of, e.g., the cation ionic radii and of the addition of a second cation, like in $(Ca,Ba)F_2$.

6 Other alkaline earth fluorides

6.1 Pure binary alkaline earth fluorides (CaF_2, SrF_2, BaF_2)

Calcium fluoride (CaF_2), strontium fluoride (SrF_2) and barium fluoride (BaF_2) were investigated. The naturally stable crystalline CaF_2, SrF_2, and BaF_2 phases possess the isostructural fluorite structure (Fm3m, space group No.225), as shown in figure 6.1, which is different from the MgF_2. Cations form a face-centred cubic lattice (fcc). Eight fluoride atoms form a simple cubic structure inside the fcc cell. Four cations surround one fluoride forming a tetrahedron. Two adjacent tetrahedra link via one edge.

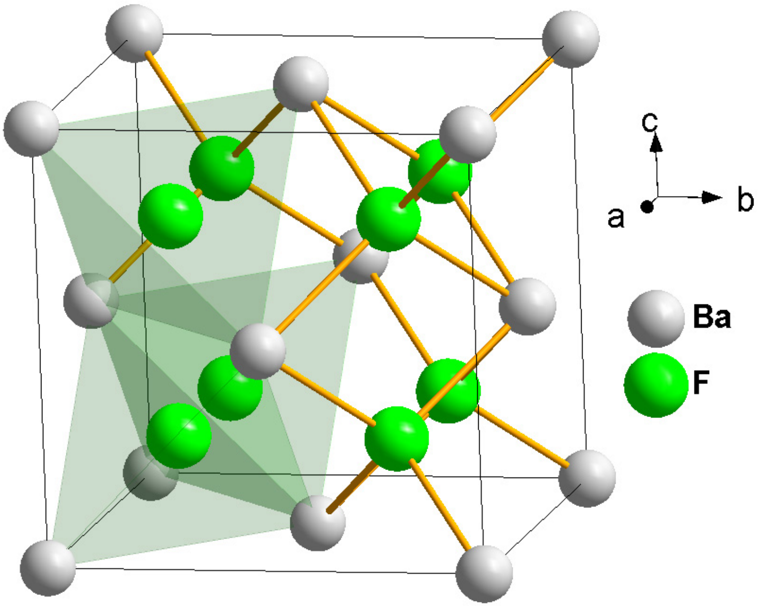

Figure 6.1: The fluorite structure, which contains a face-centred cubic arrangement of cations (grey) and a simple cubic arrangement of fluoride anions (green).

Because of the structural difference to MgF_2, the structure evolution from the amorphous phase to the polycrystalline phase is expected to be different from MgF_2. Moreover, the differences among the CaF_2, SrF_2 and BaF_2, are also interesting for understanding the radius size effect of the cations.

The in-situ diffraction experiments show that the amorphous phases of CaF_2, SrF_2, and BaF_2 directly crystallize to the fluorite structure by annealing. No intermediate phases are found. The transition temperatures of all three structures are the same (273±10 K).

Figure 6.2 shows PDFs extracted from the in-situ diffraction data. Due to multiple scattering of the electron beam, the heights of the PDF curves were normalized at the first pronounced peak, which is the first coordination shell of cation–F. The PDFs in Fig. 6.2 depict the experimentally observed structure evolution of CaF_2, SrF_2 and BaF_2. The solid lines obtained at low temperature (193 K) exhibit strongly damped oscillations at large r-values, which prove that the samples produced at liquid nitrogen temperature are amorphous. The dotted lines obtained at room temperature (303 K) exhibit distinctively pronounced peaks, which, along with their positions, prove that the annealed samples have crystallized with fluorite structures (Fm3m).

The PDFs of both the amorphous and crystalline phases among the three compounds are very similar. Therefore, in following the PDFs of CaF_2 is used as an example to discuss all three compounds. The first pronounced peak of the crystalline PDF at 2.36 Å corresponds to the first coordination shell of Ca–F. The second pronounced peak of the crystalline PDF at 3.87 Å corresponds to the first coordination shell of the Ca–Ca and the second coordination shell of F–F, where the first one relates to the short-range structure of F-centred tetrahedra and the second one corresponds to the ordering of the F-centred tetrahedra. The third pronounced peak of the crystalline PDF at 4.58 Å corresponds to the second coordination shell of the Ca–F, which relates to the structure of the simple F cube. The PDF of the amorphous CaF_2 shows only three pronounced peaks. They have similar positions as the discussed three pronounced peaks in the crystalline PDF. This indicates that the three peaks in the amorphous PDF correspond to the same atom pairs as in the crystalline PDF. Thus, a strongly distorted short-range order exists in the amorphous phase: distorted F-centred tetrahedra and partially ordered adjacent tetrahedra which are disordered in the long range. Furthermore, the first peak in the

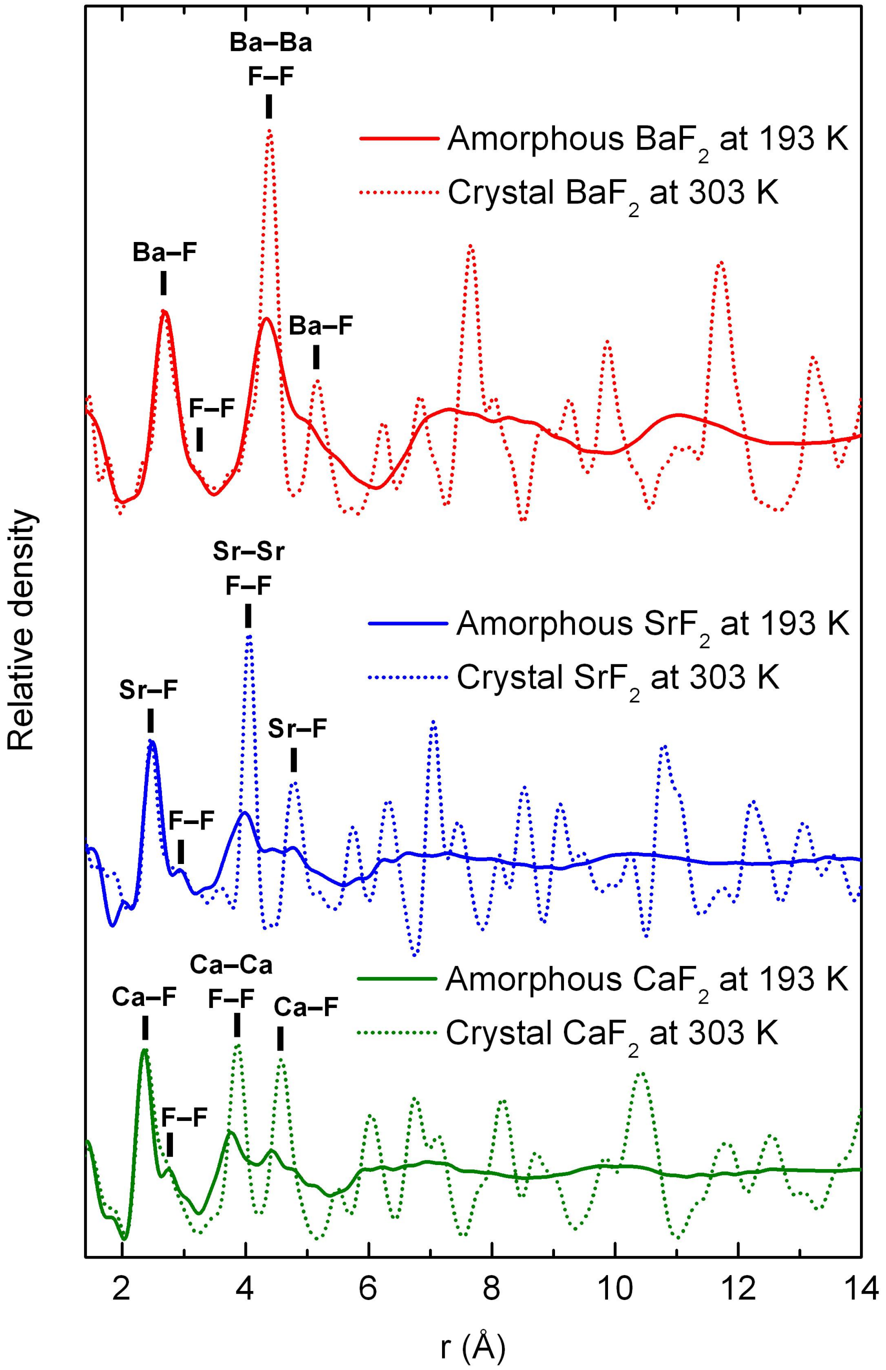

Figure 6.2: Experimentally measured PDFs of the amorphous phase (solid lines) at 193 K and the crystalline phase (dotted lines) at 303 K of CaF_2 (bottom, green), SrF_2 (middle, blue), and BaF_2 (top, red) at 303 K. The black lines label the first coordination shell of cation–F, F–F, cation–cation and the second coordination shell of F–F and cation–F, respectively.

PDF of amorphous CaF_2 has almost the same width as for crystalline CaF_2 revealing that the Ca–F bonding distances in the amorphous phase are almost identical to those in the crystalline phase. This proves the stability of the short-range structure in the amorphous phase. The situations are the same for the other two compounds, SrF_2 and BaF_2. The differences of the more pronounced second peak and reduced third peak are due to the different scattering factors between Ba, Sr, and Ca.

These results suggest the following structure evolution. Despite the long-range disorder, tetrahedra are well ordered on a small length scale in the amorphous structure. Such locally ordered regions have low potential energy and act as nuclei for the crystallization during annealing.

6.2 Mixture of calcium difluoride and barium difluoride (($Ca_{0.5}Ba_{0.5}$)F_2)

6.2.1 In-situ diffraction and HRTEM

The two fluoride compounds were deposited simultaneously with 1:1 atomic ratio on a 2 nm thick amorphous carbon substrate by the LT-ABD technique at 123 K. Hence the Ca and Ba cations were randomly mixed on the atomic level. The structure of the mixture is initially amorphous as confirmed by electron diffraction measured at 123 K. The diffraction pattern (Fig. 6.3a) and the corresponding structure factor (Fig. 6.3d, black line, bottom) are recorded at 303 K. No structural changes are detected up to this temperature.

After annealing, the amorphous specimen crystallizes at around 643 K and forms a polycrystalline phase with fcc structure shown by the diffraction pattern recorded at 673 K (Fig. 6.3b) and the corresponding structure factor (Fig. 6.3d, red line, middle). An HRTEM image taken along the [111] direction of one crystal (Fig. 6.4b) enlarged from Fig. 6.4a (white dashed box) as well as its Fourier transform (Fig. 6.4c) further confirm the fcc structure. Red lines in Fig. 6.4a encircle some pronounced $CaBaF_4$ nanocrystals, which shows that the grain size is around 8–15 nm. In addition, EFTEM EELS mapping of Ba (N-edge) and Ca (L-edge) and EDX measurements prove that Ba and Ca are homogeneously mixed in the film. Therefore, the crystalline phase formed

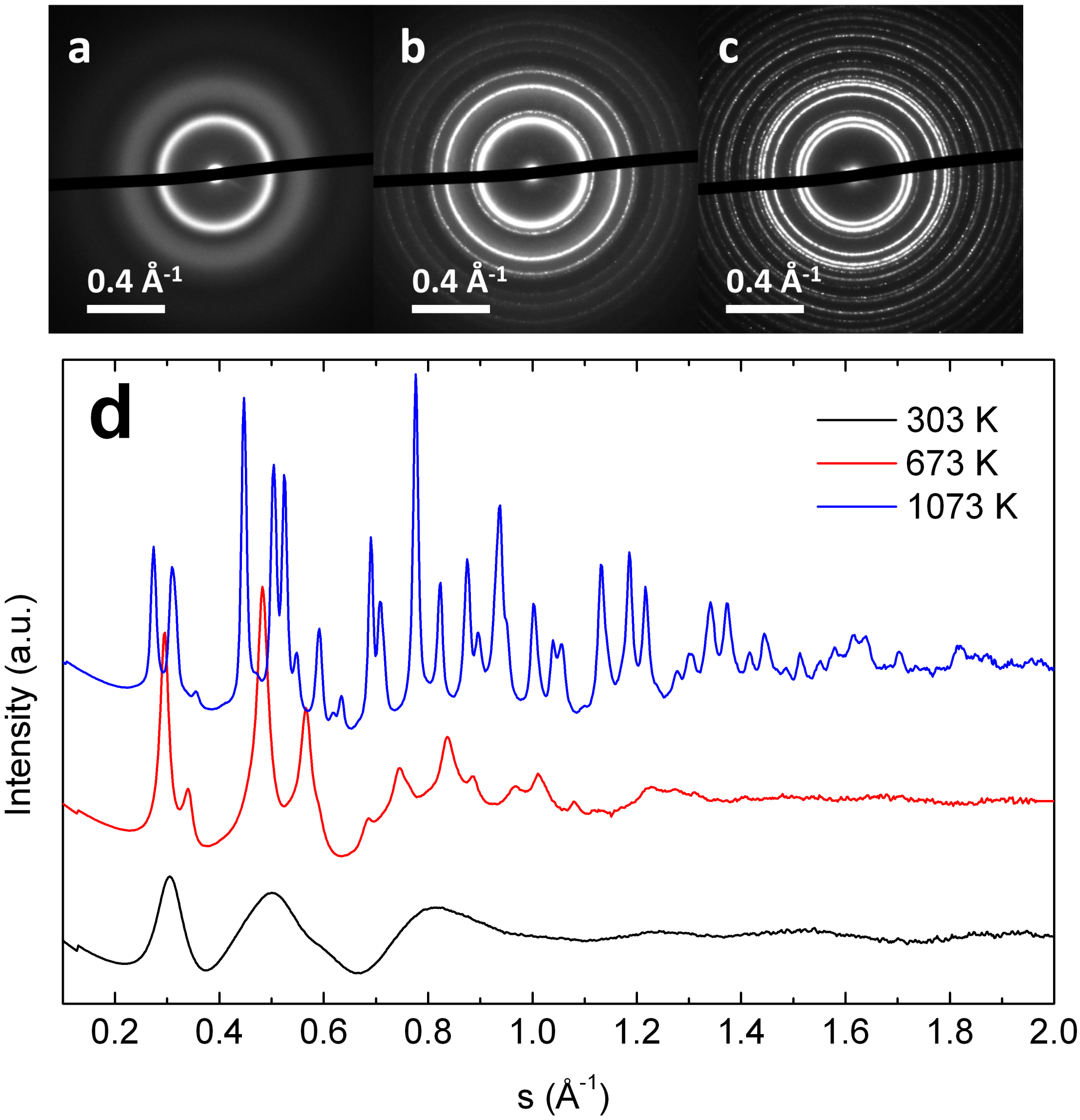

Figure 6.3: Experimentally measured electron diffraction patterns recorded at (a) 303 K, (b) 673 K, and (c) 1073 K of the $CaBaF_4$ film. (d) Temperature dependent structure factors determined from the diffraction patterns in (a, b, c).

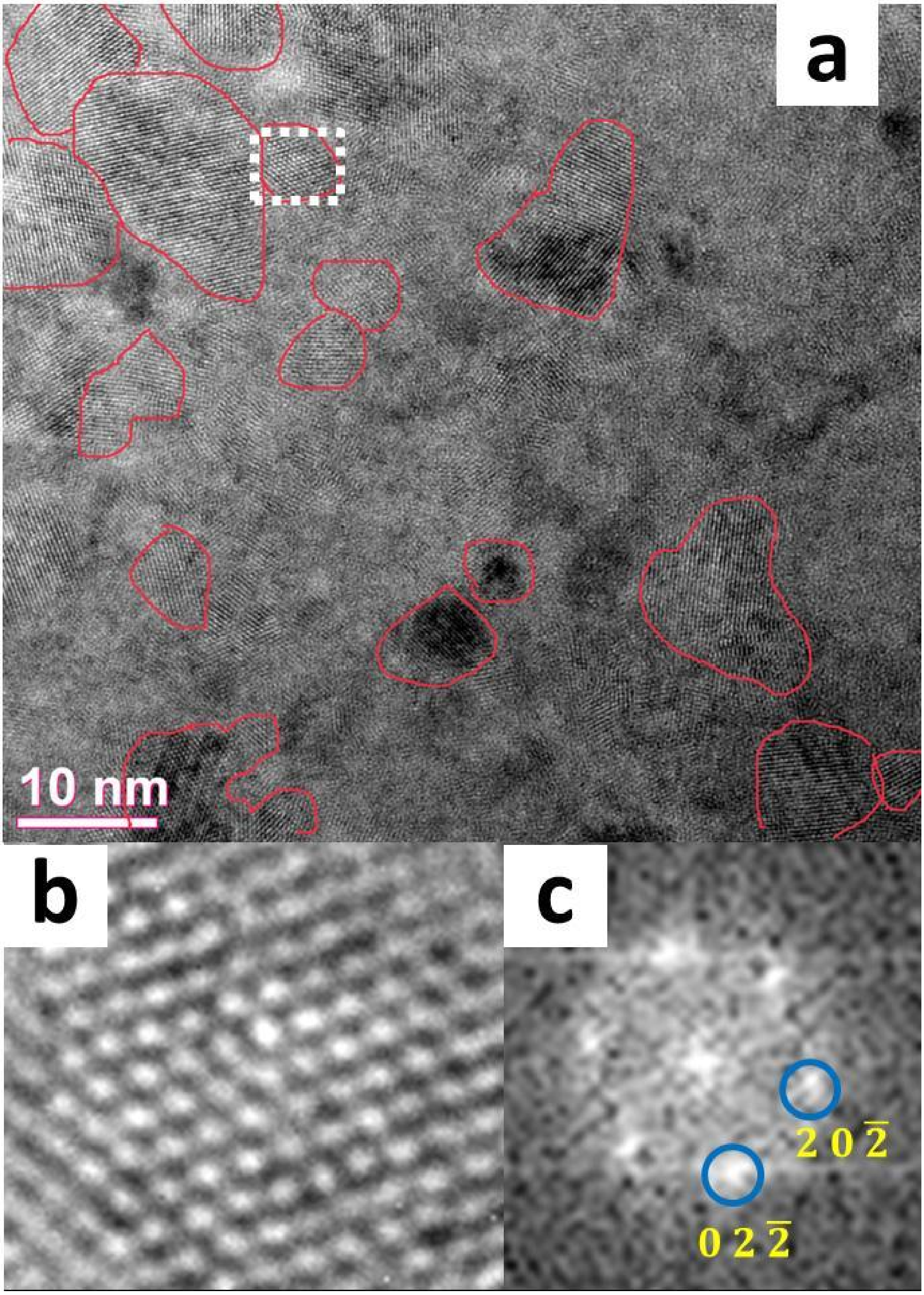

Figure 6.4: (a) HRTEM image of the solid-solution phase recorded at 673 K. (b) Enlarged image from the white dashed box in (a) showing the [111] direction of the fcc crystal. (c) The Fourier transform of (b), where two indexes of the corresponding planes with regard to the bright spots are indicated.

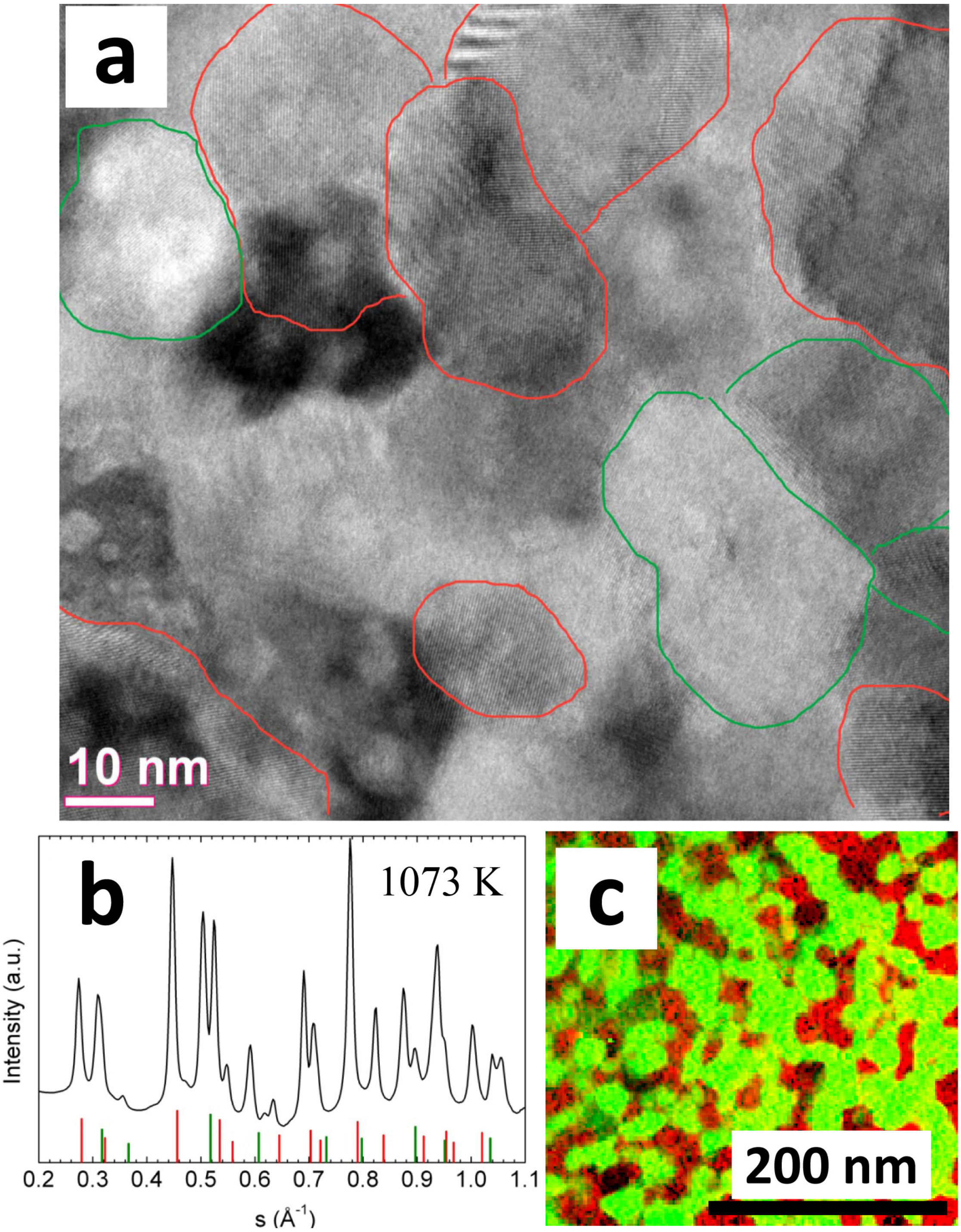

Figure 6.5: (a) HRTEM image of the phase-separated material recorded at 1073 K (BaF_2: red, CaF_2: green). (b) The enlarged structure factor of the blue line (1073 K) in Fig. 6.3 (d). The lines at the bottom represent calculated diffraction peaks (BaF_2: red, CaF_2: green). (c) EFTEM chemical mapping of the phase-separated material (green: Ca-$M_{2,3}$ signal, red: Ba-$N_{4,5}$ signal).

at 643 K should be a solid-solution phase with fluorite (Fm3m) structure as shown in Fig. 6.1. Ca and Ba ions occupy the fcc positions with equal probability according to the stoichiometric ratio. Due to interest in ionic conductivity properties of CaF_2 and BaF_2, Heitjans et al have reported the solid-solution phase which was synthesized by ball milling crystalline CaF_2 and BaF_2 particles [81–83]. In this work the solid-solution phase was obtained by the annealing process from the initially amorphous phase and the main focus is on the viewpoint of the structure evolution.

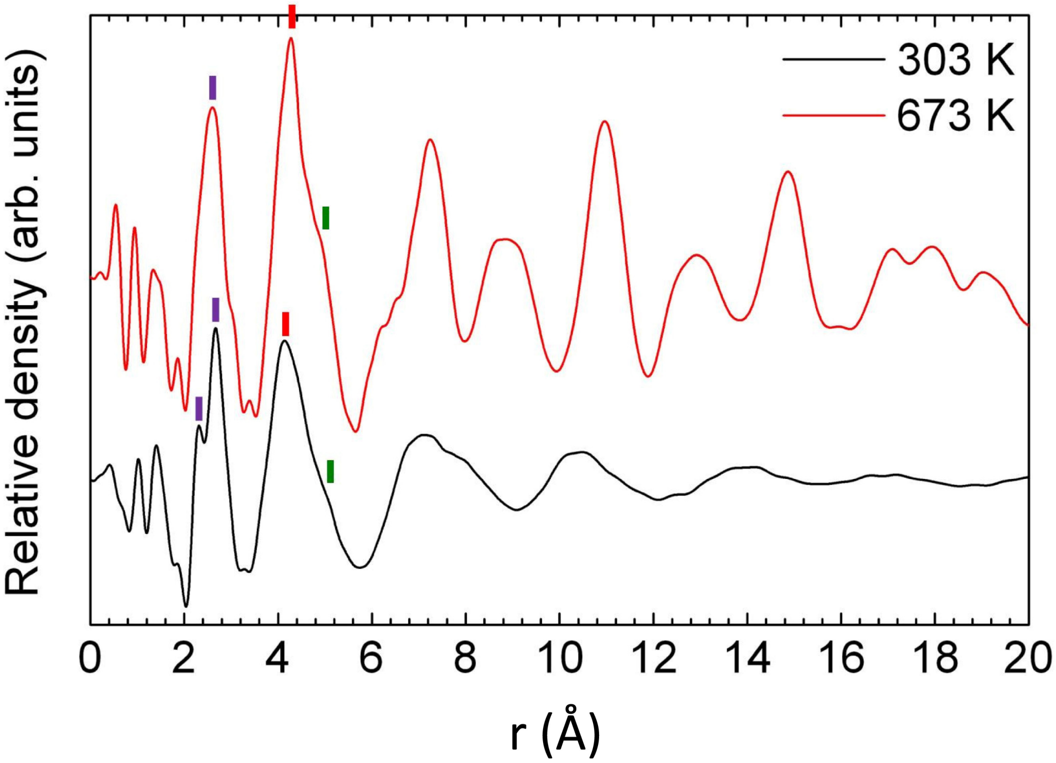

Figure 6.6: Experimental PDFs of the amorphous $(Ca_{0.5}Ba_{0.5})F_2$ phase (black, bottom) and the solid-solution $CaBaF_4$ phase (red, top). The violet lines indicate cation–F bond distance, the red lines indicate cation–cation nearest distance, and the green lines indicate cation–F second nearest distance.

With increasing temperature, the specimen undergoes a second crystallization at around 753 K and forms a third phase, shown by the diffraction pattern recorded at 1073 K (Fig. 6.3c) and the corresponding structure factor (Fig. 6.3d, blue line, top). This new phase is an elementally separated polycrystalline phase containing CaF_2 nano-crystals and BaF_2 nano-crystals. This elemental separation is confirmed by the comparison between the experimentally measured structure factor and the calculated diffraction peaks for pure CaF_2 [84] and BaF_2 [85] using bulk crystal data (Fig. 6.5b). Chemical mapping (Fig. 6.5c) of Ca ($M_{2,3}$ edge) and Ba ($N_{4,5}$ edge) obtained by acquiring EFTEM image series (in the energy range of 0–135 eV with a 2 eV energy slit) further confirms the phase separation. The HRTEM image (Fig. 6.5a) highlights the pronounced CaF_2 (green) and BaF_2 grains (red) and shows that the grain size is around 20 and 50 nm.

The PDF of the amorphous $(Ca_{0.5}Ba_{0.5})F_2$ state (black, bottom, Fig. 6.6) shows damped peaks at long-range, but strongly pronounced peaks in the short-range. The first measured pronounced peak is split into two peaks at 2.31 Å and 2.67 Å (Fig. 6.6, violet lines on the black line, bottom). This implies that the nearest bond distances between Ca–F and Ba–F are different. The measured bond distances deviate slightly from the literature data of bulk CaF_2 [84] and BaF_2 [85], where the Ca–F bond length is 2.37 Å and the Ba-F bond length is 2.68 Å . The second pronounced PDF peak of the amorphous phase corresponds to the cation-to-cation distance. It implies the existence of short-range order of Ca_4F and Ba_4F tetrahedra in the amorphous phase. The Ca_4F and Ba_4F tetrahedra have different volume and are randomly connected to form the amorphous network, schematically shown in Fig. 6.7.

In contrast, the PDF of the solid-solution shows more pronounced peaks in the long-range, but peaks in the short-range are still as broad as for the amorphous PDF. One notable change is that the first two peaks of the amorphous phase merge together to one single maximum, i.e. only one peak exists at 2.60 Å in the solid-solution. Therefore, it can be suggested that after annealing the isolated Ca_4F and Ba_4F tetrahedra (Fig. 6.7a) in the amorphous phase merge together and consequently Ca–F and Ba–F bonds balance their length to an average value to form a fluorite crystal (Fig. 6.7b). Because of the different equilibrium distance of Ca–F and Ba-F pairs, the solid-solution crystalline unit must be strongly distorted leading to broad peaks in the short-range.

The change of the Ca–F and Ba–F average bond lengths causes an average volume increase of the Ca_4F tetrahedra from the amorphous phase to the solid-solution phase, and simultaneously a volume decrease of the Ba_4F tetrahedra from the amorphous phase to the solid-solution phase. The volume changes result in a strong (potential) energy barrier between the amorphous and the solid-solution structure. This barrier sufficiently

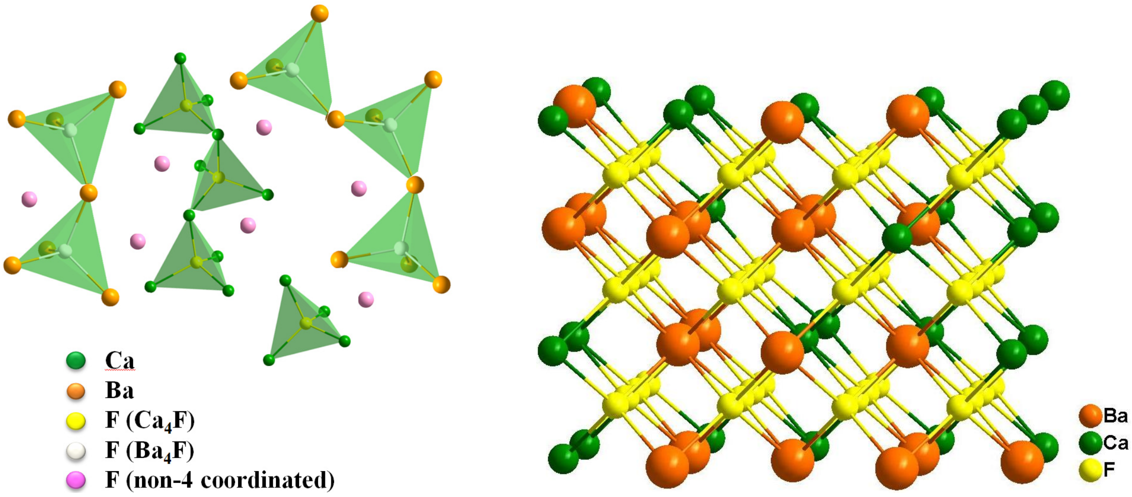

(a) (b)

Figure 6.7: (a) Sketch of the assumed amorphous $(Ca_{0.5}Ba_{0.5})F_2$ network constructed by Ca_4F and Ba_4F tetrahedra. Some F (pink) ions are in a hybrid coordination environment. Some of them are even non-4-fold coordinated. (b) The solid-solution crystalline structure (fluorite), where the Ca^{2+} and Ba^{2+} occupy the fcc atomic positions with a probability of 1/2 (50%).

stabilizes the amorphous phase of the mixture at high temperature compared to the amorphous phase of the pure CaF_2, SrF_2, and BaF_2 discussed previously (chapter 6.1).

The strongly distorted crystalline lattice of the solid-solution phase as well as the deviation of the bond length causes large additional energy which unstabilizes the structure. By further heating (> 753 K), one species of cations can easily diffuse away from the solid-solution phase under formation of chemically separated phase.

6.2.2 Energy-loss near-edge structure (ELNES) analysis

Figure 6.8 shows the fluorine-K edge for the different phases. The differences of the near-edge fine structures among the three phases are clearly observed, which differences correspond to the different chemical environments of the F^- ions for the different structures.

Figure 6.9 shows a comparison of the F-K edge between the experimentally measured EELS for the phase-separated phase and the X-ray absorption spectra (XAS) of the

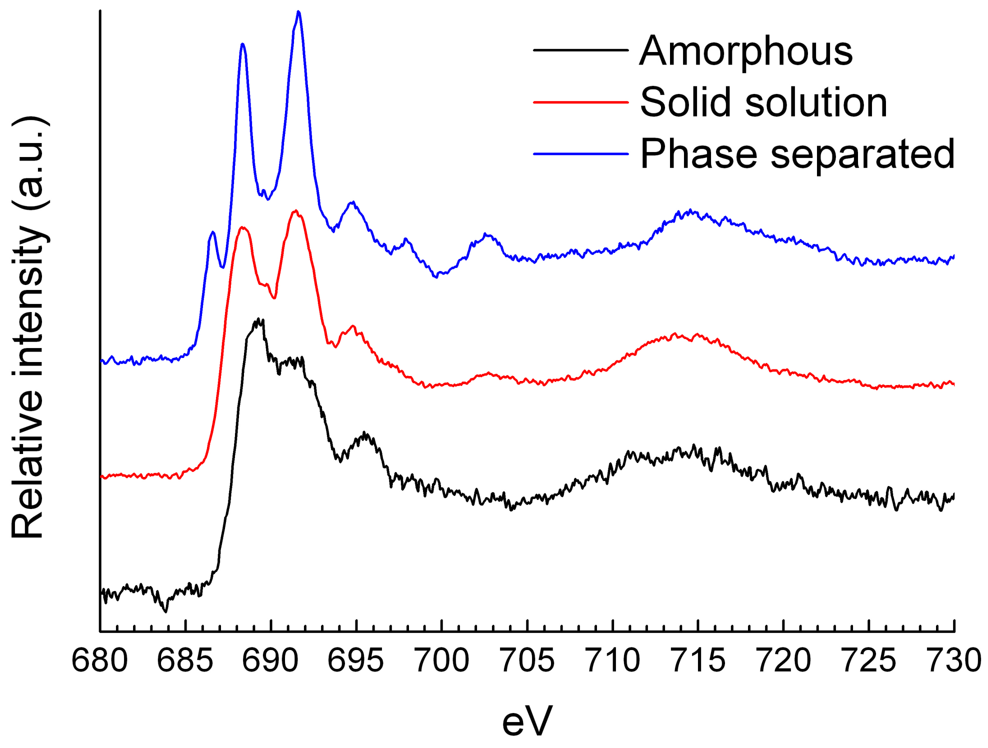

Figure 6.8: EELS of the F-K edge of amorphous phase (black, bottom), solid-solution phase (red, middle), and BaF_2+CaF_2 separated phase (blue, top).

pure compounds BaF_2 and CaF_2 from reference [86]. This comparison shows that the F-K edge of the EELS data of the phase-separated phase (blue, solid) has the same features as the dashed red line which is a superposition of the XAS of pure CaF_2 (green, solid) and pure BaF_2 (green, solid). This further proves elemental separation. The onset energy of the F-K edge of BaF_2 is 1.3 eV lower than that of CaF_2 because the Ba–F bond length in the crystalline BaF_2 is larger by 12% than the Ca–F bond length in the crystalline CaF_2.

For the solid-solution phase, the experimental EELS spectrum is compared to the XAS data (Fig. 6.10). The onset energy of the F-K edge of the solid-solution phase (Fig. 6.10, pink solid line) is 0.5 eV lower than that of the BaF_2 + CaF_2 superposition (Fig. 6.10, blue dashed line) and in between those of the onset of BaF_2 (Fig. 6.10, orange solid line) and CaF_2 (Fig. 6.10, green solid line). This can be understood because the bond length of F-cations in the solid-solution phase is in between those of pure CaF_2 and BaF_2.

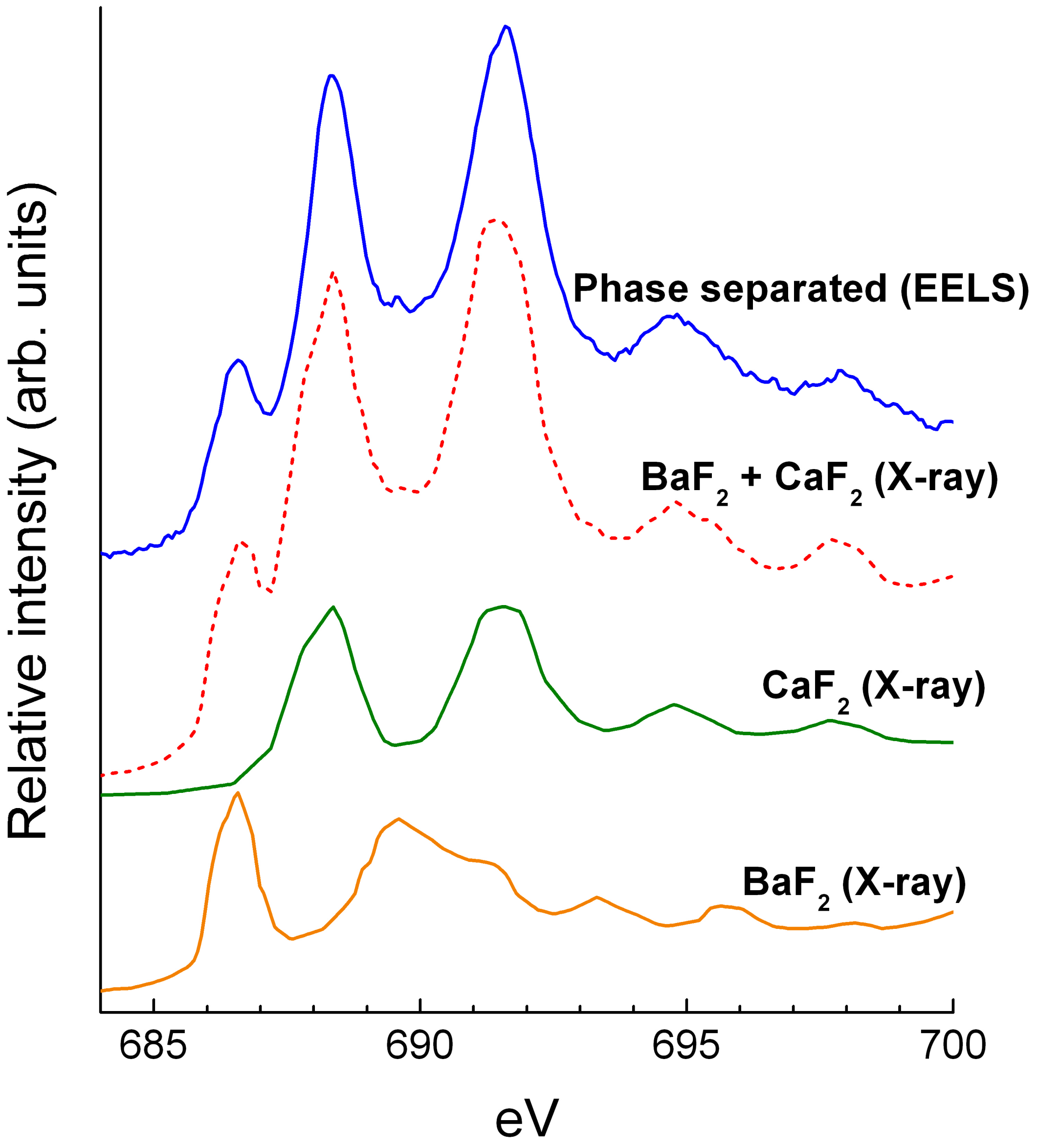

Figure 6.9: Comparison of the F-K edge of the phase-separated material between the EELS experiment data (blue, solid) and X-ray absorption spectra of pure BaF$_2$ (orange, solid), pure CaF$_2$ (green, solid) as well as their superposition (red, dashed) [86].

To gain better understanding of the spectra, calculations of the F-K edge of the solid-solution were done by using the FEFF8 code [87, 88]. To simulate the disordered distribution of Ba^{2+} and Ca^{2+} ions in the fcc arrangement, the model of the solid-solution is built for five different coordination conditions of the first shell of the centred F^- ion: the F^- coordinated with four Ba^{2+} ions (F–Ba4) in the tetrahedral configuration; with three Ba^{2+} ions and one Ca^{2+} ion (Ca–F–Ba3); and so on, (Ba2–F–Ca2); (Ba–F–Ca3); until (F–Ca4) where all Ba^{2+} ions are replaced by Ca^{2+} ions in the tetrahedron. All other atoms in the outside shells follow the fluorite structure, and Ba^{2+} and Ca^{2+} ions are put on the fcc cationic positions with both occupancies of 50%. The cell size (a = 6.018 Å) was adopted as the value measured by electron diffraction (Fig. 6.3d, red line, middle), in which the error bar is given as ±0.01 Å. Six coordination shells are included in the calculation. The core-hole effect is considered by using a Z+1 approach. Finally, the calculated five spectra are add with the same weight to simulate the solid-solution spectrum.

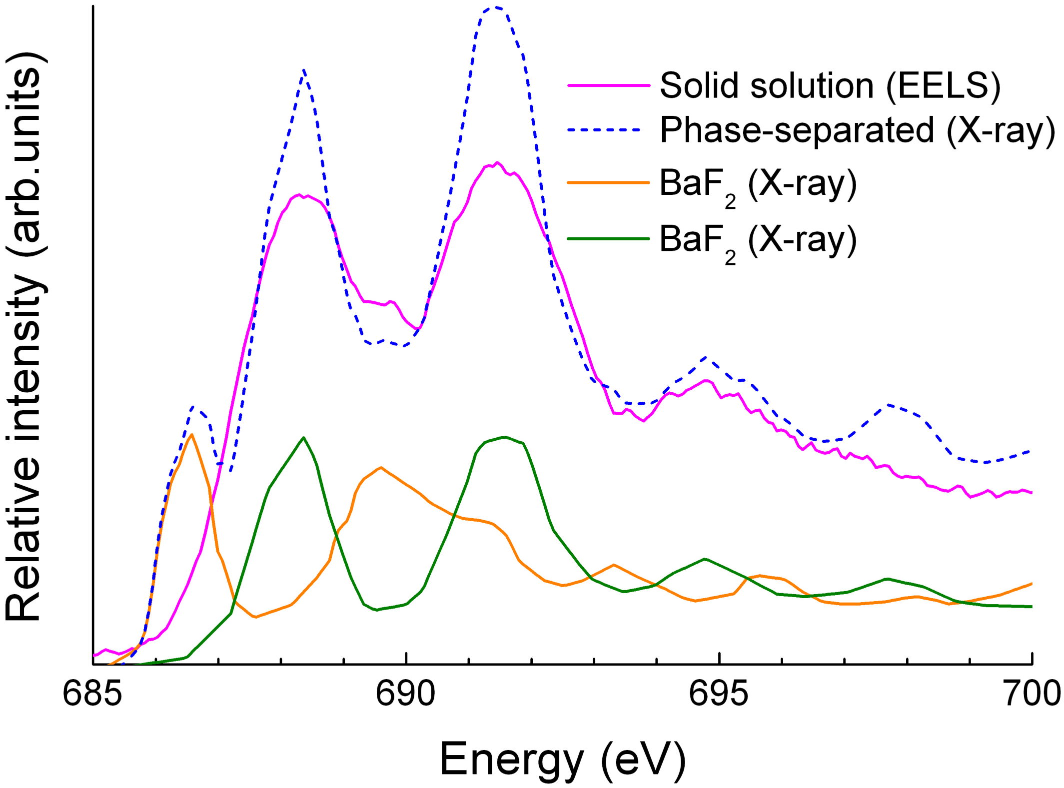

Figure 6.10: Comparison of the F-K edges between experimental EELS spectra for the solid-solution phase (pink, solid) and X-ray absorption spectra for pure BaF_2 (orange, solid) and CaF_2 (green, solid) as well as their superposition (blue, dashed) [86].

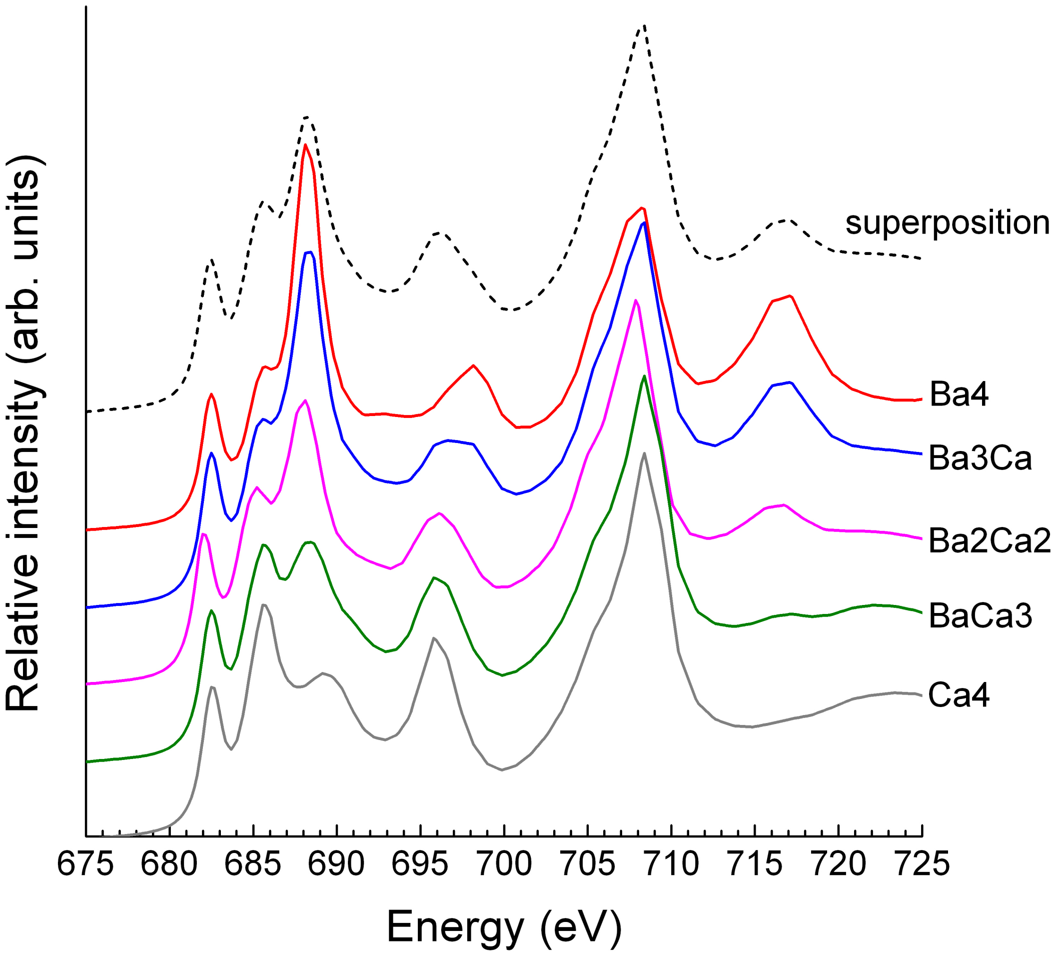

Figure 6.11: EELS F-K edge spectra calculation by the FEFF8 code. The solid lines are the spectra for different coordination environments of the central F^- ion. The dashed line is a superposition of all solid lines with equal weight, mimicking the calculated F-K edge spectrum of the solid-solution phase.

The calculated spectra are shown in Fig. 6.11, where the solid lines correspond to the five different coordination conditions of the F^- and the dashed line is the calculated solid-solution spectrum as a sum of the five solid lines. The solid lines (Fig. 6.11) reveal the gradual changes of the spectra with the change of the coordination conditions. One notable point is that the onset energy (i.e. the chemical shift) is not affected by the next-neighbour atom species. It confirms the assumption that the onset energy in the fluorite structures BaF_2 and CaF_2 mainly depends on the bond distance, rather than

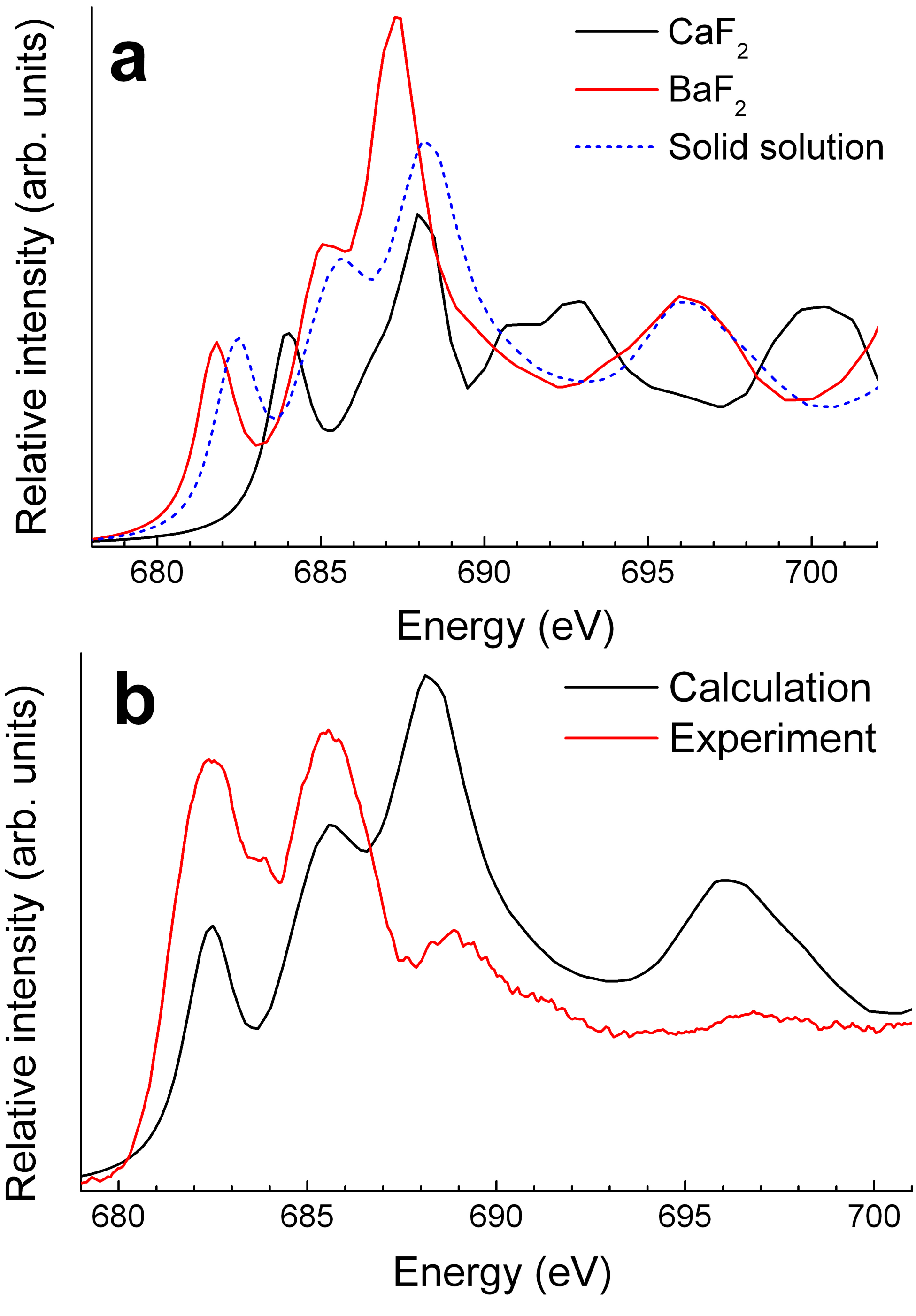

Figure 6.12: (a) Comparison of the calculated F-K edge spectra between the crystalline fluorite CaF_2 (black, solid), BaF_2 (red, solid), and the solid-solution phase (blue, dashed). (b) Comparison of F-K edge spectra of the solid-solution phase between the simulation (black) and the EELS experiment (red)

the atomic number of the cations. Combining with Fig. 6.10, the onset energies seem to be inversely proportional to the cation–F bond distance.

Beside the simulation of the solid-solution spectrum, the F-K edges of the crystalline fluorite CaF_2 and BaF_2 are also calculated. Fig. 6.12a shows a comparison of the calculated F-K spectra of crystalline CaF_2, BaF_2, and the solid-solution phase. The spectra of CaF_2 and BaF_2 are not identical to the XAS data (Fig. 6.9, Fig. 6.10), but have comparable peaks and peak positions, i.e. the calculations are qualitatively reliable. Fig. 6.12a again shows that the behaviour of the onset energies from the calculations agrees with the experimental measurements in Fig. 6.10, i.e. $E_{\mathrm{CaF_2}} > E_{\mathrm{solid-solution}} > E_{\mathrm{BaF_2}}$ as $D_{\mathrm{BaF_2}} > D_{\mathrm{solid-solution}} > D_{\mathrm{CaF_2}}$, where E is the onset energy, and D is the cation–F bond length.

The simulated solid-solution F-K edge spectrum is finally compared to the experimental EELS F-K spectrum in Fig. 6.12b. All peaks below 702 eV are found in both, the simulated and experimental spectra, and they have the same energy positions. Only the relative intensities between the first and the third peaks are not comparable.

The onset energy of the experimental spectrum of the amorphous phase is even by 0.7 eV higher than the solid-solution experimental spectrum (Fig. 6.8). The reason for this observation remains unclear. Simulating the spectrum requires not only taking the tetrahedral structure into account, but also considering other non-equilibrium phases, because the non-tetrahedrally coordinated F^- ions (Fig. 6.7a pink atoms) can cause high free energy, so that the system is locally in a metastable phase. Further studies are required to solve this problem in the future.

6.3 Mixture of magnesium fluoride and barium fluoride ($(Ba_{0.7}Mg_{0.3})F_2$)

Mg^{2+} ions in rutile-type structure are 6-fold-coordinated by F^-, Ba^{2+} ions in the fluorite-type structure are 8-fold-coordinated by F^-. Moreover, Ba has the largest radius in the alkaline earth metal group (except Ra which is radioactive element). Therefore, the structure evolution of the mixture of MgF_2 and BaF_2 is interesting to be compared with the mixture of CaF_2 and BaF_2. MgF_2 and BaF_2 are deposited simultaneously on a 2 nm

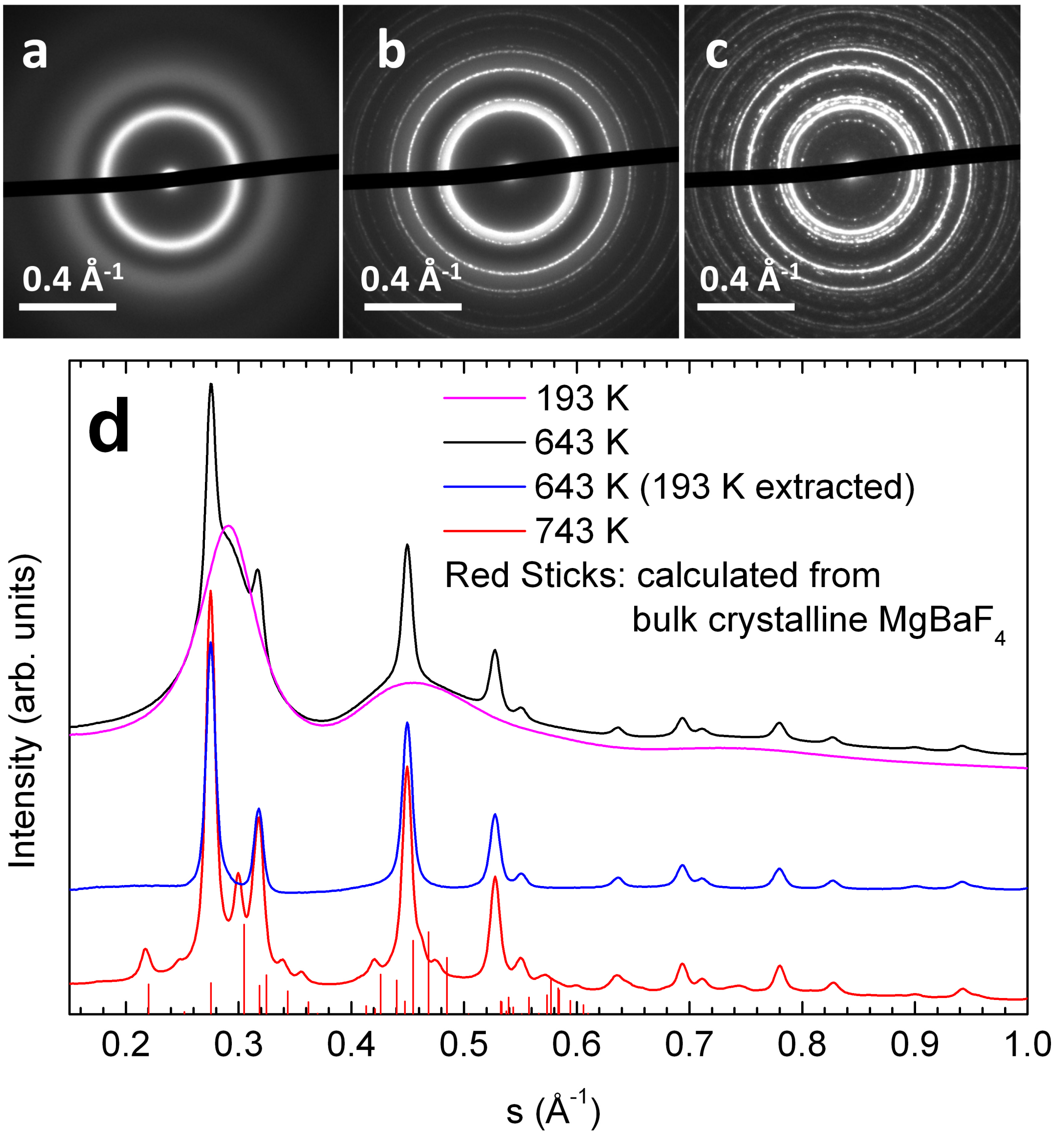

Figure 6.13: Experimentally measured electron diffraction patterns of the $Mg_{0.3}Ba_{0.7}F_2$ film recorded at (a) 193 K, (b) 643 K , and (c) 743 K. (d) The diffraction profiles at 193 K (pink line), 643 K (black line), and 743 K (red line) as well as the profile (blue line) obtained by subtracting the 193 K profile from the 643 K profile and the diffraction peaks calculated from the database of the bulk crystalline $MgBaF_4$ [89] (red lines).

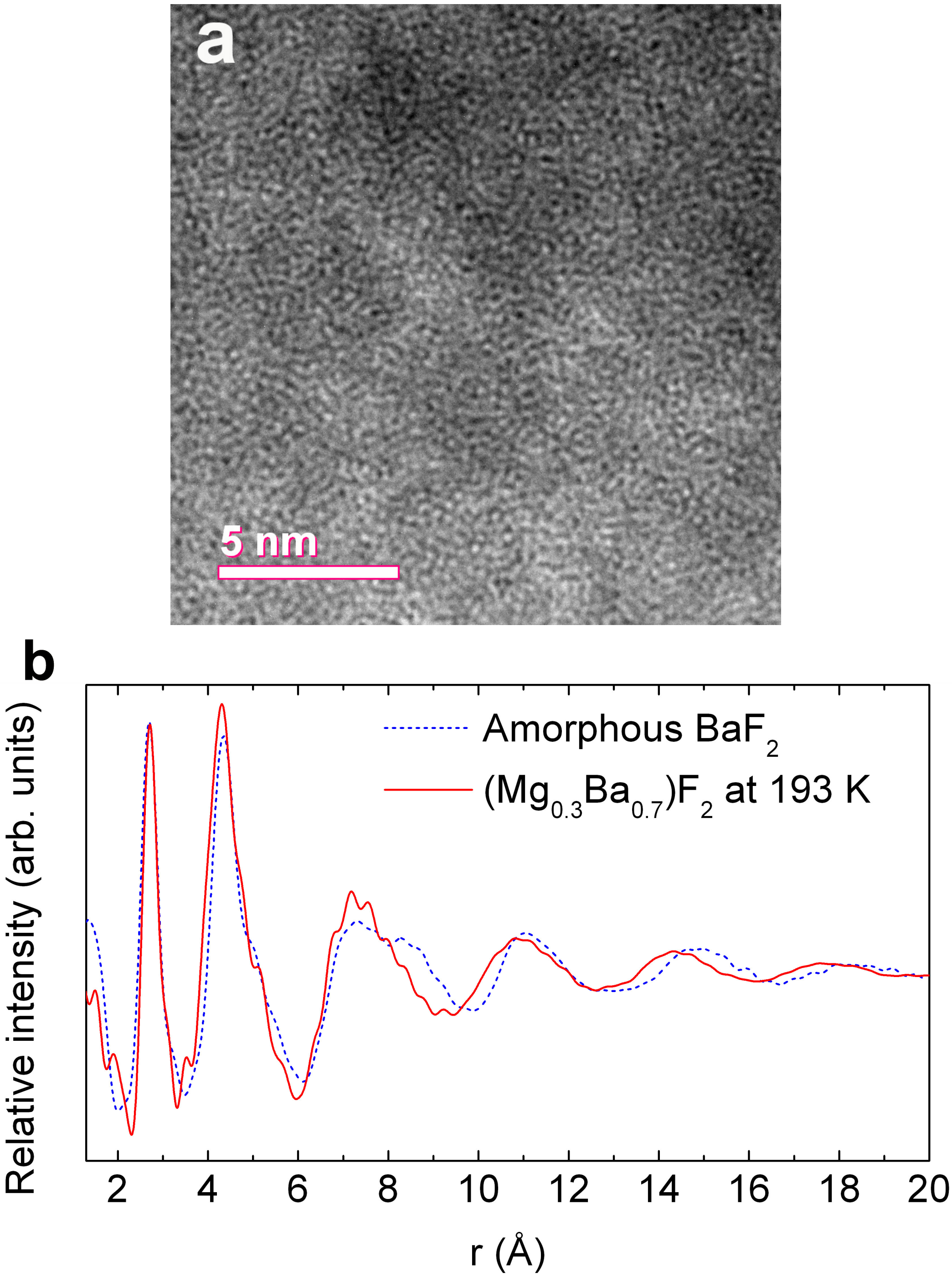

Figure 6.14: (a) HRTEM image of the amorphous mixture. (b) PDF of amorphous $(Mg_{0.3}Ba_{0.7})F_2$ measured at 193 K (red, solid) and of amorphous BaF_2 (blue, dashed) from Fig. 6.2 (red solid) for comparison.

carbon support at liquid nitrogen temperature via the LT-ABD method. In-situ heating experiments are performed in the TEM following the same procedure as discussed in chapter 4.

The experimental results reveal that the mixture is initially amorphous, shown by the diffraction data in Fig. 6.13a and its profile in Fig. 6.13d (pink line). The HRTEM image (Fig. 6.14a) further proves the structure to be amorphous instead of showing nanometer-sized crystals. Figure 6.14b shows the PDF of the amorphous $Ba_{0.7}Mg_{0.3}F_2$ mixture (solid line, red) extracted from the experimental diffraction data and the PDF of amorphous pure BaF_2 (dashed line, blue) taken from Fig. 6.2 (red solid). The PDFs are quite similar. One has to consider that the scattering power of Ba^{2+} ions is much larger than that of Mg^{2+} ions so that signals from the BaF_x clusters in the amorphous mixture are much stronger than those from MgF_y clusters (the x, y subscripts represent the numbers of F for the Ba- and Mg-centred polyhedra). Therefore, the similarity of the two PDFs indicates that the BaF_x clusters in the amorphous mixture have similar structures as in pure amorphous BaF_2. Furthermore the Ba–F distances in the mixture are not strongly influenced by the additional Mg^{2+} ions. The slight differences between the two PDFs are caused by the scattering signals coming from the Mg^{2+} ions and also variations of the structure of the BaF_x clusters compared to the pure amorphous BaF_2 due to additional Mg^{2+} ions. The differences are accumulated with increase of inter-atomic distance.

The amorphous mixture crystallizes when the temperature is increased up to 593 K. Small crystals with sizes of 6–12 nm (Fig. 6.15a recorded at 643 K) form. The diffraction data recorded at 643 K are shown in Fig. 6.13b and d (black line). In addition to the Bragg peaks in the diffraction data, one can see strong diffuse scattered signals, which reveals that the crystallized mixture still contains a large fraction of the amorphous component. The blue line in Fig. 6.13d is calculated by subtracting the amorphous profile (pink line) from the first crystallized profile (black line). This blue line has the same peak positions as the fcc BaF_2 fluorite-type structure. This reveals that the grains in the at 593 K annealed mixture are BaF_2. The amorphous residues should contain all MgF_2 and a part of BaF_2 which will be proven by the following results upon further heating experiments.

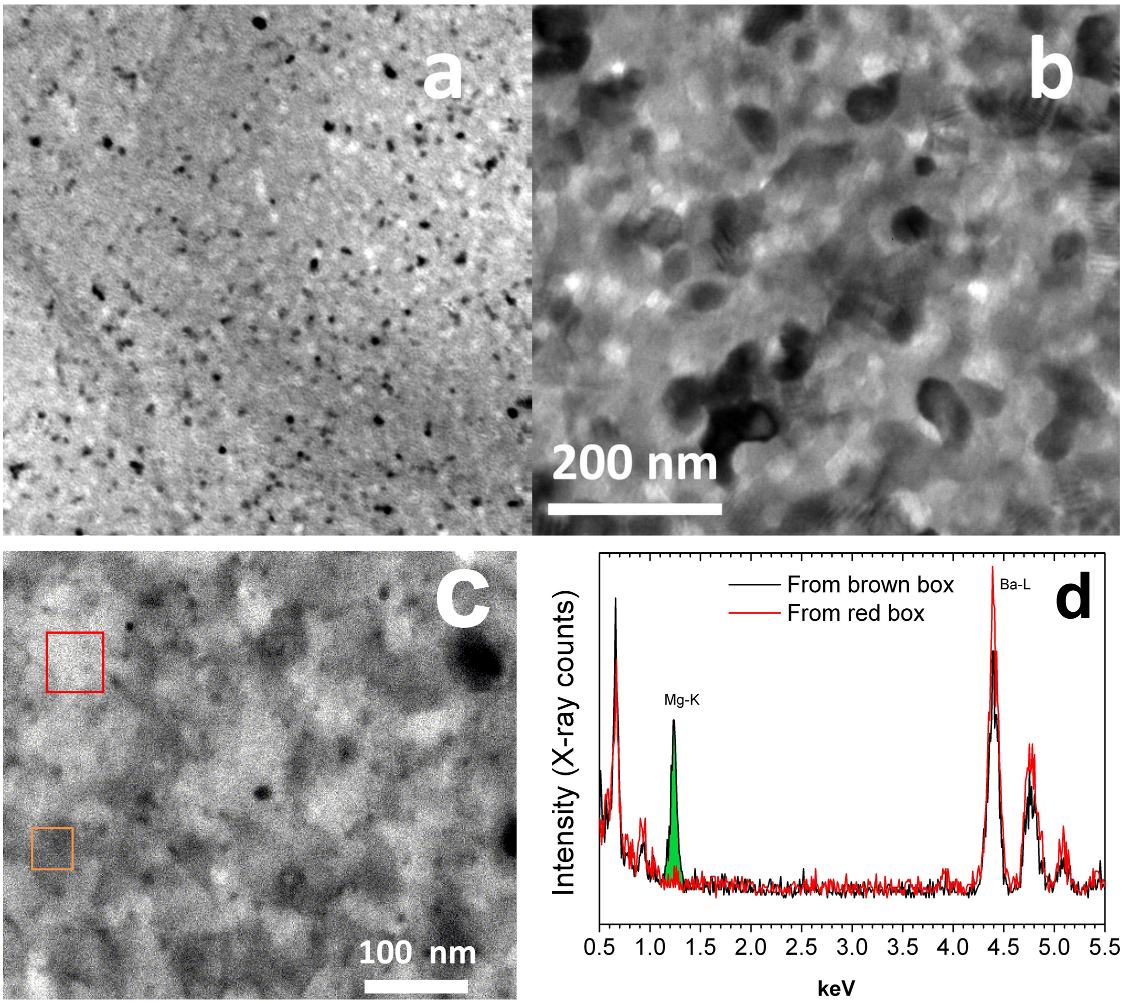

Figure 6.15: BF images of the mixture recorded at (a) 643 K and (b) 743 K. (c) STEM-HAADF image recorded at 743 K. (d) EDX spectra acquired from the areas in the red box (red line) and brown box (black line) in (c), the difference between Mg-K peak of the two spectra is highlighted by green color.

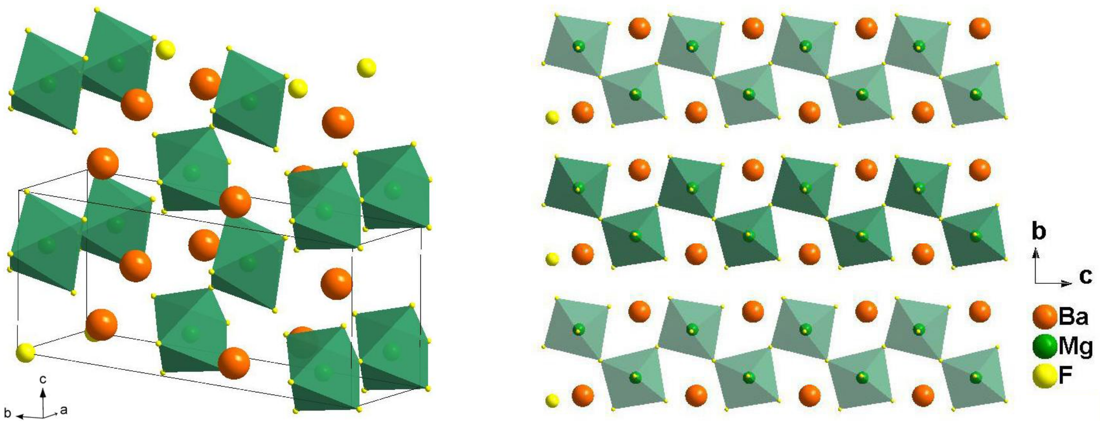

(a) (b)

Figure 6.16: The atomic structure of $BaMgF_4$, (a) Two units stacked along the c axis. (b) overview along the a axis.

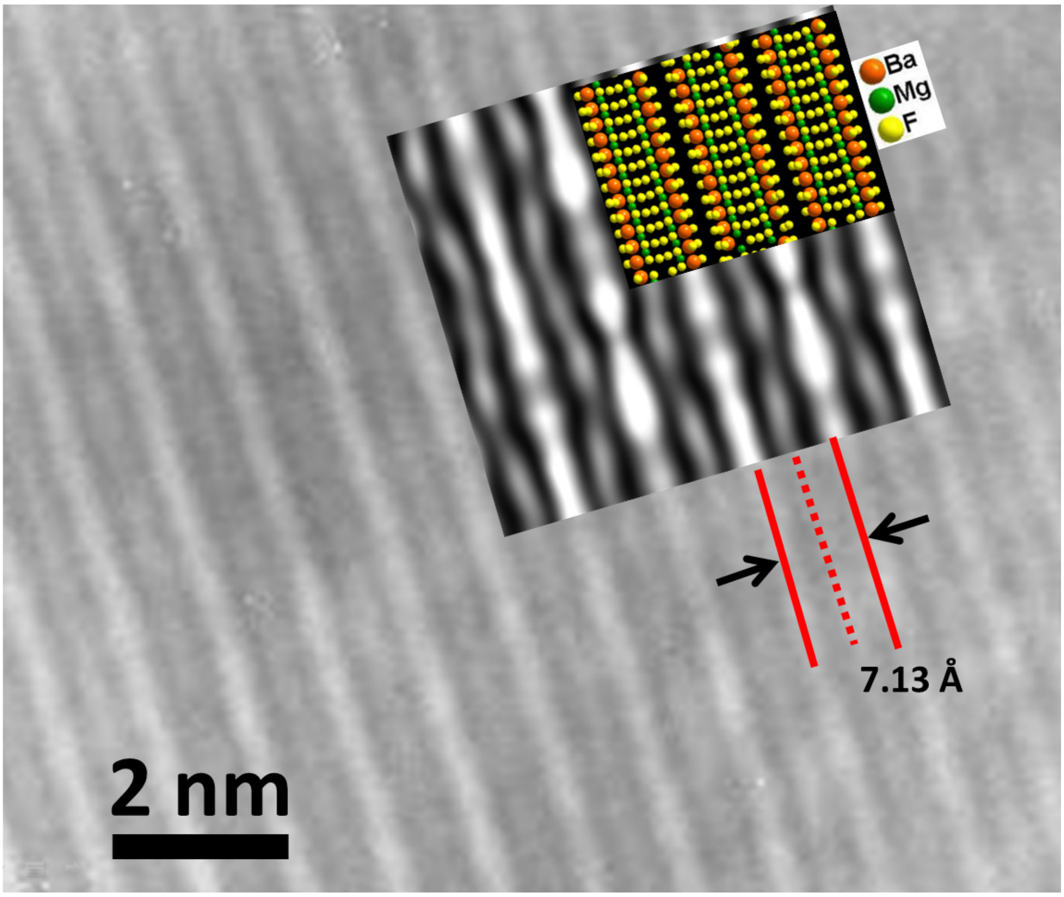

Figure 6.17: HRTEM image of $BaMgF_4$ along the [103] direction. The insert is a simulated image using a multislice algorithm (QSTEM [90]) as well as the structure with the crystalline direction adopted in the simulation.

After high temperature annealing, some additional peaks appear in the diffraction data (Fig. 6.13c and d red line), which is recorded at 743 K. The diffraction data show that the residual amorphous component is finally crystallized when the temperature is further increased. This secondary crystallization happens at around 723 K. A crystalline ternary compound which contains Ba^{2+}, Mg^{2+}, and F^- ions with stoichiometric ratio Ba:Mg:F = 1:1:4 ($BaMgF_4$) forms. TEM BF image in Fig. 6.15b shows the morphology of the fully crystallized mixture film. STEM-HAADF image (Fig. 6.15c) as well as the EDX spectra (Fig. 6.15d) exhibit the chemical difference between the crystals. Two types of chemical ratios are present. Pure Ba crystals show bright contrast and crystals containing both Ba and Mg show dark contrast. The Mg:Ba atomic ratio differs from 1:1 which may be attributed to the strong absorption of the Mg-K X-rays which have quite a low energy of around 1.25 keV. The crystalline $BaMgF_4$ has an orthorhombic $BaZnF_4$-type structure, space group $Cmc2_1$ (no. 36), which has been reported by Gingl [89] in 1997 and which is schematically shown in Fig. 6.16. Theoretical diffraction peaks of the structure are calculated by using parameters in the report and shown by the red lines in Fig. 6.13d. The structure is proven by the good match between the calculated red lines and the additional peaks which appear after the high temperature annealing in the experimental data (red line, Fig. 6.13d). Figure 6.17 shows a HRTEM image of a $BaMgF_4$ crystal along [103] direction. The inset shows a simulated image and the structure used for the simulation. The good matching between the HRTEM image and the simulation further proves the $BaZnF_4$-type structure. The structure consists of MgF_6 octahedra similar as in rutile-type MgF_2, but more distorted. The MgF_6 octahedra are linked via vertices forming zigzag chains which are parallel to each other. The Ba^{2+} ions occupy the sites between chains and have nine F^- neighbours. The Mg–F bond distances range from 1.93 to 2.07 Å . The Ba–F bond distances range from 2.60 to 3.00 Å , and the F–F distances are in the range of 2.58 to 3.0 Å .

6.4 Discussion

The structure evolution of pure earth alkali (Mg, Ca, Sr, Ba) fluoride and their mixtures (Ca+Ba and Mg+Ba) are summarized in Table. 6.1. Pure CaF_2, SrF_2, and BaF_2 show identical behaviour, namely direct crystallization from the amorphous phase to the fluorite-type phase, without any intermediate metastable phase. This shows that the small radial difference of the three cations is not enough to affect the structure evolution of CaF_2, SrF_2, and BaF_2. However, the ionic radius of Mg^{2+} is significantly smaller than the ionic radii of Ba^{2+}, Sr^{2+}, and Ca^{2+}. This is the reason why the thermodynamically stable structure of the alkaline earth fluorides have 8-fold cation-F coordination in CaF_2, SrF_2, and BaF_2, but 6-fold coordination in MgF_2 [91]. This coordination difference finally influences the phase transformation behavior of MgF_2. In the amorphous phase, the Mg^{2+} ions can occupy interstitial sites of F^- framework (F_6-octahedra) leading to adjacent MgF_6 octahedra sharing faces instead of corners (Fig. 5.8a, highlighted octahedra). This preserves the octahedral tilt (Fig. 5.8, red dashed lines) and stabilizes the metastable $CaCl_2$-type phase. The fluorite structure does not allow the big Ca^{2+}, Sr^{2+}, and Ba^{2+} ions to occupy interstitial sites of the F^- framework (F_8-hexahedra), so that there is no metastable phase.

Differing from the pure binary fluorides (CaF_2, SrF_2, BaF_2), Diverse structure evolutions were observed in the quasi-binary mixtures due to an additional second cation.

For $(Ca_{0.5}Ba_{0.5})F_2$ mixture, the amorphous sample firstly crystallizes into a solid solution phase at 643 K, which decomposes at 753 K into the pure phases CaF_2 and BaF_2. This is not shown in the known phase diagram of the CaF_2/BaF_2 system [92], as the solid solution phase is attributed to a thermodynamic metastable phase [82].

In the amorphous phase of $(Ca_{0.5}Ba_{0.5})F_2$, the different cation types have different cation–F bond lengths , i.e. the average length of Ca–F (2.31 Å) is smaller than the average length of Ba-F (2.67 Å) in the amorphous $(Ca_{0.5}Ba_{0.5})F_2$ mixture (Fig. 6.6). In order to form the solid solution phase, the average bond lengths of the Ca–F and Ba–F have to equalize, consequently the Ca–F bond lengths have to be stretched from their equilibrium points and the Ba–F bond length has to be compressed. This corresponds to a high potential energy which can only be overcome at high temperatures when the cations become mobile. The consequence is a stabilization of the amorphous phase of

Table 6.1: Summary of the structure evolution of the investigated earth alkali fluorides

	Amorphous phase	Intermediate phase (metastable)	Stable phase
MgF_2	< 458 K	458 K–653 K $CaCl_2$-type with rutile-type distortion	> 653 K rutile-type
CaF_2	< 273 K	none	> 273 K fluorite-type
SrF_2	< 273 K	none	> 273 K fluorite-type
BaF_2	< 273 K	none	> 273 K fluorite-type
$(Ca_{0.5}Ba_{0.5})F_2$	< 643 K	643 K–753 K solid solution $CaBaF_4$ (fluorite-type)	> 753 K phase-separated $BaF_2 + CaF_2$ (fluorite-type)
$(Ba_{0.7}Mg_{0.3})F_2$	< 593 K	593 K–723 K amorphous $(Ba_{0.5}Mg_{0.5})F_2$ $+ BaF_2$ (fluorite-type)	> 723 K $BaMgF_4$ (orthorhombic $BaZnF_4$-type) $+ BaF_2$ (fluorite-type)

this mixture. In the intermediate phase, i.e. the solid-solution phase, Ca^{2+} and Ba^{2+} are randomly mixed on the atomic level. Thus, the formation of this solid solution does not require long-range transport of the cations. Only local movements leading to new equilibrium positions are needed. The local rearrangement of the ions requires much less energy than the long-range transport. Therefore, during the temperature increase the solid-solution phase first appears before the two different ion types separate.

In the case of $(Mg_{0.3}Ba_{0.7})F_2$ mixture, the amorphous sample crystallizes at 593 K and forms crystalline BaF_2; further at 723 K, the ternary crystalline phase $MgBaF_4$ forms. These processes reflect the phase diagram [93].

The $(Ba_{0.7}Mg_{0.3})F_2$ mixture has more complicated situation. The difference of ionic radii between Mg^{2+} and Ba^{2+} is much larger than between Ca^{2+} and Ba^{2+}. Moreover, differing from 8-fold-coordinated Ba^{2+} ions, Mg^{2+} ions prefer 6-fold coordination as their smaller radii. Therefore, formation of solid solution $Ba_7Mg_3F_{20}$ is difficult and requires much higher energy than Mg^{2+} ion transport. Thus, the $(Ba_{0.7}Mg_{0.3})F_2$ mixture shows component separation, i.e. BaF_2 separates from the amorphous matrix after the first crystallization. Then Ba-rich regions form for BaF_2 nanocrystallites, leaving amorphous regions with a ratio of Mg : Ba = 1 : 1. The amorphous residual is thus able to form crystalline $BaMgF_4$ when the temperature is further increased.

6.5 Conclusion

In this work, the structure evolution of the alkaline earth fluorides: CaF_2, SrF_2, and BaF_2 and their mixtures in the case of $(Ca_{0.5}Ba_{0.5})F_2$ and $(Ba_{0.7}Mg_{0.3})F_2$ is investigated. Their phases occurred during the annealing processes were studied. The influences by cation ionic radii and of the addition of a second cation in the fluoride systems are revealed by this study. Diverse structure evolutions were observed in the quasi-binary mixtures. Moreover, differing from MgF_2, the amorphous CaF_2, SrF_2, and BaF_2 directly transform into thermodynamically stable crystalline phases rather than going through a metastable phase.

7 Multiple-scattering correction

7.1 Log-ratio deconvolution for multiple-scattering correction

Dynamic scattering is a significant effect when the specimen is thick or the kinetic energy of the electron beam is low (120 keV in the Zeiss 912). It causes multiple-scattering which cannot be simply treated by the kinematic scattering theory. In diffraction, multiple scattering causes the experimental intensity to be much higher than the theoretical one at large angle. This results in a deviation of the experimental PDF from the true PDF. Therefore, quantitative analysis of the PDF from the experimental data is hindered by these multiple-scattering effects, especially if coordination numbers are of interest.

One way to consider multiple-scattering is to treat the distribution of the twice scattered electrons as a 2D convolution of the single scattering with itself, i.e. assuming that the second scattering has the same angular distribution as the first one. Hence, k-times scattering is a k-times convolution of the single scattering with itself, and the intensity decreases with increasing number of scattering events, according to the Poisson distribution.

$$I_k = I_{total}\frac{1}{k!}L^k e^{-L} \tag{7.1}$$

$$P_k(\vec{q}) = [P_1(\vec{q}) \otimes P_1(\vec{q}) \otimes \cdots \otimes P_1(\vec{q})]_{k-times} \tag{7.2}$$

where $L = D/\lambda$ is the ratio of specimen thickness (D) and elastic scattering mean free path (λ), $q = 2sin\theta/\lambda$ is the scattering angle, I_1 is the intensity of single scattered electrons, and $P_1(\vec{q})$ is the normalized single-scattering distribution, I_k is the intensity of k-times scattered electrons, $P_k(\vec{q})$ is the normalized distribution of the k-times scattered electrons. A Fourier-log deconvolution method is adopted to retrieve the single-scattering

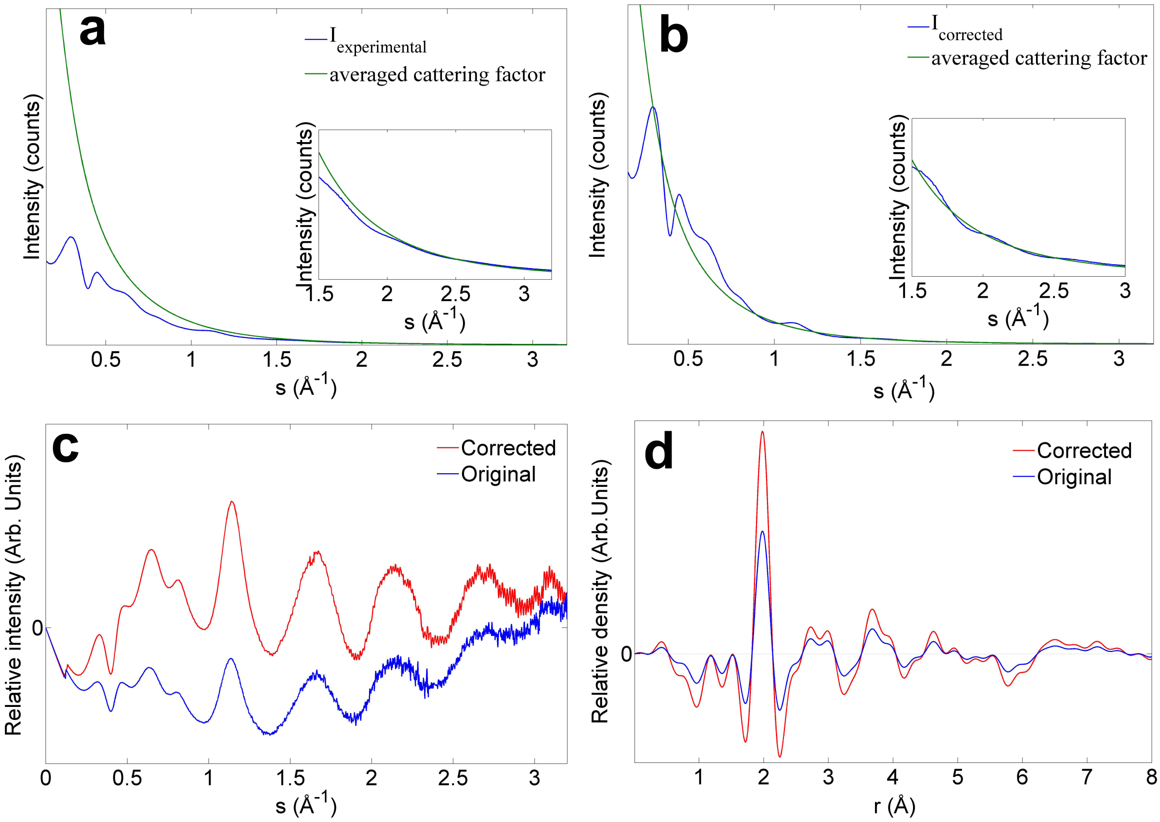

Figure 7.1: Illustration of multiple-scattering correction by Fourier-log deconvolution with the experimental data of the 80 nm thick MgF_2 amorphous specimen. (a) Experimental diffraction profile (blue) and the average scattering factor (green), the insert is enlarged part of the large angle range. (b) Corrected diffraction profile (blue) and the average scattering factor (green), the insert is enlarged part of the large angle range. (c) The structure factors from the experiment (blue) and from the correction (red). (d) PDFs from the experiment (blue) and from the correction (red).

intensity (I_1) and its distribution ($P_1(\vec{q})$). A more detailed description is shown in G.R. Anstis's work [62] and J.E. Ankele' work [63].

Table 7.1: List of the average 1^{st} shell coordination numbers

1^{st} coordination shell	uncorrected	corrected	MD	perfect crystal
Amorphous MgF_2	2.7	3.1	3.4	–
$CaCl_2$-type MgF_2	3.1	3.9	–	4.0
Rutile-type MgF_2	3.1	3.5	3.8	4.0
Bunsenite-type NiO	3.7	11.7	–	6

The thicknesses D are taken as $D_{\mathrm{MgF_2}} = 80$ nm, and $D_{\mathrm{NiO}} = 35$ nm.

After multiple-scattering correction the diffraction line profile can be fitted by the theoretical scattering factor in the whole angular range unlike the originally uncorrected data where fitting at both small and large angles is impossible (Fig. 7.1a, b). The scattering factor of the corrected data thus oscillates around zero (Fig. 7.1c). The resulting PDF of the corrected data has larger peak intensities than the uncorrected counterpart (Fig. 7.1d). The coordination numbers which are the integral intensities below the PDF peaks are increased accordingly. Note that the correction has the same effect as the polynomial fitting used in the data processing discussed in section 3.4 (Fig. 3.6b, d). This similarity is strong evidence that multiple-scattering is the main reason for the deviation of the experimental diffraction data from the theoretical scattering factor.

This method is applied to MgF_2 data to try achieving the Mg–F coordination numbers without influence of the multiple-scattering effect. The parameter of the specimen thickness D can be measured by EELS. The elastic mean free path λ can be calculated by following the equation: $\lambda = 1/(\rho \times \sigma)$, where ρ is the atomic density of the specimen, and σ is the elastic scattering cross-section of the corresponding atoms which can be found in [94]. Table 7.1 shows the first shell coordination numbers of the MgF_2 sample ($D = 80$ nm) for the three different phases and a crystalline NiO sample ($D = 35$ nm). The numbers obtained for MgF_2 are very close to the MD simulation data. However, the results for the crystalline NiO film are far from the expected value of 6. The original and corrected diffraction profiles of the NiO film are shown in Fig. 7.2. Negative

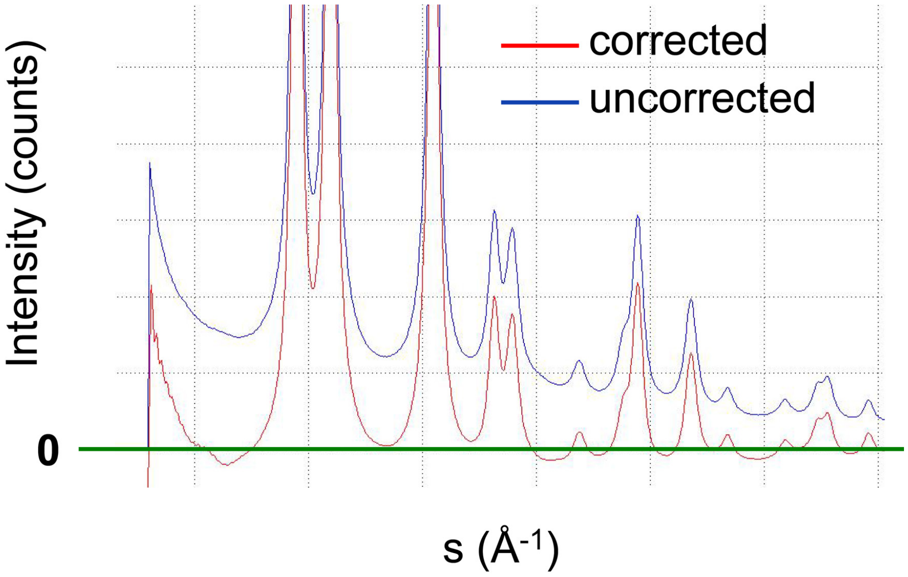

Figure 7.2: Illustration of the failure of the Fourier-log deconvolution in crystalline NiO. Lines are diffraction profiles. The zero intensity line is highlighted by the green line.

intensity occurs in the corrected profile. This causes too much integrated intensities of the PDF peaks, resulting in an unreasonably large coordination number. This degrades the reliability of the coordination numbers obtained for the rutile-type phase and $CaCl_2$-type phase and even the amorphous phase MgF_2.

The reason of the failure of the Fourier-log deconvolution in the crystalline sample is that the method includes three basic approximation:

1. Transmitted beam has the same intensity as the incident beam, i.e. electron absorption and back scattering are not taken into account.
2. Unique elastic mean free path λ, i.e. the same intensity drop for each scattering event.
3. Same angular distribution in all scattering events.

The first two approximations assume that the Poisson distribution of the scattering intensity (Eq. 7.1) is correct. The third approximation means that the sample is treated as a fully isotropic structure everywhere (Eq 7.2). It ignores local structure fluctuations of the sample and causes failure in polycrystalline material. Even in the amorphous material, the local anisotropic structure cannot be neglected due to their non-zero structure factors and situations can be even worse when the material contains local crystalline structures.

.

7.2 Structure reconstruction from experimental PDF assisted by dynamic simulation

To achieve real multiple-scattering-free diffraction data, the dynamic scattering process has to be considered in a forward way instead of mathematical deconvolution. The forward way means taking the multiple-scattering into account by applying a dynamic process to a structure model to simulate the diffraction pattern which then contains multiple-scattering effects. A reasonable structural model including all atom positions thus becomes the key point. There are basically two ways to find a reasonable model. One is to consider all forces between atoms then relaxing the model from an initial state until equilibrium, such as in molecular dynamics (MD). Another is to retrieve the structure model by comparing simulated data with real experiments, then go back to change the model until the simulation fits to the experiments. According to the aim of fixing the multiple-scattering problem, a method to retrieve the model by based on the latter approach will be introduced.

7.2.1 The basic: Reverse Monte-Carlo (RMC)

Reverse Monte-Carlo, based on a random walking algorithm, has been a routine to retrieve structure models by comparing experimental data with values derived from the model [65–68]. Figure 7.3 shows the basic RMC algorithm in the model simulation:

1. Select a starting structure model.
2. Extract the PDF from the pseudo-model, $G_{\text{model}}(r)$.

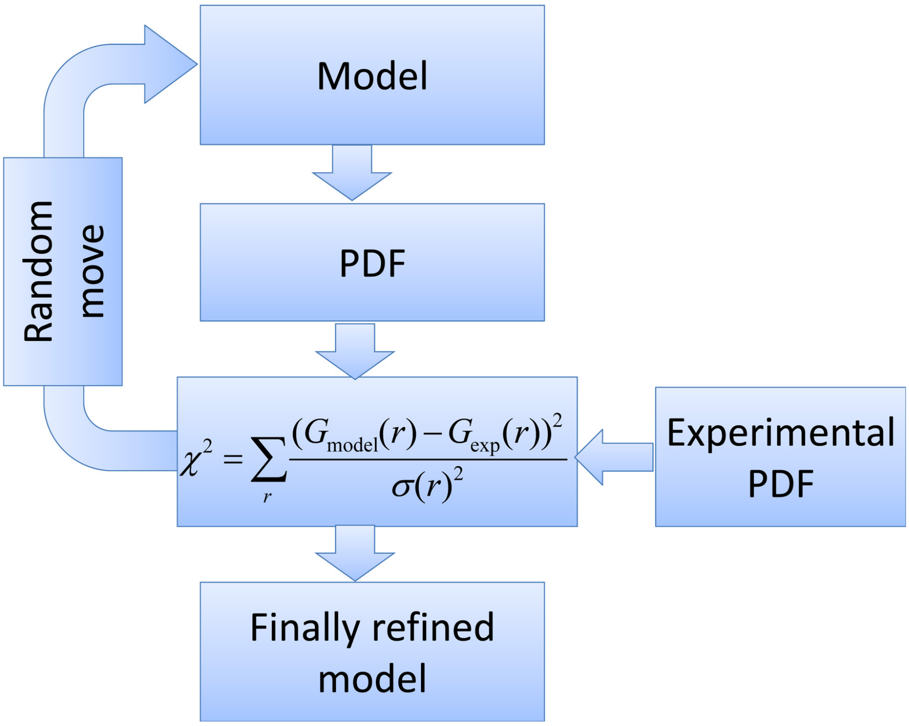

Figure 7.3: Flow chart of the RMC algorithm.

3. Calculate the deviation of $G_{\mathrm{model}}(r)$ from the experimental PDF:

$$\chi_0^2 = \sum_r \frac{(G_{\mathrm{model}}(r) - G_{\mathrm{exp}}(r))^2}{\sigma^2(r)} \tag{7.3}$$

   where $G_{\mathrm{exp}}(r)$ is the experimental PDF, $\sigma(r)$ relates to the experimental error.

4. Randomly move atoms in the structure model (usually with a uniform distance).
5. Calculate the new model's PDF and its difference from the experimental PDF, χ_n^2 by Eq. 7.3.
6. If $\chi_n^2 < \chi_0^2$, accept the movement in step 4 and replace the structure model by the new model, and replace χ_0^2 by χ_n^2, otherwise reject the structural changes and stop.
7. Return to step 4.

With numerous iterations, χ_0^2 will decrease to a minimum (in the best case a global minimum which partially depends on the strength of the moving step in step 4) and the new model's PDF will come closer to the experimental data. Then the refined model can be judged as a reasonable model for the experimental data. One drawback is that the iterative efficiency of this algorithm is low owing to the random movement of the model's atoms (in step 4), i.e. no direction can be predetermined. Moreover, some restrictions of the movements are set in order to keep the simulated model physical reasonable. These restrictions can strongly reduce the efficiency of the random movements.

7.2.2 Dynamic diffraction simulation combined with RMC

The experimental PDF is not multiple-scattering-free so that the simulated model based on that can be wrong. Our new method adopts the basic RMC algorithm and simultaneously takes the dynamic scattering process into account to reconstruct a more reasonable model as well as its multiple-scattering-free PDF. The aim of this new development is to overcome the multiple-scattering problem. The flow chart of the basic idea is given below:

1. Produce an initial PDF (element-specific PDFs for multi-element materials). The simplest case is to use the PDFs of crystalline structure of the material.
2. Build an initial structure model fitting to the pseudo-PDF by RMC.
3. Construct a supercell to simulate the thickness of the sample like in the real measurement.
4. Calculate a diffraction pattern by a dynamical calculation using a multislice code [90].
5. Calculate the PDF from the simulated diffraction pattern.
6. Compare the simulated PDF with the experimental PDF. Accept the initial PDF as well as the initial structure model if the difference is small enough, otherwise change the initial PDF in step 1 and repeat until a satisfying difference value is obtained.

The method proposed here is a promising approach to overcome the problems resulted from the dynamic scattering which has puzzled electron microscopists for decades. This

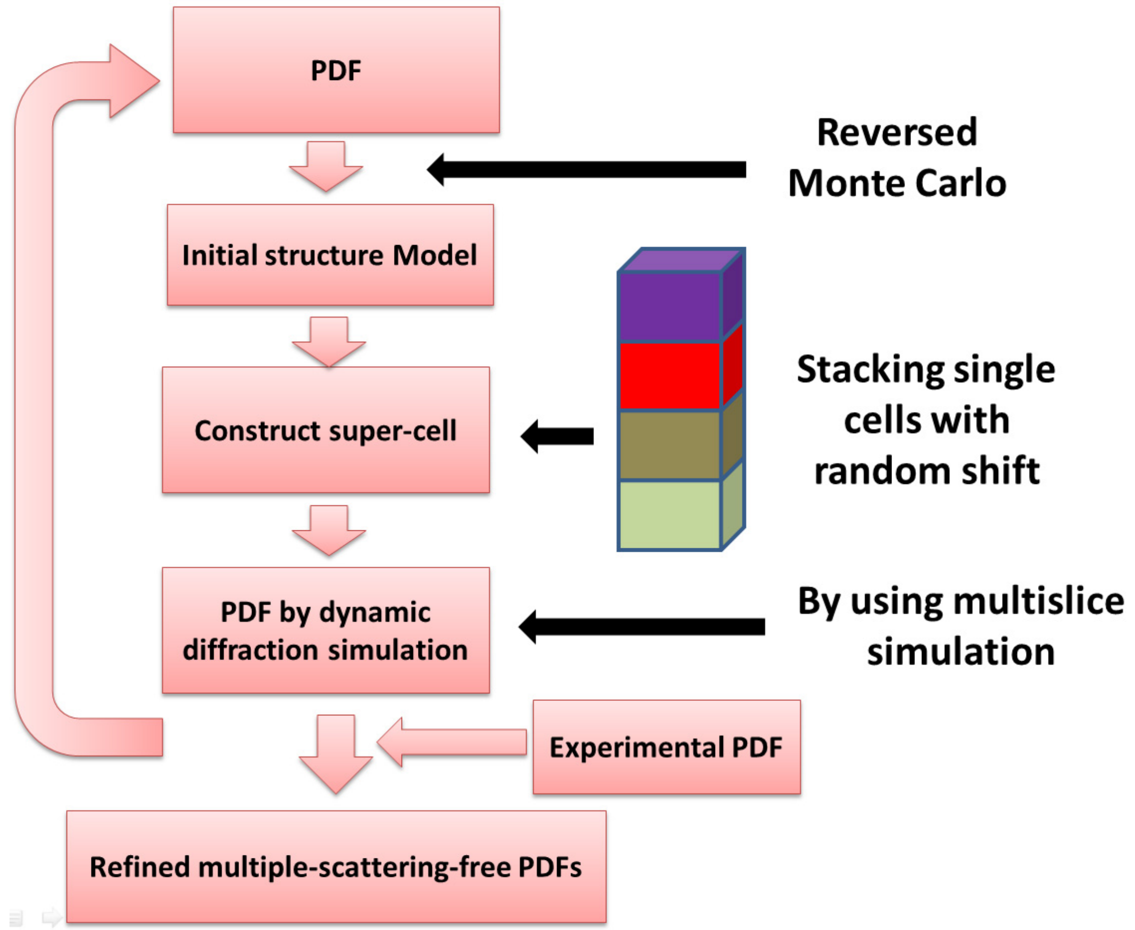

Figure 7.4: Flow chart of the proposed algorithm to take the dynamic process into account.

possible solution, which only requires one single diffraction experiment, but outputs a model and element-specific partial PDFs, has promising perspectives for experimental microscopists.

8 Outlook and conclusion

8.1 Outlook

8.1.1 Element-specific partial PDFs from experiments

The PDF based on a single diffraction experiment only can derive the element-averaged total PDF. In the investigation of multi-element matter the information of element-specific coordination is of interest, however, the total PDF cannot give this informations, when the element-specific partial PDFs overlap. Therefore, methods to experimentally reveal the element-specific partial PDFs are desired in future studies.

One way is to combine electron diffraction data with techniques using other diffraction sources which have different scattering factors than electrons, for example X-ray and neutron radiation. From the three different radiation sources, three different PDFs can be obtained. Then the element-specific partial PDFs can be extracted. However, this method can only deal with binary matter as the binary matter contains three partial PDFs. For ternary matters which have six partial PDFs, six different diffraction data from additional three sources would be necessary. This is obviously impossible. Furthermore access to X-ray synchrotron or neutron sources is not as easy as clicking a button for the diffraction mode in a TEM.

Another way is to analyse the extended fine structure of EELS data (EXELFS) which is the part of the spectrum from 30–50 eV past the onset until several hundreds of eV. The oscillations of the EXELFS contain element-specific information of the structure of the measured specimen. The partial PDFs can thus be gained from the EELS core-loss spectra of different elements. This technique have been studied [95–98] and a brief introduction can be found in Williams' book [58] (chapter 40). The technique based on the same principle has been routine in the extended X-ray absorption fine structure

(EXAFS) [38, 39]. One problem on the EELS side is that EXELFS does not have as good signal-to-noise ratio as EXAFS. Higher illuminating dose and longer acquisition time can modify the structure of some materials due to the stronger interaction of electrons compared to X-ray. However, it is worth testing such techniques in the future for some more stable materials than the mixtures presented in chapter 6.

8.1.2 Other techniques for amorphous material characterization

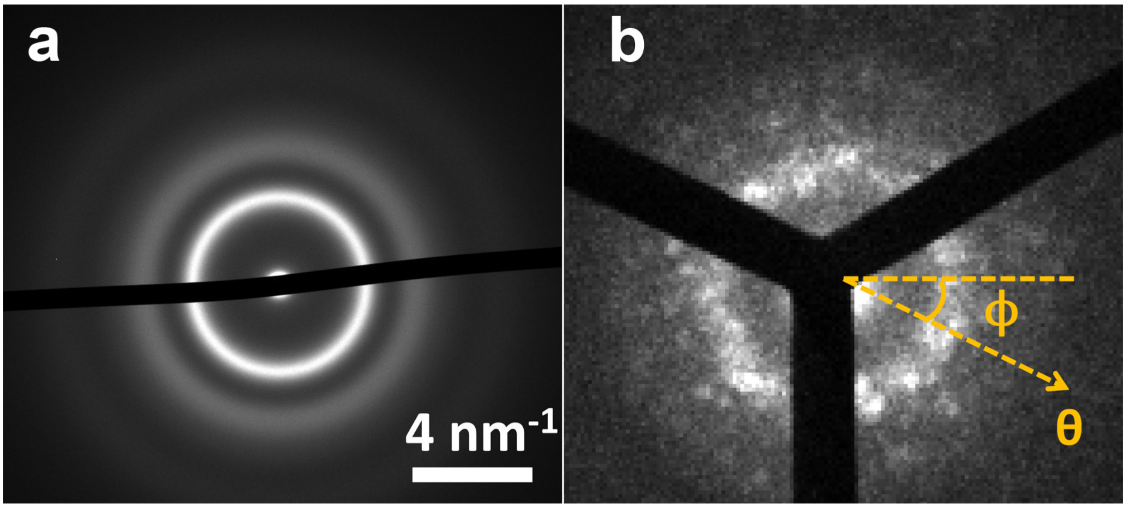

Figure 8.1: Diffraction patterns of the $(Ba_{0.7}Mg_{0.3})F_2$ film obtain by (a) large-area parallel illumination (Zeiss EM912, 1.2 μm diameter selected area aperture) and (b) nanobeam illumination (SESAM, 1.9 nm beam diameter, 76 mrad convergence angle).

Figure 8.1 shows the difference between the traditional diffraction pattern by large-area illumination ((a), obtained in the Zeiss EM912 with select area aperture of 1.2 μm diameter) and a nanobeam diffraction pattern using a nearly parallel beam illumination ((b), obtained in the SESAM with illumination condition of 1.9 nm beam-diameter and 0.76 mrad convergence angle, following the microscope configuration described in [99]). The material is the amorphous $(Ba_{0.7}Mg_{0.3})F_2$ film presented in Section 6.3. The PDF technique based on large-area diffraction offers an averaged information spanning a large volume of the investigated sample (micrometers). However, nanobeam illumination is spatially coherent and illuminates a much smaller volume of the specimen. Therefore the diffraction data contain more details in both scattering angle (Fig. 8.1b, represented by the length of the orange arrowed dashed line, denoted as θ) and the azimuthal orientation in the second dimension (Fig. 8.1b, represented by the azimuthal angle between the orange arrowed dashed line and the non-arrowed dashed line, denoted as ϕ).

The θ value of the speckles in Fig. 8.1 contains information from the local area (with diameter of a few nm). More fluctuation in a diffraction series record at different positions of a specimen represents more established medium-range ordering, therefore, it is an effective mean to detect "para-crystallites" hidden inside amorphous materials. The technique called "fluctuation microscopy" is designed basing on such principle [100–104].

Another technique is called (angular) cross-correlation analysis which focuses on the second dimension information, i.e. the ϕ value (Fig. 8.1b). The azimuthal arrangement of the speckles in the nanobeam diffraction pattern relates to the local symmetry of the paracrystallites and their orientations. By analysing the ϕ-dependent correlation coefficient of those speckles one can reveal the symmetric arrangement of atoms in the specimen and hence the bonding angles and coordination numbers. Such a technique has been utilized in X-ray synchrotron diffraction and was applied to investigate colloidal glasses [105].

8.2 Conclusion

In this work, the disordered structures in the amorphous phases and distortions in the crystalline high-temperature phases of the investigated materials were studied by the PDF technique. In combination with XRD and MD, the $CaCl_2$-type crystallization nuclei were found in the amorphous MgF_2 deposit. Moreover, amorphous intergranular regions in the annealed MgF_2 specimen were detected. This successfully explains the discrepancy between the existence of the $CaCl_2$-type metastable phase and the theoretical prediction, and hence shows a thorough understanding of the structure evolution through the metastable phase.

The height of peaks in the PDF contains coordination information. The coordination number can be extracted from the peaks, although it is not straightforward due to multiple scattering. The relative height of the peaks in the PDF still gives an intuitive view of the short-range ordering of the investigated materials. With PDF the information is translated into real space instead of the ambiguous diffuse scattering in the reciprocal space, thus, can be directly read out without complicated theoretical simulations. Based on this, the amorphous phase of other alkaline earth fluorides and their mixtures were investigated by the experimental PDFs.

Although the two methods introduced in section 8.1 are powerful, the traditional PDF measurement from simple diffraction experiment is the most convenient and preferred route and offers strong feasibility for beam-sensitive materials. It offers material scientists and microscopists a straightforward way to explain diffuse scattering, hence to get access into disordered structures. By combining the proposed multiple-scattering correction method (chapter 7.2.2), the traditional PDF measurements based on electron diffraction can be more powerful and reliable for complex materials.

List of Figures

Bibliography

[1] F. J. DiSalvo: *Solid-State Chemistry - a Rediscovered Chemical Frontier*. Science **247**, 649-655 (1990).

[2] A. K. Cheetham: *Advanced Inorganic Materials - an Open Horizon*. Science **264**, 794-795 (1994).

[3] F. J. DiSalvo: *Solid state chemistry*. Solid State Communications **102**, 79-85 (1997).

[4] F. J. DiSalvo: *Challenges and opportunities in solid-state chemistry*. Pure and Applied Chemistry **72**, 1799-1807 (2000).

[5] J. C. Schön and M. Jansen: *First step towards planning of syntheses in solid-state chemistry: Determination of promising structure candidates by global optimization*. Angewandte Chemie International Edition in English **35**, 1287-1304 (1996).

[6] M. Jansen: *A concept for synthesis planning in solid-state chemistry*. Angewandte Chemie International Edition in English **41**, 3747-3766 (2002).

[7] M. Jansen, K. Doll and J. C. Schön: *Addressing chemical diversity by employing the energy landscape concept*. Acta Crystallographica Section A **66**, 518-534 (2010).

[8] J. C. Schön, H. Putz and M. Jansen: *Studying the energy hypersurface of continuous systems - The threshold algorithm*. Journal of Physics: Condensed Matter **8**, 143-156 (1996).

[9] J. C. Schön, K. Doll and M. Jansen: *Predicting solid compounds via global exploration of the energy landscape of solids on the ab initio level without recourse to experimental information*. Physica Status Solidi (b) **247**, 23-39 (2010).

[10] K. Doll, J. C. Schön and M. Jansen: *Global exploration of the energy landscape of solids on the ab initio level.* Physical Chemistry Chemical Physics **9**, 6128-6133 (2007).

[11] N. Gaston, B. Paulus, U. Wedig and M. Jansen: *Multiple minima on the energy landscape of elemental zinc: A wave function based ab initio study.* Physical Review Letters **100**, 226404 (2008).

[12] J. C. Schön, M. A. C. Wevers and M. Jansen: *'Entropically' stabilized region on the energy landscape of an ionic solid.* Journal of Physics: Condensed Matter **15**, 5479-5486 (2003).

[13] M. A. C. Wevers, J. C. Schön and M. Jansen: *Global aspects of the energy landscape of metastable crystal structures in ionic compounds.* Journal of Physics: Condensed Matter **11**, 6487-6499 (1999).

[14] D. Fischer and M. Jansen: *Low-activation solid-state syntheses by reducing transport lengths to atomic scales as demonstrated by case studies on AgNO3 and AgO.* Journal of the American Chemical Society **124**, 3488-3489 (2002).

[15] J. C. Schön and M. Jansen: *Determination, prediction, and understanding of structures, using the energy landscapes of chemical systems - Part I.* Zeitschrift für Kristallographie - Crystalline Materials **216**, 307-325 (2001).

[16] J. C. Schön and M. Jansen: *Determination, prediction, and understanding of structures, using the energy landscapes of chemical systems - Part III.* Zeitschrift für Kristallographie **216**, 361-383 (2001).

[17] J. C. Schön and M. Jansen: *Prediction, determination and validation of phase diagrams via the global study of energy landscapes.* International Journal of Materials Research **100**, 135-152 (2009).

[18] M. Jansen, I. V. Pentin and J. C. Schön: *A Universal Representation of the States of Chemical Matter Including Metastable Configurations in Phase Diagrams.* Angewandte Chemie International Edition in English **51**, 132-135 (2012).

[19] I. V. Pentin, V. Saltykov, J. Nuss, J. C. Schön and M. Jansen: *Theoretical and Experimental Exploration of the Energy Landscape of the Quasi-Binary Cesium Chloride/Lithium Chloride System.* Chemistry – A European Journal **18**, 3559-3565 (2012).

[20] Z. P. Cancarevic, J. C. Schön, D. Fischer and M. Jansen: *Theoretical and experimental exploration of the energy landscape of LiI.* Materials Science Forum **494**, 61-66 (2005).

[21] D. Fischer and M. Jansen: *A new modification of the laves phase* $CaLi_2$. Zeitschrift für anorganische und allgemeine Chemie **629**, 1934-1936 (2003).

[22] D. Fischer and M. Jansen: *Synthesis and Crystal Structure of* $LiZn_{13}$. Zeitschrift für anorganische und allgemeine Chemie **636**, 1917-1919 (2010).

[23] D. Fischer and M. Jansen: *Synthesis and structure of* Na_3N. Angewandte Chemie International Edition in English **41**, 1755-1756 (2002).

[24] D. Fischer, Z. Cancarevic, J. C. Schön and M. Jansen: *Synthesis and structure of* K_3N. Zeitschrift für anorganische und allgemeine Chemie **630**, 156-160 (2004).

[25] D. Fischer, A. Muller and M. Jansen: *Is there a wurtzite-modification of lithium bromide? Studies on the system LiBr/LiI.* Zeitschrift für anorganische und allgemeine Chemie **630**, 2697-2700 (2004).

[26] A. Bach, D. Fischer and M. Jansen: *Synthesis of a New Modification of Lithium Chloride Confirming Theoretical Predictions.* Zeitschrift für anorganische und allgemeine Chemie **635**, 2406-2409 (2009).

[27] Y. Liebold-Ribeiro, D. Fischer and M. Jansen: *Experimental substantiation of the "Energy Landscape Concept" for solids: Synthesis of a new modification of LiBr.* Angewandte Chemie International Edition in English **47**, 4428-4431 (2008).

[28] A. Bach, D. Fischer, X. K. Mu, W. Sigle, P. A. van Aken and M. Jansen: *Structural Evolution of Magnesium Difluoride: from an Amorphous Deposit to a New Polymorph.* Inorganic Chemistry **50**, 1563-1569 (2011).

[29] S. Neelamraju, A. Bach, D. Fischer, J. C. Schön and M Jansen: *Experimental and theoretical study on Raman spectra of magnesium fluoride clusters and solids.* The Journal of Chemical Physics **137**, 194319 (2012).

[30] http://www.elementsdatabase.com/, (last visited on 12, April, 2013).

[31] C. T. Koch and S. H. Garofalini: *Determining the radial pair-distribution function within intergranular amorphous films by numerical nanodiffraction.* Ultramicroscopy **106**, 383-388 (2006).

[32] R. B. Neder and Th. Proffen: *Diffuse scattering and defect structure simulations : a cook book using the program DISCUS.* Oxford University Press, Oxford (2008).

[33] T. Egami and S. J. L. Billinge: *Underneath the Bragg peaks structural analysis of complex materials.* Elsevier Ltd, Kidlington, Oxford OX5 1GB, UK (2003).

[34] P. Chirawatkul, A. Zeidler, P. S. Salmon, S. Takeda, Y. Kawakita, T. Usuki and H. E. Fischer: *Structure of eutectic liquids in the Au-Si, Au-Ge, and Ag-Ge binary systems by neutron diffraction.* Physical Review B **83**, 014203 (2011).

[35] J. Fortner and J. S. Lannin: *Radial-Distribution Functions of Amorphous-Silicon.* Physical Review B **39**, 5527-5530 (1989).

[36] Th. Proffen, S. J. L. Billinge, T. Egami and D. Louca: *Structural analysis of complex materials using the atomic pair distribution function - a practical guide.* Zeitschrift für Kristallographie **218**, 132-143 (2003).

[37] B. H. Toby and T. Egami: *Accuracy of pair distribution function analysis applied to crystalline and non-crystalline materials.* Acta Crystallographica Section A **48**, 336-346 (1992).

[38] T. Ressler, S. L. Brock, J. Wong and S. L. Suib: *Multiple-scattering EXAFS analysis of tetraalkylammonium manganese oxide colloids.* Journal of Physical Chemistry B **103**, 6407-6420 (1999).

[39] D. E. Sayers, E. A. Stern and F. W. Lytle: *New Technique for Investigating Noncrystalline Structures: Fourier Analysis of Extended X-Ray – Absorption Fine Structure.* Physical Review Letters **27**, 1204 (1971).

[40] K. Mullen and I. Levin: *Mitigation of errors in pair distribution function analysis of nanoparticles.* Journal of Applied Crystallography **44**, 788-797 (2011).

[41] T. Egami and W. Dmowski: *Dynamic pair-density function method for neutron and X-ray inelastic scattering.* Zeitschrift für Kristallographie - Crystalline Materials **227**, 233-237 (2012).

[42] C. A. Reiss, A. Kharchenko and M. Gateshki: *On the use of laboratory X-ray diffraction equipment for Pair Distribution Function (PDF) studies.* Zeitschrift für Kristallographie - Crystalline Materials **227**, 257-261 (2012).

[43] K. Page, C. E. White, E. G. Estell, R. B. Neder, A. Llobet and Th. Proffen: *Treatment of hydrogen background in bulk and nanocrystalline neutron total scattering experiments.* Journal of Applied Crystallography **44**, 532-539 (2011).

[44] D. J. H. Cockayne and D. R. Mckenzie: *Electron-Diffraction Analysis of Polycrystalline and Amorphous Thin-Films.* Acta Crystallographica Section A **44**, 870-878 (1988).

[45] D. J. H. Cockayne: *The study of nanovolumes of amorphous materials using electron scattering.* Annual Review of Materials Research **37**, 159-187 (2007).

[46] L. E. Hall and D. R. McKenzie: *Coordination number determination in binary alloys using electron diffraction.* Philosophical Magazine A **80**, 525-541 (2000).

[47] T. C. Petersen, W. McBride, D. G. McCulloch, I. K. Snook and I. Yarovsky: *Refinements in the collection of energy filtered diffraction patterns from disordered materials.* Ultramicroscopy **103**, 275-283 (2005).

[48] W. E. McBride, D. J. H. Cockayne and C. M. Goringe: *Reduced density function analysis using convergent electron illumination and iterative blind deconvolution.* Ultramicroscopy **76**, 115-123 (1999).

[49] C. A. Young and A. L. Goodwin: *Applications of pair distribution function methods to contemporary problems in materials chemistry.* Journal of Materials Chemistry **21**, 6464-6476 (2011).

[50] D. J. Sprouster, R. Giulian, L. L. Araujo, P. Kluth, B. Johannessen, N. Kirby and M. C. Ridgway: *Formation and structural characterization of Ni nanoparticles embedded in* SiO_2. Journal of Applied Physics **109**, 113517 (2011).

[51] T. Takagi, T. Ohkubo, Y. Hirotsu, B. S. Murty, K. Hono and D. Shindo: *Local structure of amorphous* $Zr_{70}Pd_{30}$ *alloy studied by electron diffraction.* Applied Physics Letters **79**, 485-487 (2001).

[52] D. Dambournet, K. W. Chapman, M. V. Koudriachova, P. J. Chupas, I. Belharouak and K. Amine: *Combining the Pair Distribution Function and Computational Methods To Understand Lithium Insertion in Brookite (*TiO_2*).* Inorganic Chemistry **50**, 5855-5860 (2011).

[53] C. Li, X. Mu, P. A. van Aken and J. Maier: *A High-Capacity Cathode for Lithium Batteries Consisting of Porous Microspheres of Highly Amorphized Iron Fluoride Densified from Its Open Parent Phase.* Advanced Energy Materials **3**, 113-119 (2013).

[54] N. Yamakawa, M. Jiang, B. Key and C. P. Grey: *Identifying the Local Structures Formed during Lithiation of the Conversion Material, Iron Fluoride, in a Li Ion Battery: A Solid-State NMR, X-ray Diffraction, and Pair Distribution Function Analysis Study.* Journal of the American Chemical Society **131**, 10525-10536 (2009).

[55] D. Dambournet, K. W. Chapman, P. J. Chupas, R. E. Gerald, N. Penin, C. Labrugere, A. Demourgues, A. Tressaud and K. Amine: *Dual Lithium Insertion and Conversion Mechanisms in a Titanium-Based Mixed-Anion Nanocomposite.* Journal of the American Chemical Society **133**, 13240-13243 (2011).

[56] A. Abouimrane, D. Dambournet, K. W. Chapman, P. J. Chupas, W. Weng and K. Amine: *A New Class of Lithium and Sodium Rechargeable Batteries Based on Selenium and Selenium-Sulfur as a Positive Electrode.* Journal of the American Chemical Society **134**, 4505-4508 (2012).

[57] L. Malavasi: *Total scattering investigation of materials for clean energy applications: The importance of the local structure.* Dalton Transactions **40**, 3777-3788 (2011).

[58] D. B. Williams and C. B. Carter: *Transmission electron microscopy : a textbook for materials science.* Springer, New York (2008).

[59] L. Reimer and H. Kohl: *Transmission Electron Microscopy: Physics of Image Formation.* Springer, Berlin (1993).

[60] Zeiss: *Transmission Electron Microscope LEO 912 OMEGA Operating Manual.* LEO Elektronenmikroskopie GmbH, Oberkochen (1998).

[61] E. J. Kirkland: *Advanced computing in electron microscopy.* Plenum Press, New York (1998).

[62] G. R. Anstis, Z. Liu and M. Lake: *Investigation of Amorphous Materials by Electron-Diffraction – the Effects of Multiple-Scattering.* Ultramicroscopy **26**, 65-69 (1988).

[63] J. E. Ankele, J. Mayer, P. Lamparter and S. Steeb: *Quantitative electron diffraction data of amorphous materials.* Zeitschrift für Naturforschung Section A **60**, 459-468 (2005).

[64] G. Q. Li, K. B. Borisenko, Y. X. Chen, D. Nguyen-Manh, E. Ma and D. J. H. Cockayne: *Local structure variations in $Al_{89}La_6Ni_5$ metallic glass.* Acta Materialia **57**, 804-811 (2009).

[65] R. L. McGreevy: *Reverse Monte Carlo modelling.* Journal of Physics: Condensed Matter **13**, R877-R913 (2001).

[66] M. M. J. Treacy and K. B. Borisenko: *The Local Structure of Amorphous Silicon.* Science **335**, 950-953 (2012).

[67] K. B. Borisenko, B. Haberl, A. C. Y. Liu, Y. X. Chen, G. Q., J. S. Williams, J. E. Bradby, D. J. H. Cockayne and M. M. J. Treacy: *Medium-range order in amorphous silicon investigated by constrained structural relaxation of two-body and four-body electron diffraction data.* Acta Materialia **60**, 359-375 (2012).

[68] D. J. H. Cockayne, D. R. McKenzie, W. McBride, C. Goringe and D. McCulloch: *Characterization of amorphous materials by electron diffraction and atomistic modeling.* Microscopy and Microanalysis **6**, 329-334 (2000).

[69] D. G. McCulloch, D. R. McKenzie, C. M. Goringe, D. J. H. Cockayne, W. McBride and D. C. Green: *Experimental and theoretical characterization of structure in thin disordered films.* Acta Crystallographica Section A **55**, 178-187 (1999).

[70] K. B. Borisenko, Y. X. Chen, D. J. H. Cockayne, S. A. Song and H. S. Jeong: *Understanding atomic structures of amorphous C-doped $Ge_2Sb_2Te_5$ phase-change memory materials.* Acta Materialia **59**, 4335-4342 (2011).

[71] C. Bennemann, W. Paul, K. Binder and B. Dunweg: *Molecular-dynamics simulations of the thermal glass transition in polymer melts: alpha-relaxation behavior.* Physical Review E **57**, 843-851 (1998).

[72] W. Kob: *Computer simulations of supercooled liquids and glasses.* Journal of Physics: Condensed Matter **11**, R85-R115 (1999).

[73] H. Pang, Z. H. Jin and K. Lu: *Relaxation, nucleation, and glass transition in supercooled liquid Cu.* Physical Review B **67**, 094113 (2003).

[74] K. Binder: *Computer simulations of undercooled fluids and the glass transition.* Journal of Non-Crystalline Solids **274**, 332-341 (2000).

[75] C. T. Koch, W. Sigle, R. Höschen, M. Rühle, E. Essers, G. Benner and M. Matijevic: *SESAM: Exploring the Frontiers of Electron Microscopy.* Microscopy and Microanalysis **12**, 506-514 (2006).

[76] N. Totò, C. Schön and M. Jansen: *Atomistic study of xenon crystal growth via low-temperature atom beam deposition.* Physical Review B **82**, 115401 (2010).

[77] M. Catti, A. Pavese, R. Dovesi, C. Roetti and M. Causa: *Quantum-Mechanical Hartree-Fock Self-Consistent-Field Study of the Elastic-Constants and Chemical Bonding of MgF_2 (Sellaite).* Physical Review B **44**, 3509-3517 (1991).

[78] S. Neelamraju, J. C. Schön, K. Doll and M. Jansen: *Ab initio and empirical energy landscapes of $(MgF_2)_n$ clusters ($n = 3, 4$).* Physical Chemistry Chemical Physics **14**, 1223-1234 (2012).

[79] M. A. C. Wevers, J. C. Schön and M. Jansen: *Determination of structure candidates of simple crystalline AB_2 systems.* Journal of Solid State Chemistry **136**, 233-246 (1998).

[80] J. Haines, J. M. Léger, F. Gorelli, D. D. Klug, J. S. Tse and Z. Q. Li: *X-ray diffraction and theoretical studies of the high-pressure structures and phase transitions in magnesium fluoride.* Physical Review B **64**, 134110 (2001).

[81] A. Duvel, B. Ruprecht, P. Heitjans and M. Wilkening: *Mixed Alkaline-Earth Effect in the Metastable Anion Conductor $Ba_{1-x}Ca_xF_2$ ($0 \leq x \leq 1$): Correlating Long-Range Ion Transport with Local Structures Revealed by Ultrafast F-19 MAS NMR.* Journal of Physical Chemistry C **115**, 23784-23789 (2011).

[82] B. Ruprecht, M. Wilkening, A. Feldhoff, S. Steuernagel and P. Heitjans: *High anion conductivity in a ternary non-equilibrium phase of BaF_2 and CaF_2 with mixed cations.* Physical Chemistry Chemical Physics **11**, 3071-3081 (2009).

[83] B. Ruprecht, M. Wilkening, S. Steuernagel and P. Heitjans: *Anion diffusivity in highly conductive nanocrystalline BaF_2:CaF_2 composites prepared by high-energy ball milling.* Journal of Materials Chemistry **18**, 5412-5416 (2008).

[84] A. H. Swanson and E. Tatge: *Standard X-ray diffraction powder patterns.* National Bureau of Standards **539**, 69-70 (1953).

[85] A. H. Swanson and E. Tatge: *Standard X-ray diffraction powder patterns.* National Bureau of Standards **539**, 1-95 (1953).

[86] Y. Gao, T. Tiedje, P. C. Wong and K. A. R. Mitchell: *X-Ray-Absorption near-Edge Structure at the Fluorine-K Edge in CaF_2 and BaF_2.* Physical Review B **48**, 15578-15583 (1993).

[87] J. J. Rehr, J. J. Kas, M. P. Prange, A. P. Sorini, Y. Takimoto and F. Vila: *Ab initio theory and calculations of X-ray spectra.* Comptes Rendus Physique **10**, 548-559 (2009).

[88] http://leonardo.phys.washington.edu/feff/, (last visited on 12, April, 2013).

[89] F. Gingl: *$BaMgF_4$ and $Ba_2Mg_3F_{10}$: New examples for structural relationships between hydrides and fluorides.* Zeitschrift für anorganische und allgemeine Chemie **623**, 705-709 (1997).

[90] T. C. Koch: *Determination of core structure periodicity and point defect density along dislocations.* Phd Dessertation (2002).

[91] Ulrich Müller: *Inorganic Structural Chemistry.* John Wiley and Sons, Ltd, (2007).

[92] P. P. Fedorov, I. I. Buchinskaya, N. A. Ivanovskaya, V. V. Konovalova, S. V. Lavrishchev and B. P. Sobolev: *CaF_2-BaF_2 phase diagram.* Doklady Physical Chemistry **401**, 53-55 (2005).

[93] M. Rolin and M. Clausier: *Le Systeme Fluorure De Calcium Fluorure De Baryum - Fluorure De Magnesium.* Revue Internationale Des Hautes Temperatures Et Des Refractaires **4**, 39 (1967).

[94] C. J.; Biggs F. Riley, M. E.; MacCallum: *Theoretical electron-atom elastic scattering cross sections: Selected elements, 1 keV to 256 keV.* Atomic Data and Nuclear Data Tables **15**, 443-476 (1975).

[95] M. Sarikaya, M. Qian and E.A. Stern: *EXELFS revisited.* Micron **27**, 449-466 (1996).

[96] M. Qian, M. Sarikaya and E. A. Stern: *Development of the EXELFS technique for high accuracy structural information.* Ultramicroscopy **59**, 137-147 (1995).

[97] Z. W. Yuan, S. Csillag, M. A. Tafreshi and C. Colliex: *High spatial resolution extended energy loss fine structure investigations of silicon dioxide compounds.* Ultramicroscopy **59**, 149-157 (1995).

[98] A. J. Bourdillon, S. M. El-mashri and A. J. Forty: *Application of TEM extended electron energy loss fine structure to the study of aluminium oxide films.* Philosophical Magazine A **49**, 341-352 (1984).

[99] G. Benner, H. Niebel and G. Pavia: *Nano beam diffraction and precession in an energy filtered C_S corrected transmission electron microscope.* Crystal Research and Technology **46**, 580-588 (2011).

[100] L. Fan, D. Paterson, I. Mcnulty, M. M. J. Treacy and J. M. Gibson: *Fluctuation X-ray microscopy: a novel approach for the structural study of disordered materials.* Journal of Microscopy **225**, 41-48 (2007).

[101] M. M. J. Treacy: *When structural noise is the signal: Speckle statistics in fluctuation electron microscopy.* Ultramicroscopy **107**, 166-171 (2007).

[102] M. M. J. Treacy and J. M. Gibson: *Variable coherence microscopy: A rich source of structural information from disordered materials.* Acta Crystallographica Section A **52**, 212-220 (1996).

[103] M. M. J. Treacy, J. M. Gibson, L. Fan, D. J. Paterson and I. McNulty: *Fluctuation microscopy: a probe of medium range order.* Reports on Progress in Physics **68**, 2899-2944 (2005).

[104] M M J Treacy, D Kumar, A Rougée, G Zhao, P R Buseck, I McNulty, L Fan, C Rau and J M Gibson: *Probing medium-range structural correlations by fluctuation microscopy.* Journal of Physics: Condensed Matter **19**, 455201 (2007).

[105] P. Wochner, C. Gutt, T. Autenrieth, T. Demmer, V. Bugaev, A. D. Ortiz, A. Duri, F. Zontone, G. Grubel and H. Dosch: *X-ray cross correlation analysis uncovers hidden local symmetries in disordered matter.* Proceedings of the National Academy of Sciences of the United States of America **106**, 11511-11514 (2009).

Curriculum vitae

Personal details

Name:	XiaoKe Mu
Date of birth:	21. May 1984
Place of birth:	Shandong, China
Marital status:	Single
Nationality:	China

Educations

01/2010 – 08/2013	PhD student in Stuttgart Center for Electron Microscopy (StEM), Max Planck Institute for Intelligent Systems, Stuttgart, Germany
09/2008 – 09/2009	Msc in Nanomaterials for Nanoengineering, University of Sheffield (Merit Honours)
2007 – 2008	English language, English Language Teaching Centre, University of Sheffield
2002 – 2006	BSc Applied Physics, China University of Petroleum (First Class Honours)

Publication list

1. Xiaoke Mu, Sridhar Neelamraju, Wilfried Sigle, Christoph T. Koch, Nico Totó, J. Christian Schön, Andreas Bach, Dieter Fischer, Martin Jansen, and Peter A.

van Aken, *Evolution of order in amorphous-to-crystalline phase transformation of MgF_2*, Journal of Applied Crystallography **46** (2013), 1105–1116.

2. Xiaoke Mu, Wilfried Sigle, Andreas Bach, Dieter Fischer, Martin Jansen, and Peter A van Aken, *Influence of a second cation ($M = Ca^{2+}$, Mg^{2+}) on the phase evolution of (Ba_x, M_{1-x})F_2 starting from amorphous deposits*, submitted (2013).
3. Andreas Bach, Dieter Fischer, Xiaoke Mu, Wilfried Sigle, Peter A. van Aken, and Martin Jansen, *Structural evolution of magnesium difluoride: from an amorphous deposit to a new polymorph*, Inorganic Chemistry **50** (2011), 1563–1569.
4. Chilin Li, Xiaoke Mu, Peter A. van Aken, and Joachim Maier, *A high-capacity cathode for lithium batteries consisting of porous microspheres of highly amorphized iron fluoride densified from its open parent phase*, Advanced Energy Materials, **3** (2013), 113–119.
5. Chilin Li, Conglin Yin, Xiaoke Mu, Peter A van Aken, and Joachim Maier, *Top-down synthesis of open framework fluoride for lithium and sodium batteries*, Chemistry of Materials, **25** (2013), 962–969.
6. Chilin Li, Conglin Yin, Lin Gu, Robert E Dinnebier, Xiaoke Mu, Peter A. van Aken, and Joachim Maier, *A $FeF_3 \cdot 0.5H_2O$ polytype: microporous framework compound with intersecting tunnels for Li and Na batteries*, Journal of the American Chemical Society **135** (2013), 11425-11428.
7. Kun Tang , Xiaoke Mu, Peter A. van Aken, Yan Yu, and Joachim Maier, *"Nano-Pearl-String" $TiNb_2O_7$ as anodes for rechargeable lithium batteries, Advanced Energy Materials*, **3** (2013), 49–53.
8. Kun Tang, Yan Yu, Xiaoke Mu, Peter A. van Aken, and Joachim Maier, *Multichannel hollow TiO2 nanofibers fabricated by single-nozzle electrospinning and their application for fast lithium storage*, Electrochemistry Communications, **28** (2013), 54–57.
9. Kun Tang, Robin J. White, Xiaoke Mu, Maria-Magdalena Titirici, Peter A. van Aken, and Joachim Maier, *Hollow carbon nanospheres with a high rate capability for lithium-based batteries*, ChemSusChem, **5** (2012), 400–403.

10. Xiaoke Mu, Yong Peng, Thirunavukkarasu Gnanavel, Beverley J Inkson, Günter Möbus, *Nanoporous structures from anodisation of non-planar aluminium surfaces*, Journal of Physics: Conference Series, **241** (2010), 012089.

Conference publications

1. Xiaoke Mu, Andreas Bach, Wilfried Sigle, Dieter Fischer, Martin Jansen, and Peter A. van Aken, *A study of structural evolution of alkaline earth fluorides from amorphous to polycrystalline phase by in-situ TEM*, Microscopy Conference MC2013 in Regensburg, Germany (2013), **Oral presentation**

2. Xiaoke Mu, Sridhar Neelamraju, Wilfried Sigle, Christoph T. Koch, Nico Totó, J. Christian Schön, Andreas Bach, Dieter Fischer, Martin Jansen, and Peter A. van Aken, *TEM study of the structural evolution of ionic solids from amorphous to polycrystalline phases in the case of alkali difluoride systems*, European Microscopy Congress EMC2012 in Manchester, UK (2012), 0493. **Oral presentation**

3. Xiaoke Mu, Wilfried Sigle, Andreas Bach, Dieter Fischer, Nico Totó, Sridhar Neelamraju, J. Christian Schön, Martin Jansen, and Peter A. van Aken, *Electron diffraction analysis of the structural evolution of MgF2 from an amorphous phase to a polycrystalline modification*, Microscopy Conference MC2011 in Kiel, Germany (2011), 163. **Best poster award**

4. Xiaoke Mu, Yong Peng, Thirunavukkarasu Gnanavel, Beverley J Inkson, Günter Möbus, *Nanoporous structures from anodisation of non-planar aluminium surfaces*, Electron Microscopy and Analysis Group' s EMAG2009 in Sheffield, UK (2009), Journal of Physics: Conference Series, **241** (2010), 012089

Erklärung zur Dissertation

Hiermit versichere ich, die vorliegende Dissertation ohne Hilfe Dritter nur mit den angegebenen Quellen und Hilfsmitteln angefertigt zu haben. Alle Stellen, die aus Quellen entnommen wurden, sind als solche kenntlich gemacht. Diese Arbeit hat in gleicher oder ähnlicher Form noch keiner Prüfungsbehörde vorgelegen.

Darmstadt, im Juni 2013

(Xiaoke Mu)